**Lateral Variations in Attenuation and Anisotropy of the Upper Mantle from Seismic Waveform Tomography**

by

Yuan-Cheng Gung

B.S. (National Taiwan Normal University) 1990
M.S. (National Taiwan Chung-Cheng University) 1992

A dissertation submitted in partial satisfaction of the
requirements for the degree of
Doctor of Philosophy

in

Geophysics

in the

GRADUATE DIVISION
of the
UNIVERSITY of CALIFORNIA at BERKELEY

Committee in charge:

Professor Barbara Romanowicz, Chair
Professor Douglas Dreger
Professor Philip Stark

Fall 2003

## Abstract

Lateral Variations in Attenuation and Anisotropy of the Upper Mantle from Seismic Waveform Tomography

by

Yuan-Cheng Gung

Doctor of Philosophy in Geophysics

University of California at Berkeley

Professor Barbara Romanowicz, Chair

We present constraints on Earth's upper mantle structure from seismic tomography. Using the well established waveform inversion technique for seismic velocity, we extend this mode-perturbation-based approach to resolve anelasticity and anisotropy. We develop an inversion procedure for $Q$ tomography involving two steps: (1)3D whole-mantle velocity models are first derived using nonlinear asymptotic coupling theory, which takes into account across-branch coupling effects among Earth's normal modes; and (2)the surface waveforms thus aligned in phase are inverted to obtain a degree 8 upper mantle $Q$ model, $QRLW8$. Various stability tests are performed to assess the quality of the model, and in particular to assess possible contamination from focusing effects. We find that the 3D patterns obtained are stable, but the amplitude of the lateral variation in $Q$ is not well constrained. By comparing the $Q$ model to velocity models, we address its implications for thermal upwellings, mantle dynamics and heat flux. We also develop an inversion procedure for transverse anisotropy using three-component surface and body waveform data. The procedure combines non-linear asymptotic theory and appropriate anisotropic kernels for weak transverse anisotropy. The resulting degree 16 model ($SAW16AN$) shows that significant radial anisotropy with $V_{SH} > V_{SV}$ is present under most cratons in the depth range 250-400 km. This explains the lack of correlation among global tomographic

models derived from different groups at this depth range. It also leads us to propose a new interpretation of the thickness of seismically defined tectosphere.

Professor Barbara Romanowicz
Dissertation Committee Chair

# Contents

# List of Figures

# Acknowledgements

I wish to express my most sincere gratitude and appreciation to Barbara Romanowicz, my supervisor, for her continuous encouragement and guidance at all phases of this work. She has been enthusiastic and optimistic about this research, and always been available to answer my questions. All this and the fruitful conversations with her are essential for the final completion of this thesis.

I am grateful to Doug Dreger. Discussions with him have been instrumental and have given me valuable insight into the overall area of seismology. My thanks also extend to Phillip Stark for serving on my dissertation committee. Much of the editorial work of this thesis has benefited from his thorough reviews. I am indebted to Xiang-Dong Li who wrote the essential part of the codes used in this thesis.

I would like to thank Yann Capdeville for his excellent collaboration and French humor, and Mark Panning for his anisotropy coding and English tutoring. I am also grateful to Charley Paffenbarger, Douglas Neuhauser and Peter Lombard for developing such a wonderful computing environment and assisting me patiently with my numerous requests.

I wish to express my sincere thanks to Hrvoje Tkalčić, Wu-Cheng Chi, Junkee Rhie and Sébastien Rousset for their warm friendship and companionship. Particular thanks to Wu-Cheng Chi for helping me tremendously when I was new at Berkeley.

It's a golden opportunity to interact with the scientists and graduate students at Berkeley Seismological Lab. Thanks to Bob Uhrhammer, Charles Mégnin, Ludovic Bréger, David Dolenc, Akiko toh, Sierra Boyd, Bob Nadeau, Lind Gee, Mark Murray, Dennise Templeton, Aimin Cao. Special thanks to Bob and Sierra for helping me with the proofreading of this thesis.

I must acknowledge my debt to my friends and teachers in Taiwan: Wen-Tzong Liang, Ban-Yuan Kuo, Chau-Huei Chen, Chew-Fent Shieh, Gwo-Bin Ou and Cheng-Horng Lin. I would never have reached this stage without their support and encouragement.

Finally I want to express my greatest appreciation to my wife Wanlan for her love, constant encouragement and never-fading understanding.

# Chapter 1

# Introduction

The aim of this thesis is to constrain the lateral variations in attenuation and radial anisotropy of the Earth's upper mantle using three-component long-period seismic waveforms.

In chapter 2, we review the theoretical foundations for the waveform modeling techniques used in this thesis: the conventional 'path-average approximation' (*PAVA*) [*Woodhouse & Dziewonski*, 1984], 'non-linear asymptotic coupling theory' (*NACT*) [*Li & Romanowicz*, 1995], and an extension of *NACT* that includes out of plane focusing terms computed asymptotically [*Romanowicz*, 1987a; *Romanowicz, Gung & Capdeville*, 2003]. We first introduce the basic concept of normal mode summation, and extend it to a slightly aspherical Earth model using first order perturbation theory. Finally, the three asymptotic approaches above are compared with the reference seismograms computed by the coupled SEM/normal mode method [*Capdeville et al.*, 2003a] in 3-D Earth models.

To zeroth order in $1/l$ ($l$ is the angular order of the normal mode of the Earth), the asymptotic expansion of the along-branch coupling effects results in *PAVA*, which assumes that the seismogram is sensitive only to the horizontally averaged structure

along the great-circle path from the source to the receiver. *PAVA* is a fairly accurate approximation for fundamental mode surface waves, but is inaccurate for body waves [*Li & Tanimoto*, 1993].

In addition to the along-branch coupling, *NACT* includes the effects of across-branch mode coupling, which are neglected in *PAVA*. *NACT* provides appropriate sensitivity kernels for body waves, and is therefore significantly more powerful in resolving 3-D structure in the deep mantle [*Li & Romanowicz*, 1995; *Li & Romanowicz*, 1996; *Mégnin & Romanowicz*, 1999a; *Mégnin & Romanowicz*, 1999b].

The contributions of off-great-circle structure are included in the formalism by higher order asymptotic theory [*Romanowicz*, 1987a; *Romanowicz, Gung & Capdeville*, 2003]. This technique is used in chapter 3 to evaluate the possible focusing/defocusing contamination in the resulting $Q$ model.

Next, we apply both *PAVA* and *NACT* to derive a degree 8 three-dimensional $Q$ model (*QRLW8*) of the upper mantle. Through a synthetic experiment, we demonstrate that the phase shift correction for the 3-D elastic model is a prerequisite for accurate $Q$ tomography using waveforms. Accordingly, a two step inversion procedure is set up. In the first step, 3D whole-mantle velocity models are derived separately for $V_{SH}$ (transverse component) and $V_{SV}$ (vertical and longitudinal component), using both surface and body waveforms and the *NACT* approach. In the second step, the surface waveforms, aligned in phase using the velocity models, are inverted to obtain a 3-D $Q$ model for the depth range of 80-670 km.

Various stability tests are performed and the contamination from focusing effects is examined to assess the quality of *QRLW8*. We conclude that the 3D patterns obtained are stable, but the amplitude of the lateral variations in $Q$ is not well constrained.

The model agrees with previous results in that there is a strong correlation of $Q$ with tectonics in the top 250 km of the upper mantle. In the depth range of the upper mantle transition zone, the $Q$ distribution is generally dominated by two strong

minima, one under the southern Pacific and one under Africa. This results in a strong degree-2 pattern, coherent with the elastic velocity distribution near the core-mantle boundary.

We introduce the technical components of *QRLW8* in chapter 3. This chapter has been submitted to *Geophysical Journal International* under the reference [*Gung & Romanowicz*, 2003].

Because $Q$ is considerably more sensitive to temperature variations than elastic velocities [*Jackson et al.*, 1992], $Q$ tomography should be able to provide us important information on the thermal structure in the mantle and therefore its dynamics, complementing that provided by elastic tomography. In chapter 4, through comparisons of *QRLW8* and the whole mantle velocity models, we discuss the implications of *QRLW8* in relation to mantle dynamics. This chapter was published in *Science* under the reference [*Romanowicz & Gung*, 2002].

In the development of *QRLW8*, a degree 16 $SV$ model *SAW16BV* is derived to correct the phase shift of Rayleigh waves better. The inferred anisotropy from the comparison of *SAW16BV* and the Berkeley $V_{SH}$ model, *SAW24B16* [*Mégnin & Romanowicz*, 1999b], inspired us to investigate further the upper mantle anisotropy with an improved method.

In chapter 5 we develop an inversion procedure for transverse isotropy using three-component surface and body waveform data. The procedure used appropriate kernels for weak transverse anisotropy. The resulting degree 16 anisotropic model, *SAW16AN*, has transverse isotropy with $V_{SH} > V_{SV}$ under the central Pacific and Indian oceans in the depth range 100-200km. At greater depth (250-400km), the $V_{SH} > V_{SV}$ signal is more pronounced under most continental cratons. Two main issues are discussed based on the results: (1) The thickness of the seismically defined tectosphere. (2) The nature of Lehmann and Gutenberg discontinuities. This chapter was published in *Nature* under the reference *Gung et al.* [2003].

Finally, we briefly summarize the key features and implications of *QRLW8* and *SAW16AN* in Chapter 6.

# Chapter 2

# Theoretical background

Normal mode asymptotic coupling theory is used to model waveforms in this study. The fundamental formalisms of the theory are introduced in this chapter. We will start from the normal mode summation in a spherically symmetric Earth model (Section 2.1), then advance to 3-D models using first-order perturbation theory (Section 2.2). In Section 2.3, we discuss two analytical approximations, the classical 'path-average approximation' [*Woodhouse & Dziewonski*, 1984] and 'non-linear asymptotic coupling theory' [*Li & Romanowicz*, 1995]. Both are derived using zeroth-order asymptotic approximation. In Section 2.4, with higher order asymptotic theory we extend the formalism to include out-of-plane focusing effects [*Romanowicz*, 1987a; *Romanowicz, Gung & Capdeville*, 2003]. Finally, we apply the coupled method of spectral elements and modal solution [*Chaljub et al.*, 2003; *Capdeville et al.*, 2003a] to benchmark the analytical approximations in 3-D models, and in particular, to test the validity of the new code, which includes the off-plane focusing terms.

## 2.1 Normal Mode Summation in an SNREI Earth

The response of a finite body, such as the Earth, to a mechanical disturbance can be expressed as a superposition of the body's normal modes. For internal sources these normal modes are called free oscillations. Here we develop the formalism of synthesizing seismograms with normal mode summation for an SNREI (spherical non-rotating elastic and isotropic) Earth model excited by a point source.

To derive the basic formalism of excitation of free oscillations, following the classical paper by *Gilbert* [1971], we start by considering a particle system. Consider a conservative system of $N$ particles in a small oscillation about a state of stable equilibrium. The change in internal forces between particles is assumed to be a linear function of displacement, so the equation for the conservation of linear momentum can be expressed as

$$m_\alpha \frac{d^2\mathbf{u}_\alpha(\mathbf{t})}{dt^2} + \sum_{\beta=0}^{N} \mathbf{V}_{\alpha\beta} \cdot \mathbf{u}_\beta = \mathbf{f}_\alpha, \tag{2.1}$$

where $\mathbf{u}_\alpha$ is the displacement of the $\alpha$th particle, $\alpha = 1, ..., N$, $m_\alpha$ is its mass, $\mathbf{f}_\alpha$ is the force applied to it, and $\mathbf{V}_{\alpha\beta}$ is the symmetric, positive definite potential energy matrix. The initial conditions are

$$\mathbf{u}_\alpha(0) = \frac{d}{dt}\mathbf{u}_\alpha(0) = \mathbf{0}. \tag{2.2}$$

There are $3N$ eigenfrequencies $\omega_j; j = 1, ..., 3N$, and $3N$ eigenvectors, or normal modes, ${}_j\mathbf{u}_\alpha \exp(i\omega_j t)$ for the system. The normal modes are ortho-normal

$$\sum_\alpha m_\alpha ({}_j\mathbf{u}_\alpha^*) \cdot \ ({}_k\mathbf{u}_\alpha) = \delta_{jk}, \tag{2.3}$$

where the asterisk indicates complex conjugation.

To find the solution of (2.1) as a superposition of normal modes, we need to find the coefficients $\{a_j\}$ in the expansion

$$\mathbf{u}_\alpha(t) = \sum_j a_j({}_j\mathbf{u}_\alpha)\exp(-i\omega_j t). \tag{2.4}$$

Substituting (2.4) into (2.1) and applying the Laplace transformation allows the coefficients $\{a_j\}$ to be calculated easily. Assuming that the excitation is a step-function in time times a point force in space, the displacement of $\alpha$th particle can be expressed as

$$\mathbf{u}_\alpha(t) = \sum_j \left( \sum_\beta {}_j\mathbf{u}^*_\beta \ \cdot \mathbf{F}_\beta \right) {}_j\mathbf{u}_\alpha \frac{1-\cos\omega_j t}{\omega_j^2}. \tag{2.5}$$

(2.5) indicates that a new reference level has been initiated at $t = 0$, and the motion in each mode can be thought of as an oscillation about this new reference level.

After finding the solution of normal mode excitation within a dynamic particle system, we now apply it to the excitation of the Earth by an earthquake that is approximated as a step-function in time, times a point force in space, with a prescribed moment tensor.

For the Earth, we may replace the particle sum over $\beta$ by a volume integral taken over the whole Earth. (2.5) becomes

$$\mathbf{u}(\mathbf{x},t) = \ \sum_j \left( \int_V \mathbf{u}^*_j(\xi)\cdot\mathbf{f}(\xi)\,dv \right) \mathbf{u}_j(\mathbf{x}) \frac{1-\cos\omega_j t}{\omega_j^2}, \tag{2.6}$$

where $j$ denotes the $j$th normal mode of the whole Earth, and $\mathbf{f}$ is the body force per unit volume. Though the sum in (2.6) is now an infinite sum, it converges as $\omega_j^{-2}$

[*Rayleigh*, 1945]. The normalization of the normal modes in (2.3) is modified as

$$\int_V \rho(\xi)\mathbf{u}_j^*(\xi)\cdot\mathbf{u}_k(\xi)\ dv = \delta_{jk}, \tag{2.7}$$

where $\rho$ is the density.

In an SNREI Earth, the eigenvectors for displacement can be expressed in the general form

$$\mathbf{u}_i(\mathbf{x}) = {}_nU_l(r)Y_l^m(\theta,\phi)\hat{r} + {}_nV_l(r)\nabla_1 Y_l^m(\theta,\phi) + {}_nW_l(r)\hat{r}\times\nabla_1 Y_l^m(\theta,\phi), \tag{2.8}$$

where $(n,l,m)$ are the radial, angular and azimuthal orders of the singlet with index $j$, $(r,\theta,\phi)$ are spherical coordinates of $\mathbf{x}$, $Y_l^m$ are fully normalized spherical harmonics [*Edmonds*, 1960], ${}_nU_l$, ${}_nV_l$ and ${}_nW_l$ are the radial eigenfunctions for the Earth, and $\nabla_1$ is the surface gradient operator:

$$\nabla_1 Y_l^m = \frac{\partial Y_l^m}{\partial\theta}\hat{\theta} + \frac{1}{\sin(\theta)}\frac{\partial Y_l^m}{\partial\phi}\hat{\phi}. \tag{2.9}$$

There are two types of oscillations: Spheroidal motion, for which the vertical component of $\nabla_1\times\mathbf{u}$ is zero; and toroidal motion, for which both $\mathbf{u_r}=0$ and $\nabla_1\cdot\mathbf{u_r}=0$. In an SNREI Earth, Spheroidal motion is a function of ${}_nU_l$ and ${}_nV_l$, and toroidal motion is a function of ${}_nW_l$.

To apply (2.6) to seismology, we consider the free oscillations to be excited by earthquakes. An equivalent body force approximation of the source can be expressed using moment tensors (e.g., *Aki & Richards* [2002])

$$f_p(\xi,t) = -\mathbf{M}_{pq}(t)\frac{\partial}{\partial\xi_q}\delta(\xi-\mathbf{x}_s). \tag{2.10}$$

If $\mathbf{M}$ acts as a step function in time at $\mathbf{x_s}$ (the location of the source), the $j$th excitation coefficient in (2.6) becomes

$$\begin{aligned}\int_V \mathbf{u}_j^*(\xi)\cdot\mathbf{f}(\xi)\,dv &= -\mathbf{M}_{pq}\int_V (\mathbf{u}_j)_p^*(\xi)\frac{\partial}{\partial\xi_q}\,\delta(\xi-\mathbf{x}_s)\,dv(\xi)\\ &= (e_j)_{pq}^*(\mathbf{x}_s)\mathbf{M}_{pq},\end{aligned} \tag{2.11}$$

where $(e_j)_{pq}$ is the $(pq)$ strain component of the $j$th normal mode, $e_{pq}=\frac{1}{2}(\partial u_p/\partial\xi_q+\partial u_q/\partial\xi_p)$. Substituting (2.11) into (2.6), and differentiating twice to convert displacement to acceleration, we obtain

$$\frac{\partial^2\mathbf{u}}{\partial t}(\mathbf{x},t)=\Re e\,\sum_j\left(-\mathbf{M}:\epsilon^*\right)(\mathbf{x}_s)\;\mathbf{u}_j(\mathbf{x})\exp(i\omega_j t), \tag{2.12}$$

where $\mathbf{u}_j$ and $\omega_j$ are, respectively, the spatial eigenvector and eigenfrequency of the $j$th mode, and $\mathbf{M}:\epsilon^*$ is tensor notation for $\sum_{pq}\mathbf{M}_{pq}(e_j)_{pq}^*$. The sum extends over all modes. To further simplify (2.12), we introduce the receiver vector, $R_K^m$, and the source vector, $S_K^m$:

$$R_K^m \equiv \mathbf{v}\cdot\mathbf{u}_K(\mathbf{x}), \tag{2.13}$$

$$S_K^m \equiv -(\mathbf{M}:\epsilon)(\mathbf{x}_s), \tag{2.14}$$

where $K$ is the multiplet index, which incorporates overtone number $n$, angular order $l$, and mode type (toroidal/spheroidal mode); and $\mathbf{v}$ is the unit vector in the direction of seismic observation. With these definitions, (2.12) becomes the well-known expression for the normal mode summation in an SNREI model

$$u_0(\mathbf{x},t)=\Re e\,\sum_K\exp(i\omega_K t)\sum_{m=-l}^{l}R_K^m S_K^m, \tag{2.15}$$

where $u_0$ ($= \mathbf{v} \cdot \frac{\partial^2 \mathbf{u}}{\partial t}$) is the $\mathbf{v}$ component of acceleration in a spherical symmetric Earth model. As indicated in (2.15), multiplets are degenerate in the SNREI model: the eigenfrequency does not depend on the azimuthal order $m$. Each multiplet consists of $2l + 1$ singlets sharing the same eigenfrequency.

## 2.2 First-order perturbation in an aspherical elastic Earth

A general formalism for calculating long-period seismograms in a slightly aspherical Earth model by summing normal modes has been developed by *Woodhouse* [1983] and *Tanimoto* [1984] using first-order perturbation theory.

The equation governing the displacement field $\mathbf{u}(\mathbf{x}, t)$ due to an earthquake may be written

$$(\mathcal{H} + \rho\partial_t^2)\mathbf{u} = \mathbf{f}, \tag{2.16}$$

where $\mathcal{H}$ is an integro-differential tensor operator representing the effects of the elastic restoring force and the gravitational force. The same approximations of earthquake sources used in section 2.1 are used for $\mathbf{f}$, the equivalent body force distribution of the source. Note the similarities between (2.16) and (2.1), except now the matrix form is used for $\mathcal{H}$ and $\mathbf{f}$.

(2.16) can be solved in the same manner as (2.1), by expanding $\mathbf{u}$ in terms of the normal modes of a spherical symmetric reference Earth model

$$\mathbf{u} = \sum_j a_j(t)|j), \tag{2.17}$$

where $\{|j)\}_{j=0}^{\infty}$ represents the complete set of eigenfunctions. We may rewrite the orthonormality condition (2.7)

$$(j|\rho^{(0)}|k) \equiv \int_V |j)^* \cdot \rho^{(0)}|k)\, dv \; = \delta_{jk}, \tag{2.18}$$

where $\rho^{(0)}$ is the density distribution of the reference model. *Woodhouse* [1983] shows that the solution to (2.16) for an initially quiescent Earth model ($\mathbf{a}(0) = \partial_t \mathbf{a}(0) = 0$, where $\mathbf{a} = \{a_j\}_{j=0}^{\infty}$) is given through the coefficients $\{a_j\}$

$$\mathbf{a}(t) \; = \; \Re e \left( \int_0^t \mathbf{X}^{-2} \; (\mathbf{I} \; - \exp\left[i(t-\tau)\,\mathbf{X}\right]) \; \mathbf{P}^{-1}\, \partial_t\, \mathbf{s}(\tau)\, d\tau \right), \tag{2.19}$$

where $\mathbf{X}$ is defined through $\mathbf{X}^2 \equiv \mathbf{P}^{-1}\mathbf{H}$, $\mathbf{I}$ is the identity matrix, and the elements of $\mathbf{P}$, $\mathbf{H}$ and $\mathbf{s}$ are given by

$$H_{jk} \equiv (j|\mathcal{H}|k), \tag{2.20}$$

$$P_{jk} \equiv (j|\rho|k), \tag{2.21}$$

$$s_j \equiv (j|I|\mathbf{f}), \tag{2.22}$$

where $I$ is identity operator.

For a step-function source, $\partial_t s_j(t) \; = \; \delta(t)\, S_j$ ($S_j$ is the source vector defined in (2.14)), a particular component of acceleration, $u(t) = \mathbf{v} \cdot \partial_t^2 \mathbf{u}(\mathbf{x}_r, t)$, can be expressed as

$$u(t) = \Re e\{\mathbf{R}\, \exp[i\,\mathbf{X}\,t]\mathbf{P^{-1}}\,\mathbf{S}\}, \tag{2.23}$$

where $R$ is the receiver vector defined in (2.14). As noted by *Woodhouse* [1983], although the formal expression (2.23) is an exact solution to (2.16), it is not practical for computation. In the following, we apply perturbation theory to derive an approximate expression.

A slightly aspherical Earth can be thought of as a small perturbation of the spherical symmetric reference Earth model, e.g., $\rho = \rho^{(0)} + \rho^{(1)}$. The superscript (0) refers to the reference model and superscript (1) to the small perturbation. In the same way, we may approximate the operator $\mathbf{\Theta}$, by decomposing it into the sum of a reference term (evaluated for the reference model) and a small perturbation term: $\mathbf{\Theta} = \mathbf{\Theta^{(0)}} + \mathbf{\Theta^{(1)}}$, $\mathbf{\Theta} \in \{\mathbf{P}, \mathbf{H}, \mathbf{X}\}$. Then to first-order in the perturbation (i.e. second-order quantities are neglected), we have [*Woodhouse*, 1983]:

$$P_{jk}^{-1} = \left(P_{jk}^{(0)} + P_{jk}^{(1)}\right)^{-1} \approx I_{jk} - P_{jk}^{(1)}, \tag{2.24}$$

$$X_{jk} = X_{jk}^{(0)} + X_{jk}^{(1)} \approx \omega_j I_{jk} + \frac{Z_{jk}}{\omega_j + \omega_k}, \tag{2.25}$$

where $Z_{jk} \equiv H_{jk}^{(1)} - \omega_k^2 P_{jk}^{(1)}$. Thus, (2.23) becomes

$$u(t) = \Re e \sum_{jk} R_j \left[\exp(iX_{jk}t) - \exp(i\omega_j t) P_{jk}^{(1)}\right] S_k. \tag{2.26}$$

(2.26) indicates that the aspherical structure introduces perturbations to the normal modes of the reference model. The phases and amplitudes are perturbed. The effect of the complex phase perturbation in the first term ($X_{jk}$) on the shape of waveforms increases with time, and eventually dominates that of the amplitude perturbation, which results from density perturbations ($P_{jk}^{(1)}$). Therefore, it is common to neglect the effect of amplitude perturbation [*Woodhouse*, 1980; *Romanowicz*, 1987a; *Li & Tanimoto*, 1993], which leaves:

$$u(t) = \Re e \sum_{jk} R_j \exp\left[it\left(\omega_j I_{jk} + \frac{Z_{jk}}{\omega_j + \omega_k}\right)\right] S_k. \tag{2.27}$$

As shown by *Tanimoto* [1984], (2.27) represents the first-order 'Born' solution to the displacement in a slightly heterogeneous Earth. The omitted amplitude perturbations are different from the amplitude anomalies due to focusing/defocusing of propagating waves [*Woodhouse & Wong*, 1986; *Romanowicz*, 1987a]. The focusing/defocusing effects are still present in (2.27).

## 2.3 Nonlinear asymptotic coupling theory

Because computing (2.27) becomes very expensive as the angular degree $l$ of modes becomes large, further approximations are required to apply it to seismic tomography.

To zeroth-order in $1/l$, when only coupling along the same dispersion branch is considered, the approximated coupling effect is equivalent to path-average approximation (*PAVA*) [*Woodhouse & Dziewonski*, 1984], which assumes that seismograms are sensitive only to the horizontally averaged structure along the great circle between the source and receiver [*Romanowicz*, 1987a; *Park*, 1987]. The accuracy of *PAVA* has been investigated by *Li & Tanimoto* [1993], who found that it predicts the perturbation of the seismogram fairly well for the fundamental mode surface waves, but is inaccurate for body waves, because it fails to describe the concentration of sensitivities to structure in the vicinity of the ray path.

To account for perturbation effects on body waves, it is necessary to include the across-branch coupling effects among modes. Under the assumption that heterogeneity is laterally smooth, using a short-time approximation, *Li & Tanimoto* [1993] linearized the exponential term in (2.27), and developed a formulation for calculating body

wave seismograms. This is further improved by non-linear asymptotic coupling theory (*NACT*) [*Li & Romanowicz*, 1995], in which only across-branch coupling effects are linearized. Here we briefly review the derivation of this technique. Please refer to [*Li & Tanimoto*, 1993; *Li & Romanowicz*, 1995; *Mégnin*, 1999] for details.

Let us introduce apparent frequency shifts $\delta\omega_j$ which are the same for all the singlets belonging to the same multiplet and, generally speaking, are functionals of the locations of the source and receiver and of the given 3-D Earth model. We may then modify the phase terms in (2.27)

$$\omega_j I_{jk} + \frac{Z_{jk}}{\omega_j + \omega_j} = \widehat{\omega}_j I_{jk} + \frac{\widehat{Z}_{jk}}{\omega_j + \omega_k}, \tag{2.28}$$

where $\widehat{\omega}_j = \omega_j + \delta\omega_j$ and $\widehat{Z}_{jk} = Z_{jk} - 2\omega_j\omega_k\delta_{jk}$. The modified exponential term can be linearized as [*Li & Romanowicz*, 1995; *Mégnin*, 1999]:

$$\begin{aligned} \exp\left[it\left(\widehat{\omega}_j I_{jk} + \frac{\widehat{Z}_{jk}}{\omega_j + \omega_k}\right)\right] &\approx \exp(i\widehat{\omega}_j t) I_{jk} - it\delta\omega_j \exp(i\widehat{\omega}_j t) \\ &+ Z_{jk}\frac{\exp(i\widehat{\omega}_j t) - \exp(i\widehat{\omega}_k t)}{(\omega_j + \omega_k)(\widehat{\omega}_j - \widehat{\omega}_k)}. \end{aligned} \tag{2.29}$$

In *NACT*, the contribution of along-branch and across-branch coupling effects are considered separately. We first derive the expression for *PAVA* seismogram. Using multiplet index $K$ and azimuthal order index $m$, following *Woodhouse* [1983], we define the apparent frequency shifts by

$$\delta\omega_K = \frac{\sum\limits_{mm'} R_K^m Z_{KK}^{mm'} S_K^{m'}}{2\omega_K \sum\limits_m R_K^m S_K^m}, \tag{2.30}$$

and evaluate the apparent frequency shifts $\delta\omega_K$ using the path average approximation:

$$\delta\omega_K \equiv \frac{1}{\widehat{SR}} \int_S^R \delta\omega_{local}^K d\phi, \tag{2.31}$$

where $\delta\omega_{local}^K$ is the local frequency introduced by *Jordan* [1978] (please see (2.40) for definition), the integral is taken along the great circle from the source S to the receiver R, and $d\phi$ denotes the differential angular distance element. The *PAVA* seismogram is then expressed by

$$u_{pava}(t) = \Re e \sum_K A_K \exp(i\widehat{\omega}_K t), \tag{2.32}$$

where

$$A_K = \sum_m R_K^m S_K^m, \tag{2.33}$$

$$\widehat{\omega}_K = \omega_K + \delta\omega_K. \tag{2.34}$$

Using (2.32) and the modified phase terms in (2.29), we may rewrite (2.27)

$$\begin{aligned} u(t) &= \Re e \left[ \sum_K A_K \exp(i\widehat{\omega}_K t) \right. \\ &\quad \left. - \sum_K it\, \delta\omega_K\, A_K \exp(i\widehat{\omega}_K t) + \sum_{KK'} A_{KK'} D_{KK'}(t) \right] \\ &= u_{pava}(t) + \delta u_{nact}(t), \end{aligned} \tag{2.35}$$

where

$$A_{KK'} \equiv \sum_m R_K^m Z_{KK'}^{mm'} S_{K'}^{m'}, \tag{2.36}$$

$$D_{KK'}(t) \equiv \frac{\exp(i\widehat{\omega}_K t) - \exp(i\widehat{\omega}_{K'} t)}{(\omega_K + \omega_{K'})(\widehat{\omega}_K - \widehat{\omega}_{K'})}. \tag{2.37}$$

We have separated the seismogram into two parts in (2.35): (1) $u_{pava}$, is the *PAVA* seismogram, which includes the contribution from along-branch coupling (see Appendix A.2), and is calculated in the same way as in a spherically symmetric model using a 1-D theory, with the eigenfrequencies $\widehat{\omega}_K$ evaluated for a model obtained by horizontally averaging structure along the great circle connecting the source and receiver; and (2) $\delta u_{nact}$, represents any further correction from across-branch couplings, for which we consider a linear approximation. This results in a better approximation than the complete linearization of total coupling effects.

The evaluation of $A_{KK'}$ for $K \neq K'$ becomes rapidly impractical with increasing $l$. Following *Li & Tanimoto* [1993], we derive an asymptotic approximation for $A_{KK'}$.

Because across-coupling effects are small unless $\omega_{K'}$ and $\omega_K$ are very close, we may write the frequency in $Z^{mm'}_{KK'}$, $\omega_{K'} \approx \frac{\omega_K + \omega_{K'}}{2} \approx \omega_{KK'}$, so that

$$Z^{mm'}_{KK'} \;=\; H^{(1)\,mm'}_{KK'} \;-\; \omega^2_{K'}\, P^{(1)\,mm'}_{KK'} \;\approx\; H^{(1)\,mm'}_{KK'} \;-\; \omega^2_{KK'}\, P^{(1)\,mm'}_{KK'}. \tag{2.38}$$

If lateral heterogeneities vary smoothly relative to the horizontal wavelength of modes, we can generalize the expansion for self coupling ($Z^{mm'}_{KK}$) introduced by *Woodhouse & Girnius* [1982], and approximate $Z^{mm'}_{KK'}$ as [*Romanowicz*, 1987a]

$$Z^{mm'}_{KK'} \;=\; 2\,\omega_{KK'} \int_\Omega \delta\omega_{KK'}(\theta,\phi)\, Y^{m\,*}_l(\theta,\phi)\, Y^{m'}_{l'}(\theta,\phi)\, d\Omega, \tag{2.39}$$

where $\Omega$ is the unit sphere, and the local frequency $\delta\omega_{KK'}$ is

$$\delta\omega_{KK'} \;=\; \frac{1}{2\,\omega_{KK'}} \left[ \int_0^a \delta\mathbf{m} \cdot \mathbf{M}_{KK'}(r) r^2\, dr \;-\; \sum_d r_d^2\, h_d\, H^d_{KK'} \right], \tag{2.40}$$

where $a$ is the radius of the Earth, $\delta\mathbf{m}$ represents the heterogeneous perturbations to Earth structure, and $h_d$ is the perturbation to the radius $r_d$ of the $d^{th}$ discontinuity.

The kernels $\mathbf{M}_{KK'}(r)$ and $H^d_{KK'}$ are given by *Woodhouse* [1980]. Note that the local frequency $\delta\omega^K_{local}$ in (2.31) is also calculated through (2.40) with $K = K'$.

For the earthquake source considered, the source and receiver vectors may be expressed as [*Woodhouse & Girnius*, 1982]

$$R^m_K(\theta_r, \phi_r) = \sum_{N=-1}^{1} R^N_K \, Y_l^{Nm}(\theta_r, \phi_r), \tag{2.41}$$

$$S^m_K(\theta_s, \phi_s) = \sum_{M=-2}^{2} S^M_K \, Y_l^{Mm^*}(\theta_s, \phi_s), \tag{2.42}$$

where the $Y_l^{Nm}$ are generalized spherical harmonics defined in [*Phinney & Burridge*, 1973] and the $R^N_K$ and $S^M_K$ are given in Appendix (B.4). The addition theorem for generalized spherical harmonics [*Edmonds*, 1960] states that

$$\sum_m Y_l^{Nm}(\theta_1, \phi_1) Y_l^{Mm^*}(\theta_2, \phi_2) = Y_l^{NM}(\theta_{12}, \phi_{12}) \exp[iN(\pi - \phi_{21})], \tag{2.43}$$

where $\theta_{12}$ denotes the angular distance between the point $(\theta_1, \phi_1)$ and point $(\theta_2, \phi_2)$, and $\phi_{12}$ represents the azimuth of $(\theta_1, \phi_1)$ from $(\theta_2, \phi_2)$ measured anticlockwise from south.

With (2.39), (2.42) and (2.43), we may rewrite (2.37) as

$$\begin{aligned} A_{KK'} = \; & \gamma_l \gamma_{l'} \sum_{NM} R^N_K S^M_{K'} \times \int_\Omega \delta\omega^2_{KK'} \, P_l^N(\cos\,\theta_{pr}) P_{l'}^M(\cos\,\theta_{ps}) \times \\ & \exp\left[i\left(M\phi_{ps} - N\phi_{pr}\right)\right] d\Omega_p, \end{aligned} \tag{2.44}$$

with

$$\gamma_l = \sqrt{\frac{2l+1}{4\pi}}. \tag{2.45}$$

The integral in (2.44) is taken over the unit sphere, $\delta\omega^2_{KK'} = 2\omega_{KK'}\delta\omega_{KK'}$, $P_l^N$ are associated Legendre functions, $\theta_{pr}$ is the angular distance between scatterer and receiver, $\phi_{pr}$ is the azimuth of the scatterer from the receiver measured anti-clockwise from south, $\theta_{ps}$ is the angular distance between source and scatterer, and $\phi_{ps}$ is the azimuth of the scatterer from the source. These variables are illustrated in Figure 2.1.

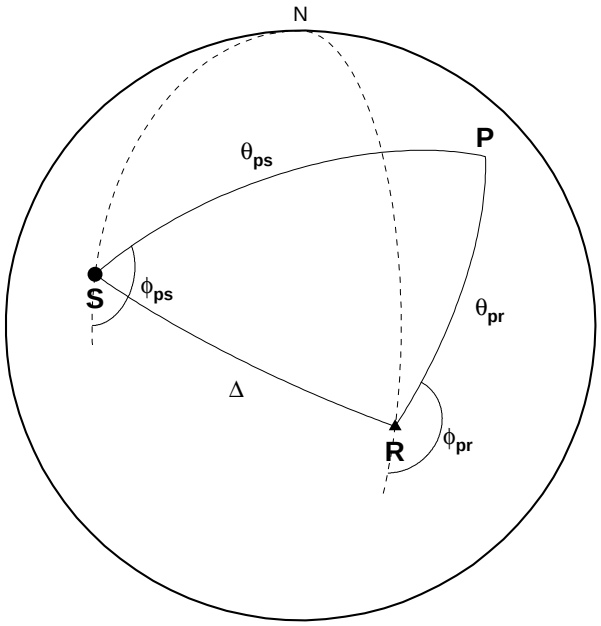


Figure 2.1: The geometrical relationship of the moving integration point (P) with the source (S) and receiver (R).

Under the assumption of short wavelength, i.e. $l \gg 1$, the associated Legendre functions may be expressed asymptotically [*Robin*, 1958; *Romanowicz & Roult*, 1986], to zeroth-order in $1/l$, by

$$\gamma_l P_l^N(\cos\theta) \approx \frac{1}{\pi\sqrt{\sin\theta}} \cos\left(\kappa\theta - \frac{\pi}{4} + \frac{N}{2}\pi\right), \tag{2.46}$$

with

$$\kappa = l + \frac{1}{2}. \tag{2.47}$$

Approximation (2.46) breaks down near $\theta = 0$ and $\theta = \pi$, which correspond to caustics for traveling waves. Replacing the associated Legendre functions in (2.44) with the asymptotic form given above, we obtain

$$A_{KK'} = \frac{1}{2\pi^2} \sum_{NM} R_K^N S_{K'}^M \int_0^{2\pi} \left[ I_1(\phi_p) + I_2(\phi_p) \right] d\phi_p, \tag{2.48}$$

where

$$\begin{aligned} I_1(\phi_p) = \quad & \int_0^{\pi} \frac{\delta\omega_{KK'}^2}{\sqrt{\sin\theta_{pr} \sin\theta_{ps}}} \\ & \times \cos\left[ \kappa(\theta_{pr} + \theta_{ps}) + j\theta_{ps} + \frac{M+N-1}{2}\pi \right] \\ & \times \exp\left[ i(M\phi_{ps} - N\phi_{pr}) \right] \sin\theta_p d\theta_p, \end{aligned} \tag{2.49}$$

$$\begin{aligned} I_2(\phi_p) = \quad & \int_0^{\pi} \frac{\delta\omega_{KK'}^2}{\sqrt{\sin\theta_{pr} \sin\theta_{ps}}} \\ & \times \cos\left[ \kappa(\theta_{pr} - \theta_{ps}) - j\theta_{ps} + \frac{N-M}{2}\pi \right] \\ & \times \exp\left[ i(M\phi_{ps} - N\phi_{pr}) \right] \sin\theta_p d\theta_p, \end{aligned} \tag{2.50}$$

where $j = l' - l$. Without loss of generality, we may choose the coordinate system in such a way that the source $(\theta_s, \phi_s)$ is located at $(\pi/2, 0)$ and the receiver $(\theta_r, \phi_r)$ is located at $(\pi/2, \Delta)$ with $0 \ll \Delta \ll \pi$. For $l \gg 1$, the integrand in (2.50) oscillates very rapidly with $\theta_p$ except in the neighborhood of the equator, where $d(\theta_{pr} + \theta_{ps})/d\theta_p$ vanishes. Following *Romanowicz & Roult* [1986], we apply the stationary phase method to perform the integration. After some algebra, the $NACT$ seismogram can be expressed as

$$u(t) \;=\; u_{pava}(t) \;+\; u_1(t) \;+\; \sum_K \sum_{K' \in \Gamma_K} D_{KK'}(t) E_{KK'}, \tag{2.51}$$

where $u_1 = -\sum_K i\, t\, \delta\omega_K\, A_K\, \exp(i\widehat{\omega}_K t)$, $\Gamma_K$ is the set of multiplets with eigenfrequencies $\omega_{K'} \geq \omega_K$, and the asymptotic scattering term $E_{KK'}$ is given by retaining only $\phi$ dependent terms in the integral:

$$E_{KK'}(t) \;\equiv\; \frac{1}{2\pi}\left[ Q^{(1)}_{KK'} \int_0^{2\pi} \delta\omega^2_{KK'} \cos(j\phi) d\phi \;+\; Q^{(2)}_{KK'} \int_0^{2\pi} \delta\omega^2_{KK'} \sin(j\phi) d\phi \right], \tag{2.52}$$

where $Q^{(1)}_{KK'}$ and $Q^{(2)}_{KK'}$ are functionals of the source and receiver, and $\phi$ is the angular distance along the great circle. $Q^{(1)}_{KK'}$ and $Q^{(2)}_{KK'}$ are given by

$$Q^{(i)}_{KK'} \;\equiv\; (-1)^{i+1} \left( P^{(i)}_{KK'} + P^{(i)}_{K'K} \right), \tag{2.53}$$

$$P^{(i)}_{KK'} \;\equiv\; g^{(1)}_l(\Delta) T^{(i)}_{KK'} + (-1)^i g^{(2)}_l(\Delta) T^{(i)}_{KK'}, \tag{2.54}$$

$$g^{(1)}_l(\Delta) \;\equiv\; \sqrt{\frac{2}{\kappa\pi \sin\Delta}} \cos\left(\kappa\Delta - \frac{\pi}{4}\right), \tag{2.55}$$

$$g^{(2)}_l(\Delta) \;\equiv\; \sqrt{\frac{2}{\kappa\pi \sin\Delta}} \sin\left(\kappa\Delta - \frac{\pi}{4}\right), \tag{2.56}$$

$$T^{(1)}_{KK'} \;\equiv\; \sum_{NM} i^{N+M} R^N_K S^M_{K'} \cos\left(\frac{N+M}{2}\pi\right), \tag{2.57}$$

$$T^{(2)}_{KK'} \;\equiv\; \sum_{NM} i^{N+M} R^N_K S^M_{K'} \sin\left(\frac{N+M}{2}\pi\right). \tag{2.58}$$

We conclude this section by comparing the sensitivity kernels of *PAVA* and *NACT*. Following *Li & Tanimoto* [1993], the sensitivity kernel $\mathbf{M}$ of a seismogram is defined by

$$\Delta u(\tau) = \int_S \mathbf{M}(r, \phi; \tau) \delta \mathbf{m} \, dA, \tag{2.59}$$

where $\Delta u$ is the perturbation seismogram due to a volumetric perturbation $\delta \mathbf{m}$, which is sampled by the sensitivity kernel $\mathbf{M}$, and the integral is taken over the whole area $S$ of the great-circle section ($dA = rd\phi dr$). A sensitivity kernel shows the regions that a particular seismic phase, arriving at the receiver at time $\tau$, has sampled.

Figure 2.2 shows the sensitivity kernels predicted by *PAVA* and *NACT* for $G$ (top), $SS$ (middle) and $S_{\mathrm{dif}}$ (bottom) phases. The sensitivity kernels are calculated based on a synthetic $SH$ seismogram computed in the spherical symmetric Earth model *PREM* [*Dziewonski & Anderson*, 1981] and low-pass filtered at a cutoff frequency $1/32Hz$. The epicentral distance is 110°, and the depth of the hypothetical earthquake is 35 km. While the kernels (*PAVA* and *NACT*) are similar for the fundamental Love wave ($G$ phase), their differences in deep-sampling phases ($SS$ and $S_{\mathrm{dif}}$) are significant. First, *NACT* provides finite-width Fresnel zones associated with body-wave propagation. Secondly, the kernels from *NACT* indicate a non-uniform sensitivity distribution along the ray path. The sensitivity concentrates at the source and receiver regions and at the bouncing point for $SS$ or diffraction region for $S_{\mathrm{dif}}$. Such concentrations at the source and receiver regions are also shown in independent studies (e.g. *Stark & Nikolayev* [1993]).

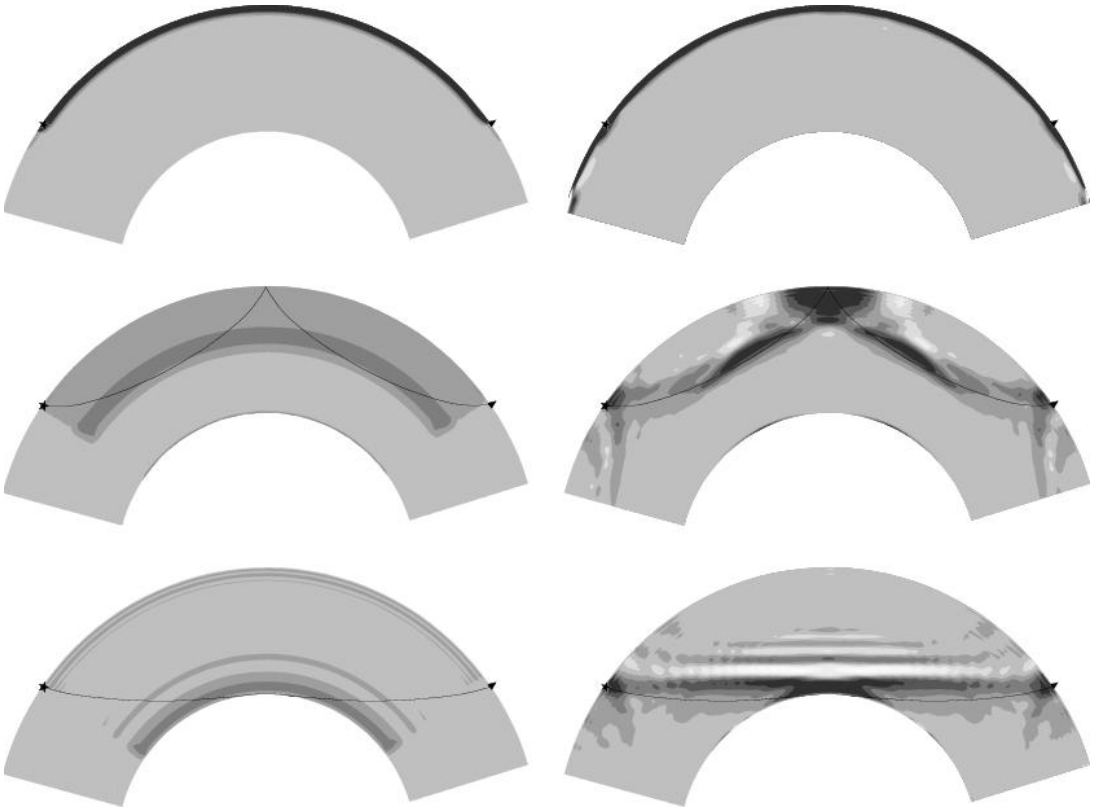

Figure 2.2: Sensitivity kernels for $G$ (top), $SS$ (middle) and $S_{\mathrm{dif}}$ (bottom) phases. The earthquake hypocenter is represented by a star and the station is represented by a triangle. The rays shown as thin curves are calculated using geometrical ray theory. The kernels shown on the left are calculated using *PAVA* and the ones shown on the right are calculated using *NACT*. (From *Li & Romanowicz* [1995].)

## 2.4 Higher order asymptotic theory

As mentioned in the end of Section 2.2, focusing/defocusing effects are present in (2.27). However, in the zeroth-order asymptotic approximation (2.46), amplitude perturbations due to the 3-D elastic structure are not included in *PAVA* or *NACT*. In both cases the perturbation seismograms are evaluated from the 2-D section beneath the great circle connecting the source and receiver. To include the focusing/defocusing effects, off-plane structure needs to be included in the formalism. Here we show that the off-plane focusing terms can be obtained by a higher order asymptotic approximation.

Following *Romanowicz* [1987a] and *Romanowicz, Gung & Capdeville* [2003] , we derive the expression for seismogram to first-order in $1/l$.

We start from the linearized form of (2.27)

$$u(t) = u_0(t) + \delta u(t), \tag{2.60}$$

where $\delta u(t)$ is the linearized waveform perturbation due to a 3-D Earth structure:

$$\begin{aligned} \delta u(t) &= \sum_{KK'} \frac{\exp(i\omega_K t) - \exp(i\omega_{K'} t)}{\omega_K^2 - \omega_{K'}^2} A_{KK'} \\ &= \sum_K \left[ \sum_{K'=K} \frac{it}{2\omega_K} A_{KK} + \sum_{K' \neq K} \frac{\exp(i\omega_K t)}{\omega_K^2 - \omega_{K'}^2} (A_{KK'} + A_{K'K}) \right]. \end{aligned} \tag{2.61}$$

$A_{KK'}$ is defined in (2.44). The asymptotic expression for associated Legendre functions, expanded to order $1/l$ [*Robin*, 1958; *Romanowicz & Roult*, 1986], is

$$\gamma_l P_l^N(\cos\theta) \approx \frac{1}{\pi\sqrt{\sin\theta}} \cos\left[\kappa\theta - \frac{\pi}{4} + \frac{N}{2}\pi + \left(\frac{N^2}{2\kappa} - \frac{1}{8\kappa}\right)\cot\theta\right]. \tag{2.62}$$

Substituting (2.62) into (2.44), we obtain

$$\begin{aligned} A_{KK'} &= \frac{1}{\pi^2}\sum_{NM} R_K^N S_{K'}^M \times \\ &\int_0^{\pi} \sqrt{\sin\lambda}\cos\left[\kappa' F(\kappa', M, \lambda)\right] \times \\ &\int_0^{2\pi} g(\lambda,\mu)\cos\left[\kappa F(\kappa, N, \beta)\right] d\lambda d\mu \end{aligned} \tag{2.63}$$

where

$$\kappa F(\kappa, J, x) = \kappa x - \frac{\pi}{4} + \frac{J\pi}{2} + (\frac{J^2}{2\kappa} - \frac{1}{8\kappa})\cot x \tag{2.64}$$

$$g(\lambda,\mu) = \frac{\delta\omega^2_{KK'}}{\sqrt{\sin\beta}}\exp\left[i(M\mu - N\mu')\right], \tag{2.65}$$

and $\lambda$, $\beta$ and $\mu$ are defined in the epicentral coordinate system (Figure 2.3).

By applying stationary phase approximation to order $1/l$ [*Romanowicz*, 1987a; *Romanowicz, Gung & Capdeville*, 2003], (see Appendix A.1), we obtain the following expression for $u_K(t)$, the contribution to the seismogram corresponding to the multiplet $K$:

$$\begin{aligned} u_K(t,\Delta) = \frac{1}{\pi\gamma_l\sqrt{\sin\Delta}} \quad & \Big[\cos(\kappa\Delta - \frac{\pi}{4})\,(B_0\cos\omega_K t - tB_1\sin\omega_K t) + \\ & \sin(\kappa\Delta - \frac{\pi}{4})\,(C_0\cos\omega_K t - tC_1\sin\omega_K t)\Big], \end{aligned} \tag{2.66}$$

which generalizes the expressions of *Romanowicz* [1987a] to any moment tensor source and to any observed component. In (2.66),

$$B_0 = T_0 + \frac{a\Delta}{\kappa U}(F_1 - \tilde{F}_7) - \frac{F_6}{\kappa} + \frac{a\Delta}{U}(\delta\tilde{\omega}_K - \delta\hat{\omega}_K)T_1, \tag{2.67}$$

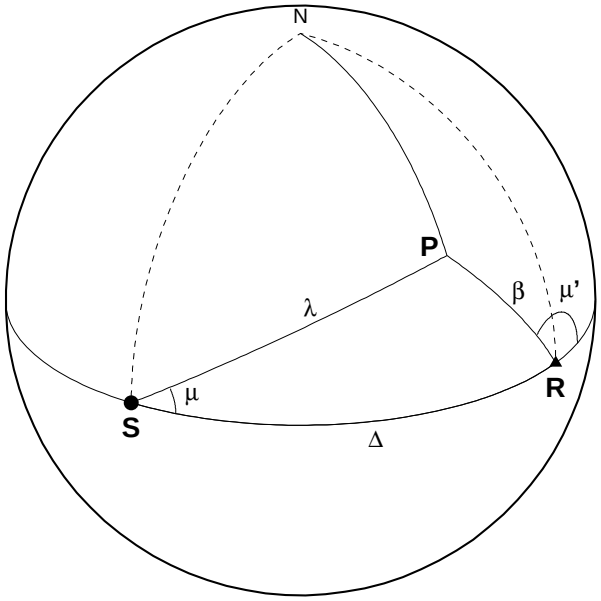


Figure 2.3: Epicentral coordinate system $(\lambda, \mu)$. S is the epicenter, R the receiver, P a point on the surface of the unit sphere, and N the pole of the source-receiver great circle.

$$B_1 = T_0 \delta\hat{\omega}_K + \frac{F_4 - \tilde{F}_{10}}{\kappa}, \tag{2.68}$$

$$C_0 = -T_1 - \frac{a\Delta}{\kappa U}(F_2 - \tilde{F}_8) - \frac{F_5}{\kappa} + \frac{a\Delta}{U}(\delta\tilde{\omega}_K - \delta\hat{\omega}_K)T_0, \tag{2.69}$$

$$C_1 = -T_1 \delta\hat{\omega}_K + \frac{F_3 - \tilde{F}_9}{\kappa}, \tag{2.70}$$

where

$$\delta\tilde{\omega}_K = \frac{1}{\Delta}\int_0^{\Delta} \delta\omega_K(s)ds, \tag{2.71}$$

$$\delta\hat{\omega}_K = \frac{1}{2\pi}\int_0^{2\pi} \delta\omega_K(s)ds. \tag{2.72}$$

Expressions for the zeroth-order terms $T_0$, $T_1$, and order $1/l$ terms $F_0 ... \tilde{F}_{10}$ are given in Appendix B. The $F$ terms contain the spatial derivatives (transverse to the great-

circle path) of the local frequency, which in turn take the off-plane structure into account, resulting in a perturbation to the amplitude. We will demonstrate focusing/defocusing effects in the next section. Note that these expressions are equivalent to those obtained by *Woodhouse & Wong* [1986] using a ray formalism.

## 2.5 Benchmarking normal mode asymptotic approximations using the coupled $SEM$/normal mode method

Before we model seismic data, we test the validity of the analytical approximations introduced in Section 2.3 and Section 2.4. For this purpose, we need a very accurate method for computing reference synthetics in a 3-D model. Here we consider the coupled $SEM$/normal mode method [*Chaljub et al.*, 2003; *Capdeville et al.*, 2003a].

The spectral element method ($SEM$) has recently been adapted successfully for global spherical Earth wave propagation applications (e.g. *Komatitsch & Vilotte* [1998]). It provides a way to compute exact seismograms in a 3-D Earth, without restrictions on the size or wavelength of lateral heterogeneity at any depth. However, it is very computationally expensive.

The coupled $SEM$/normal mode method (*CSEM*) was developed partly to address this drawback. In this method, the Earth is decomposed into two parts: a layer with 3-D lateral heterogeneities where $SEM$ computation is used, and layer(s) with spherically symmetric heterogeneities where standard normal mode computations can be applied. This hybrid method enables us to speed up the computation, while maintaining accuracy. In particular, its efficiency makes it a powerful tool to benchmark asymptotic methods.

In our 3-D synthetic test models, the Earth's mantle is the layer with lateral variations, and will be treated with $SEM$ when we apply *CSEM*. Compared to $PREM$ [*Dziewonski & Anderson*, 1981], the reference Earth model considered here is vertically smoothed near the surface. Specifically, the water layer is removed and the main discontinuities in the top 220 km are smoothed. This simplification results in considerable computational savings, because the thin layers significantly increase $SEM$ computational requirements.

Before presenting the results in 3-D models, we validate the two techniques (*CSEM* and normal mode summation) by comparing their synthetics in a spherically symmetric reference model. An isotropic source with a depth of 100 km is considered. The cut-off and corner frequencies of the filtered synthetics are 1/100 and 1/153 $Hz$ respectively. Figure 2.4 compares the vertical component of the *CSEM* and the normal mode synthetics at an epicentral distance 100°. The two methods are in excellent agreement for the reference model.

Other validations of *CSEM* have also been demonstrated in *Capdeville et al.* [2003a] and *Capdeville et al.* [2003b].

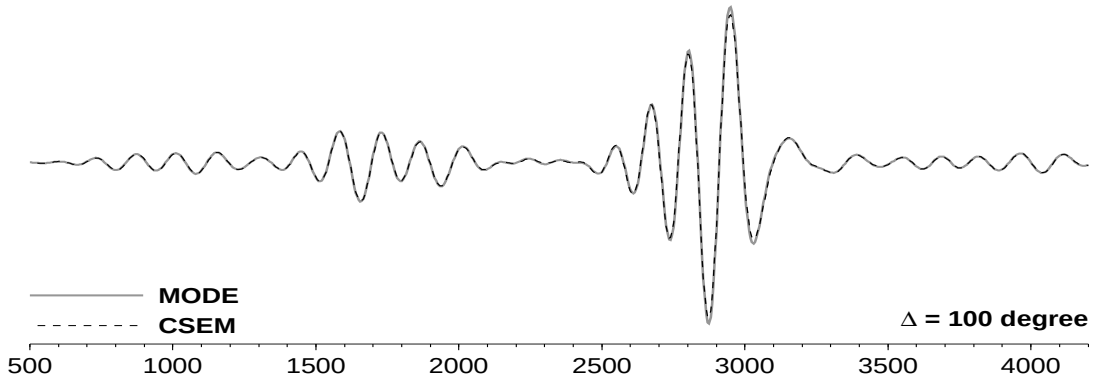


Figure 2.4: Vertical component synthetic traces of *CSEM* (dashed black line) and normal mode summation (solid gray line) for an isotropic source at an epicentral distance of 100° ($\Delta$).

In what follows, we perform computations for two 3-D synthetic models: one with single anomaly and the other with two side-by-side anomalies of opposite signs.

**3-D synthetic model: single anomaly**

The 3-D synthetic model is parameterized laterally using spherical harmonics up to degree 16, and radially using splines. It is designed to simulate a single ellipsoidal low velocity anomaly centered at 220 km depth. The maximum amplitude of the anomaly is $\sim 5$ % in $V_S$ w.r.t. the reference model. The lateral variations and cross section of this model are shown in Figure 2.5.

With the same isotropic source used to validate *CSEM*, we compute synthetics using three normal mode asymptotic approaches for this 3-D model: *PAVA*, *NACT* and *NACT+F*, an extension of *NACT* with focusing terms computed using higher order asymptotic theory. To examine more closely the small perturbation of the seismograms caused by the 3-D heterogeneities, we compare the differential waveforms (i.e. $\mathbf{u}_{\text{3D model}} - \mathbf{u}_{\text{reference model}}$) for *CSEM* and normal mode techniques. The results are shown in Figure 2.6 to Figure 2.11. These results confirm theoretical expectations.

Figure 2.6 shows the results for a receiver at an epicentral distance of 90 degrees at azimuth 180 degrees. The minor arc path connecting the source and receiver passes through the surface center of the low velocity anomaly. We note that, in the differential waveform panels, the predictions from *PAVA*, *NACT* and *NACT+F* are generally in good agreement with *CSEM* for fundamental mode wave-trains. *NACT* and *NACT+F* show a significant improvement in fit for the overtone wave-trains over *PAVA*, as expected.

Similar results are shown in Figure 2.7, where the receiver is at the same epicentral distance but at an azimuth of 170 degrees. The source-receiver great circle is now off the surface center of the low velocity anomaly, but it still passes through the anomaly, and we reach the same conclusions as before: (1) All three approximations are generally in good agreement with *CSEM* for fundamental mode wave-trains; and (2) *NACT* and *NACT+F* provide better fit for the overtone wave-trains than does PAVA.

Dramatic changes occur when source-receiver great circle just grazes the anomaly, as shown in Figure 2.8. Since both *NACT* and *PAVA* are insensitive to off-path structure, they fail to match *CSEM* synthetics, while the higher order asymptotic approximation predicts focusing effects fairly well.

We reach the same conclusions from results at a larger epicentral distance, 110 degrees, as shown in Figures 2.9 to 2.11.

In the experiment above, the amplitudes of the fundamental modes of differential waveforms are much larger than those of the overtones. This is because the sensitivities of the fundamental modes are larger at shallow depths, and phase perturbations resulting from the low velocity anomaly keep accumulating along the path.

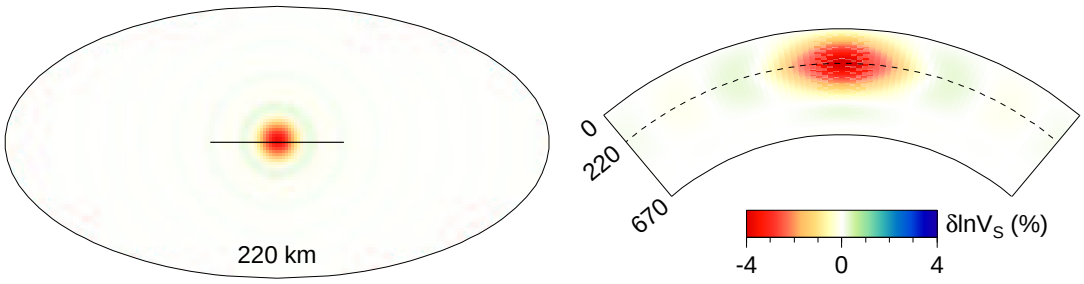


Figure 2.5: Map of lateral variations (left) and the cross section (right) of the 3-D synthetic model. The corresponding surface path of the depth cross section is shown as a black line on the map. The vertical scale of the cross section is exaggerated by a factor of 3. This model is used for the synthetic seismograms shown in Figures 2.6 to 2.11.

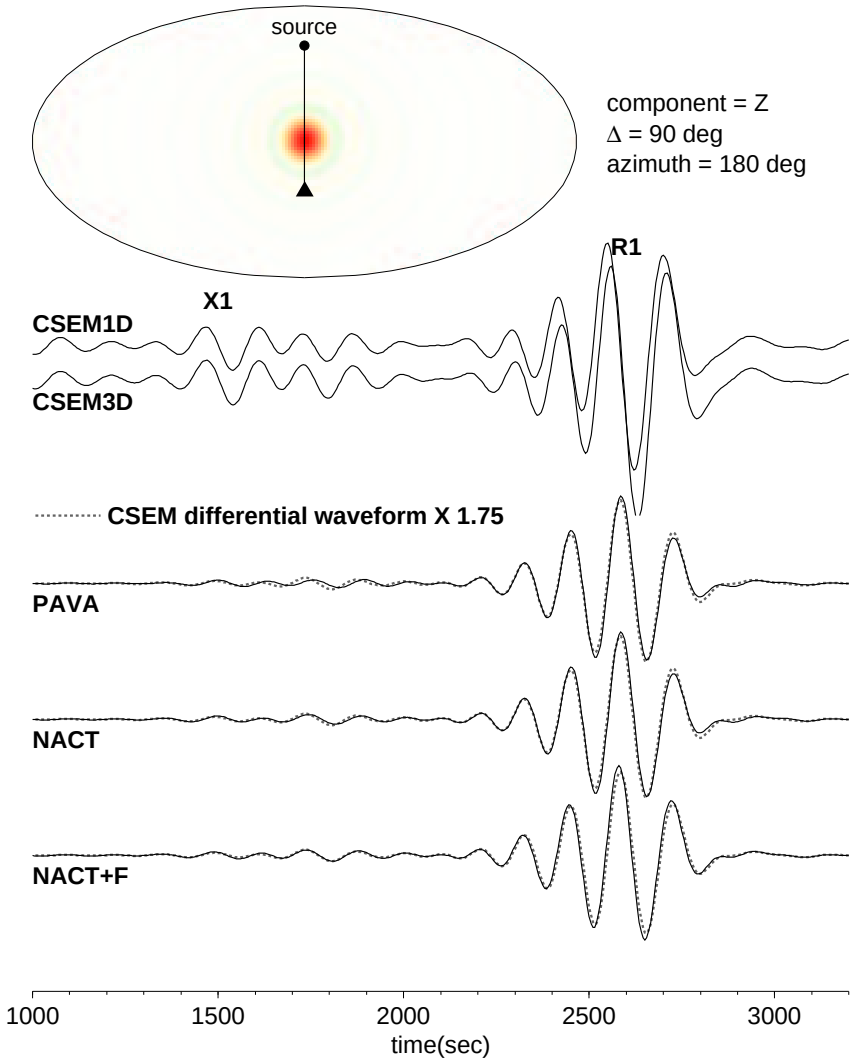


Figure 2.6: Top map: the geometrical relation of the isotropic source (black solid circle), the surface receiver (triangle) and lateral variations of hypothetic 3-D model at 220 km depth. The epicentral distance (90 degrees) and azimuth (180 degrees) for the receiver are given on the right side of the map. Note that the great circle (black line) passes through the surface center of the low velocity anomaly. Top traces: vertical component *CSEM* synthetics for the reference model (*CSEM1D*) and for the 3-D model (*CSEM3D*), the overtone phase (X1) and the fundamental mode (R1) wave-trains are shown on top of *CSEM1D*. In the bottom panels, the differential waveforms of *CSEM* (dashed line) and three normal mode based asymptotic approaches (solid line) are compared. The differential synthetics are rescaled (by multiplying 1.75 in this case). In general, the predicted perturbation seismograms from *PAVA*, *NACT* and *NACT+F* agree with *CSEM*, but predictions from *NACT* and *NACT+F* are somewhat better than those of *PAVA* for the overtone wave train.

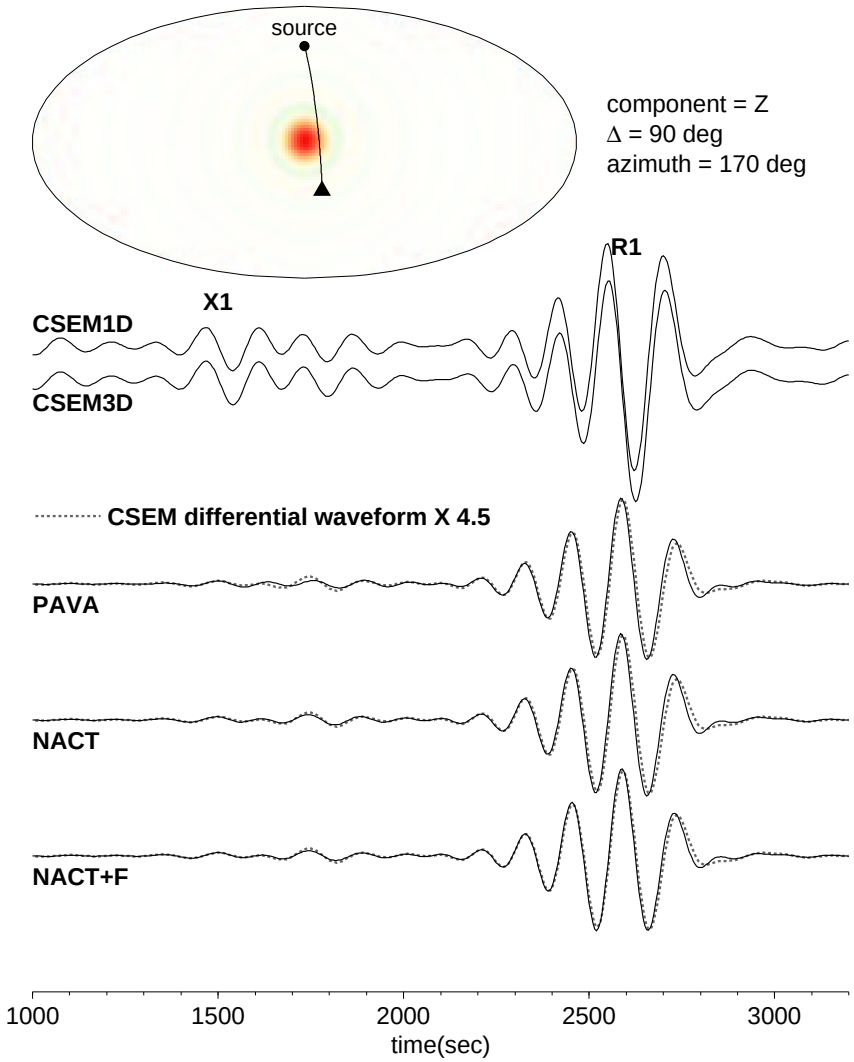


Figure 2.7: Same as Figure 2.6, but for a receiver at a smaller azimuth (170 degrees).

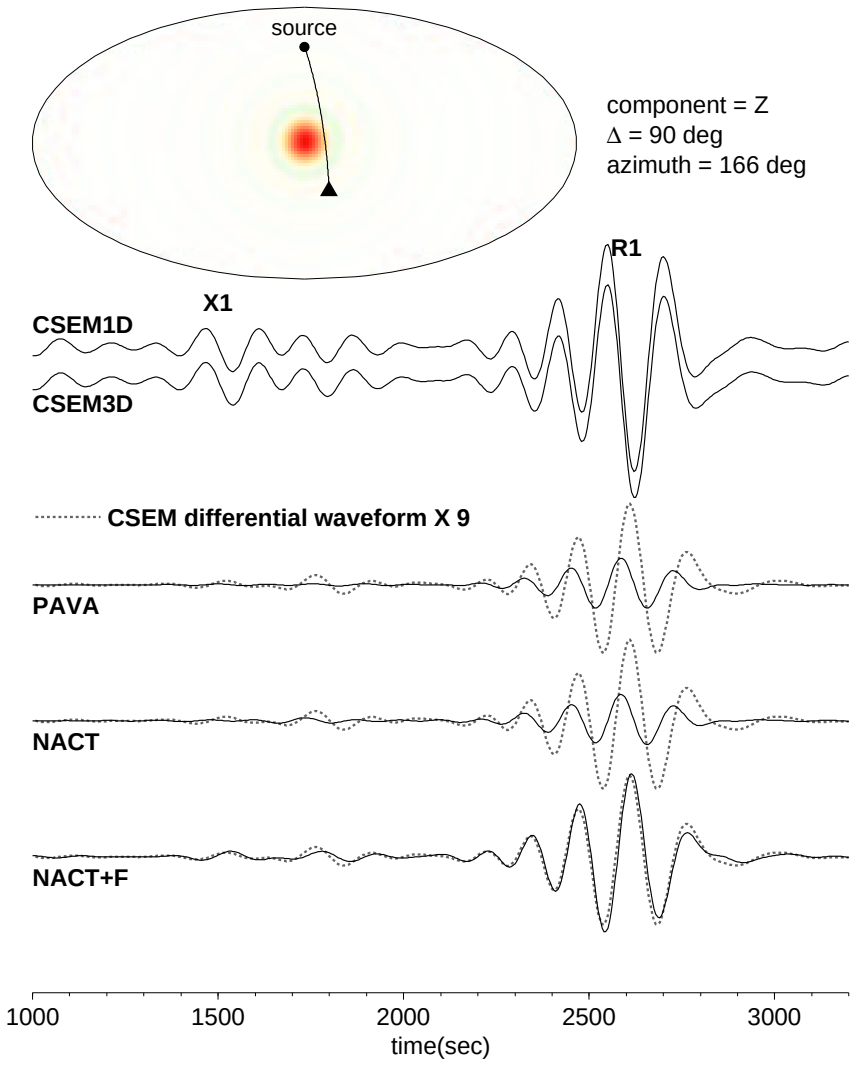


Figure 2.8: Same as Figure 2.7, but for a receiver at a slightly smaller azimuth (166 degrees). The great circle just grazes the main low velocity anomaly. Neither *PAVA* or *NACT* models the effects of the off-path anomaly, while *NACT+F*, the higher order asymptotic approximation, predicts the effects fairly well.

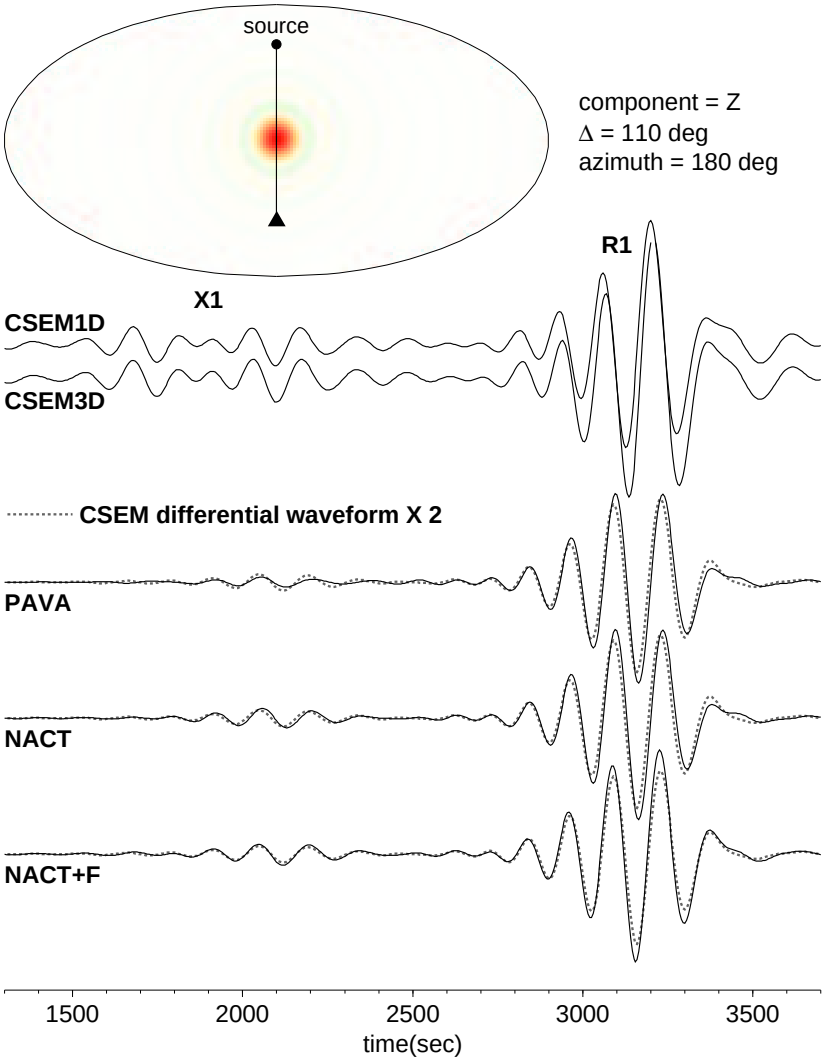


Figure 2.9: Same as Figure 2.6, but for a receiver at an epicentral distance of 110 degrees at azimuth 180 degrees.

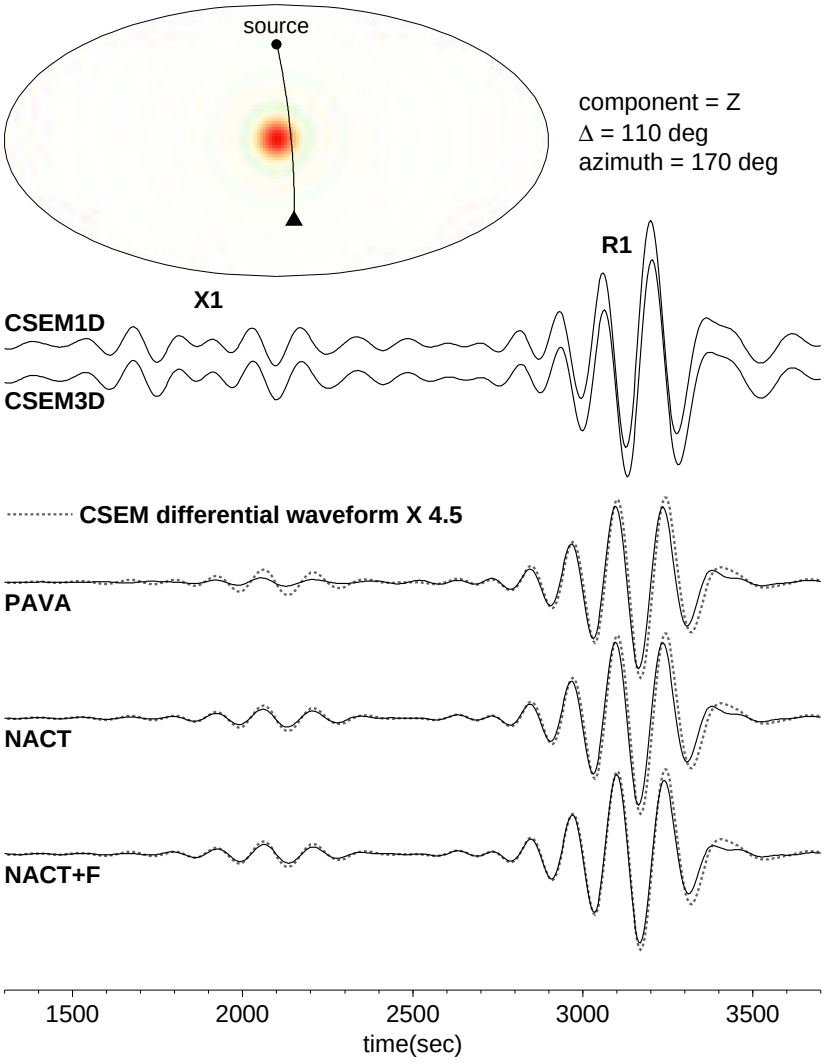


Figure 2.10: Same as Figure 2.7, but for a receiver at an epicentral distance of 110 degrees at azimuth 170 degrees.

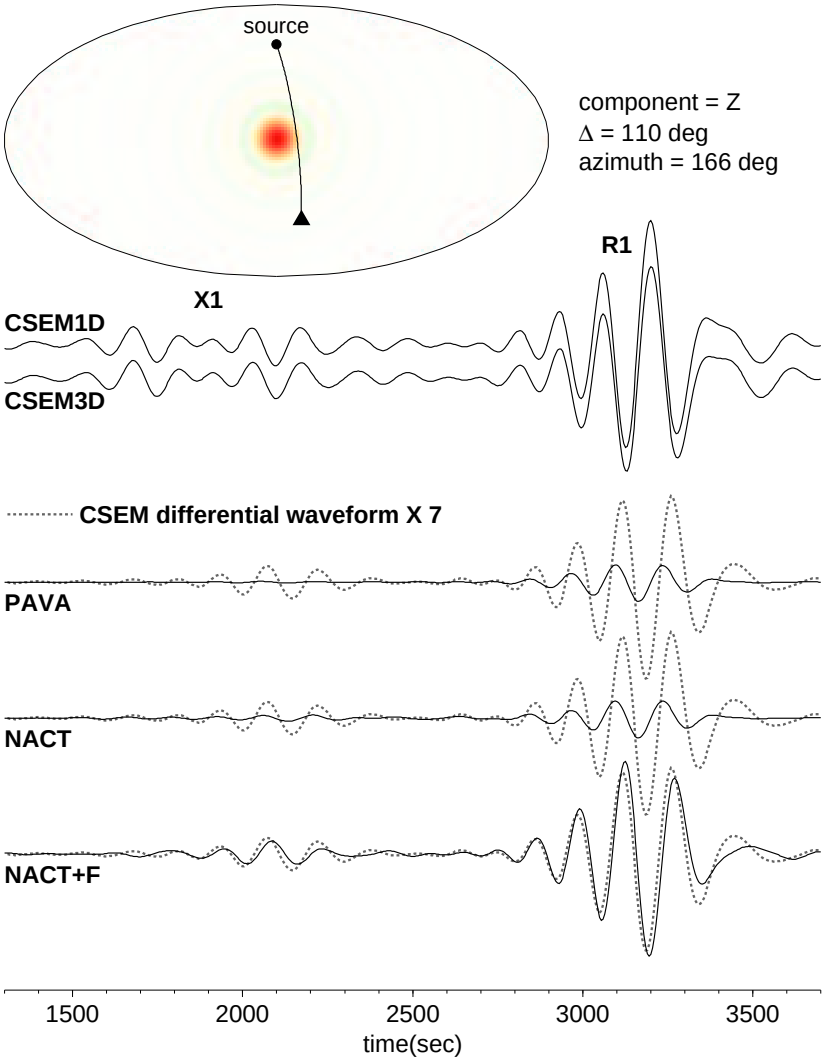


Figure 2.11: Same as Figure 2.8, but for a receiver at an epicentral distance of 110 degrees at azimuth 166 degrees.

### 3-D synthetic model: double anomalies

The second 3-D synthetic model is shown in Figure 2.12. It contains two side-by-side anomalies with opposite velocity perturbations. Both anomalies have the same maximum amplitude, $\sim 5$ % in $V_S$, and are centered at the same depth, 150 km.

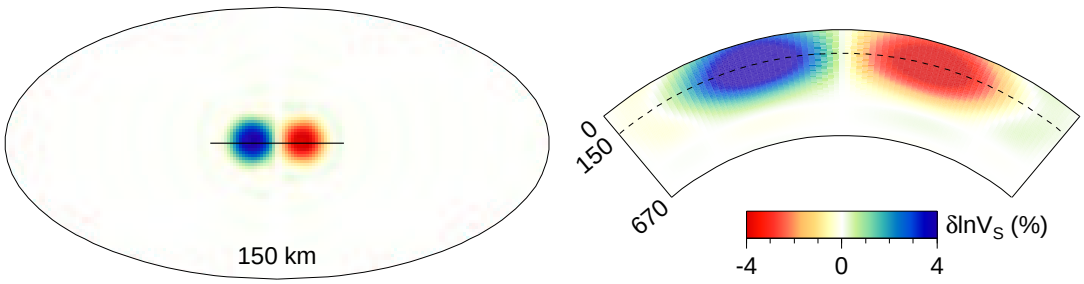


Figure 2.12: Map of lateral variations (left) and the cross section (right) of the 3-D synthetic model. The corresponding surface path of the cross section is shown in a black line on the map. The vertical scale of the cross section is exaggerated by a factor of 3.

We consider a dip-slip source in this experiment. The locations of the source and receivers and the comparison of synthetics are shown in Figure 2.13 to Figure 2.15.

When the source-receiver great circle passes through only one anomaly (Figure 2.13), the same conclusions as those from an isotropic source (Figure 2.6) hold: both *NACT* and *PAVA* give good approximations to fundamental modes, and *NACT* improves the fit to overtones.

When the source-receiver great circle passes through these two opposite anomalies (Figure 2.14), the effects of the anomalies are partly 'path-averaged out' for all modes under the *PAVA* formalism. As a result, the accuracy of *PAVA* decreases, particularly for the overtone wave-trains. Also note that the amplitudes of differential waveforms

in fundamental modes are much smaller due to the cancelling of anomaly effects.

The strong contrast between *PAVA* and *NACT* is evident when the source-receiver great circle passes through the surface centers of both anomalies, as shown in Figure 2.15. We noticed two interesting features in this particular geometry: (1) there is nearly no perturbation in the *PAVA* differential waveform (the effects of the opposite anomalies cancel each other under the *PAVA* formalism) and (2) the waveform perturbations are dominated by overtones and are explained well by *NACT* and *NACT+F*.

From the results above, we have confirmed that *NACT* is much better than *PAVA* in explaining waveform perturbations for overtone phases. We also verified, with our new code *NACT+F*, that the off-path focusing effects are predicted well by the higher order asymptotic approximation.

When we advance to higher resolution waveform tomography, the inclusion of elastic amplitude effects is potentially important. For the work presented in this thesis, *NACT+F* is used to evaluate the potential focusing/defocusing contamination in the resulting $Q$ model (Chapter 3). On the other hand, *NACT* is used routinely for elastic tomography, including $V_{SH}$, $V_{SV}$ and anisotropy. Therefore, it is important to estimate the advantage of *NACT* over conventional *PAVA* in a more statistical manner.

In this respect, using the same 3-D model, we consider 614 globally distributed receivers that cover the whole Earth surface at a 10 by 10 degree spacing. The comparisons are shown in terms of $L^2$ norm difference between the synthetics from *CSEM* and normal mode asymptotic techniques (*PAVA* and *NACT*). To identify their performance in different phases, the differences for overtone and for fundamental mode wavetrains are computed separately, and differential differences between *CSEM/PAVA* and *CSEM/NACT* are also compared.

These results are shown in Figures 2.16 to 2.19. The same features are seen in all these figures: while the differences in *NACT* and *PAVA* traces are similar for fundamental

modes, they are significantly smaller in $NACT$ for the overtone modes. These results further solidify our previous conclusions and theoretical expectations.

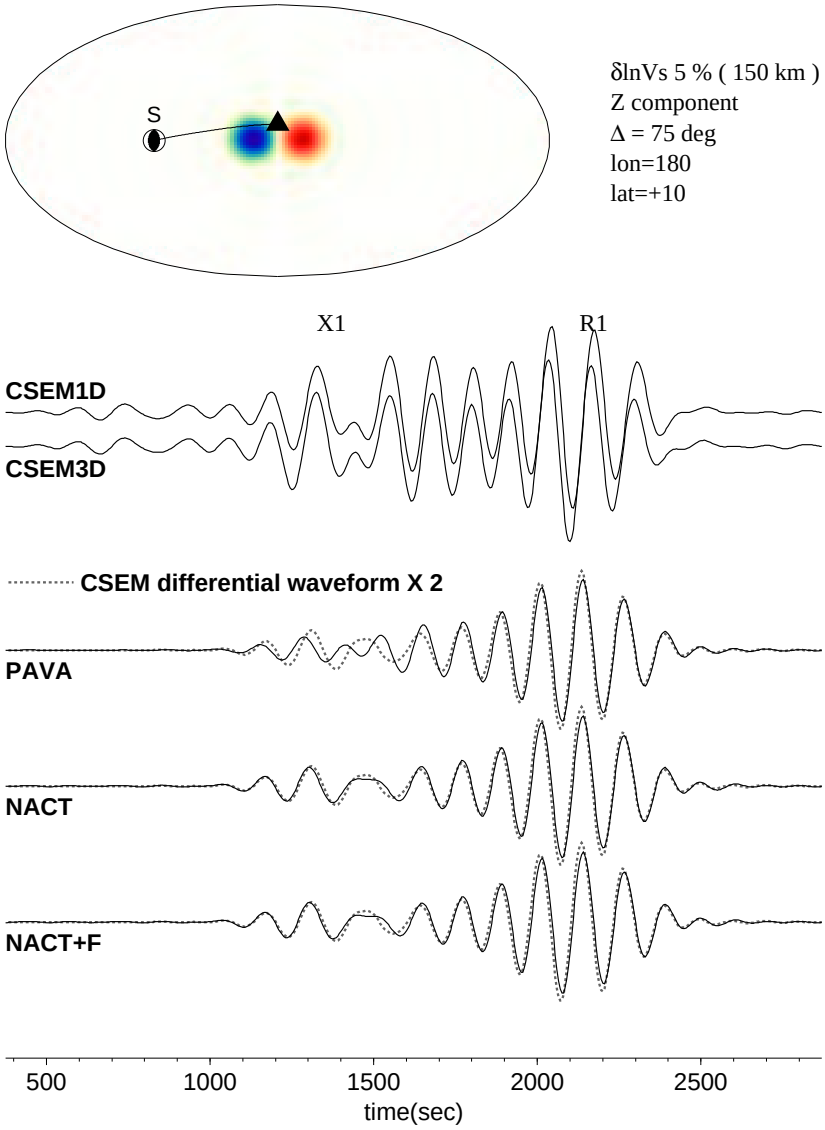


Figure 2.13: Comparison of vertical component synthetic traces for a dip-slip source. Note that the source-receiver great circle passes through only the high velocity anomaly.

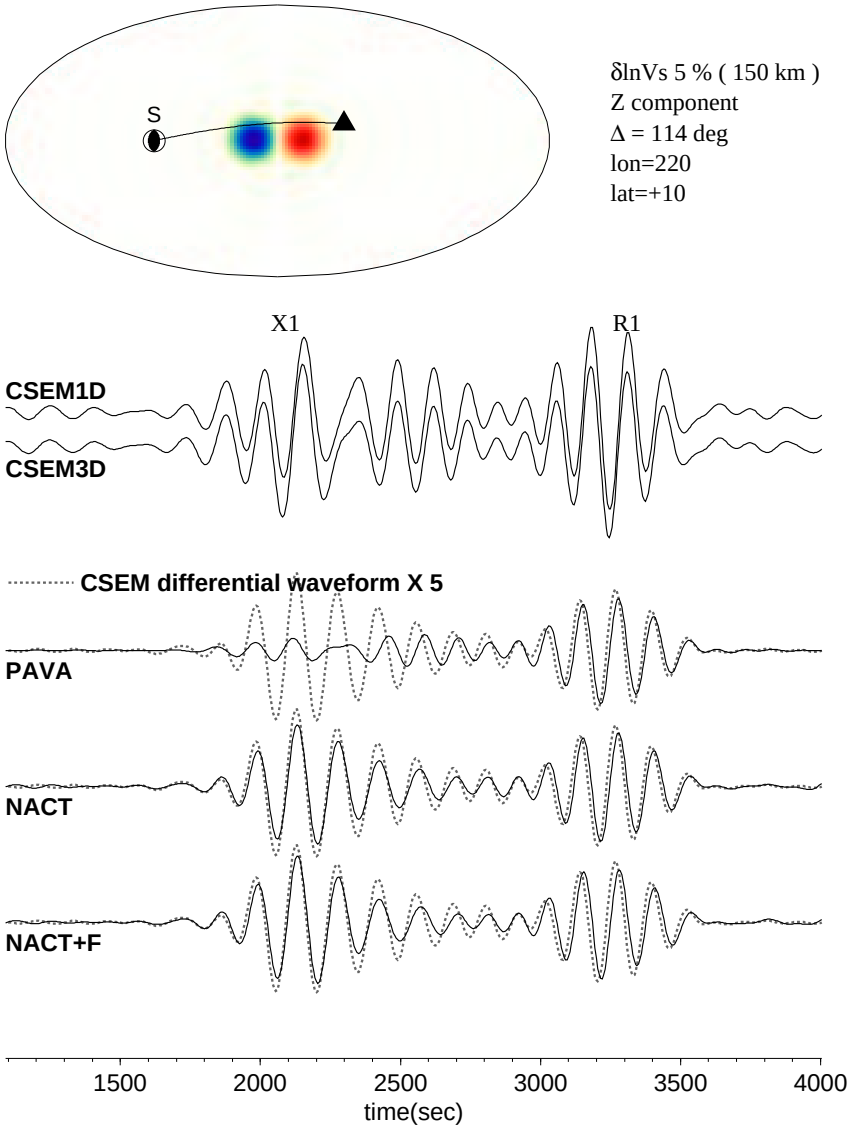


Figure 2.14: Same as Figure 2.13, but for a receiver on the great circle passing through both anomalies.

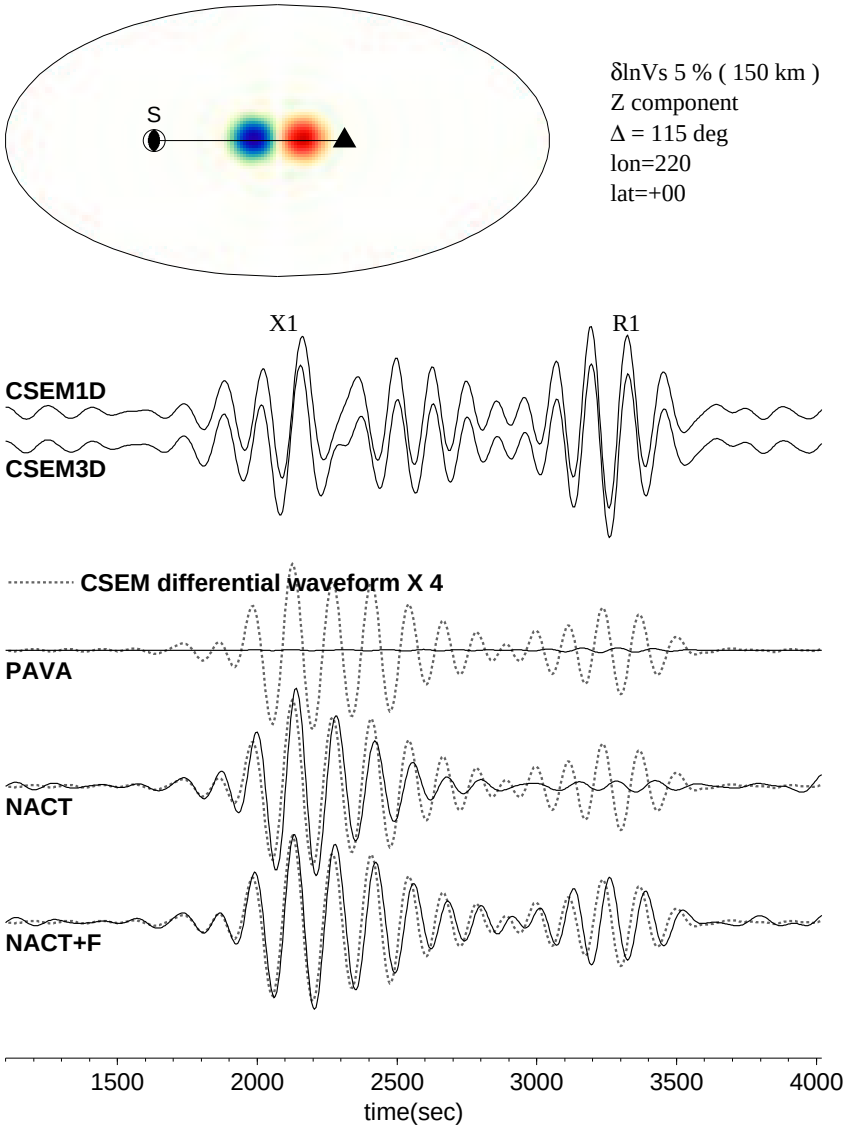


Figure 2.15: Same as Figure 2.14, but for a receiver on the great circle passing through the centers of both anomalies. In this particular geometry, the effects of the opposite anomalies cancel in the *PAVA* formalism.

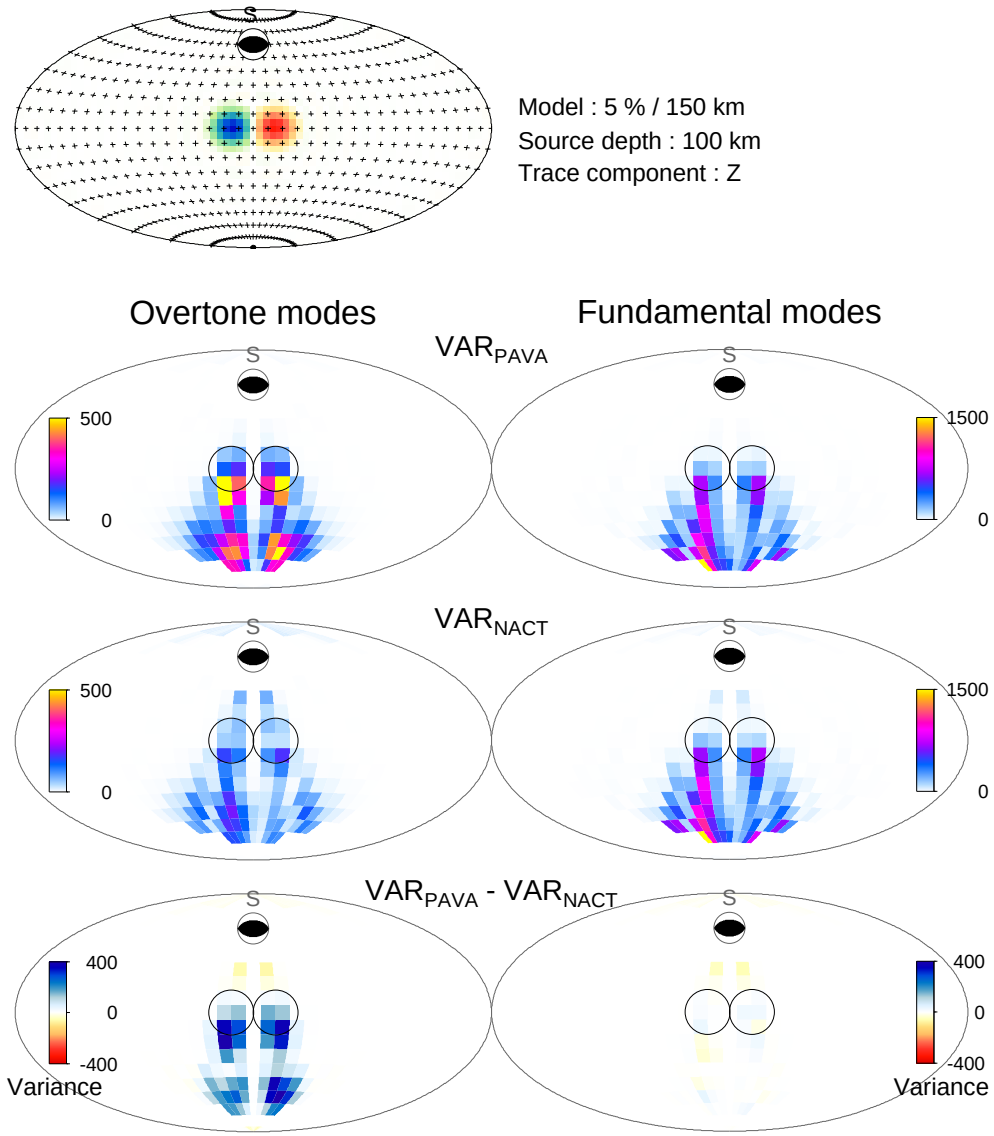


Figure 2.16: Comparison of $L^2$ norm difference between the synthetics of *CSEM/PAVA* and *CSEM/NACT*. The top map shows the 3-D $V_S$ model and source considered. The globally distributed receivers are shown as crosses. For each receiver, the $L^2$ norm difference between *CSEM* synthetics and normal mode summation techniques (*PAVA*, *NACT*) is computed, and its value is shown in color pixel on the bottom maps. The difference maps for orvertones are shown in the left column and fundamental modes in the right column. Difference maps for *CSEM/PAVA* are shown on top panels, followed by *CSEM/NACT* (middle) and their differential difference maps (bottom). The differential difference map shows that *NACT* is much more accurate than *PAVA* for the overtone phases.

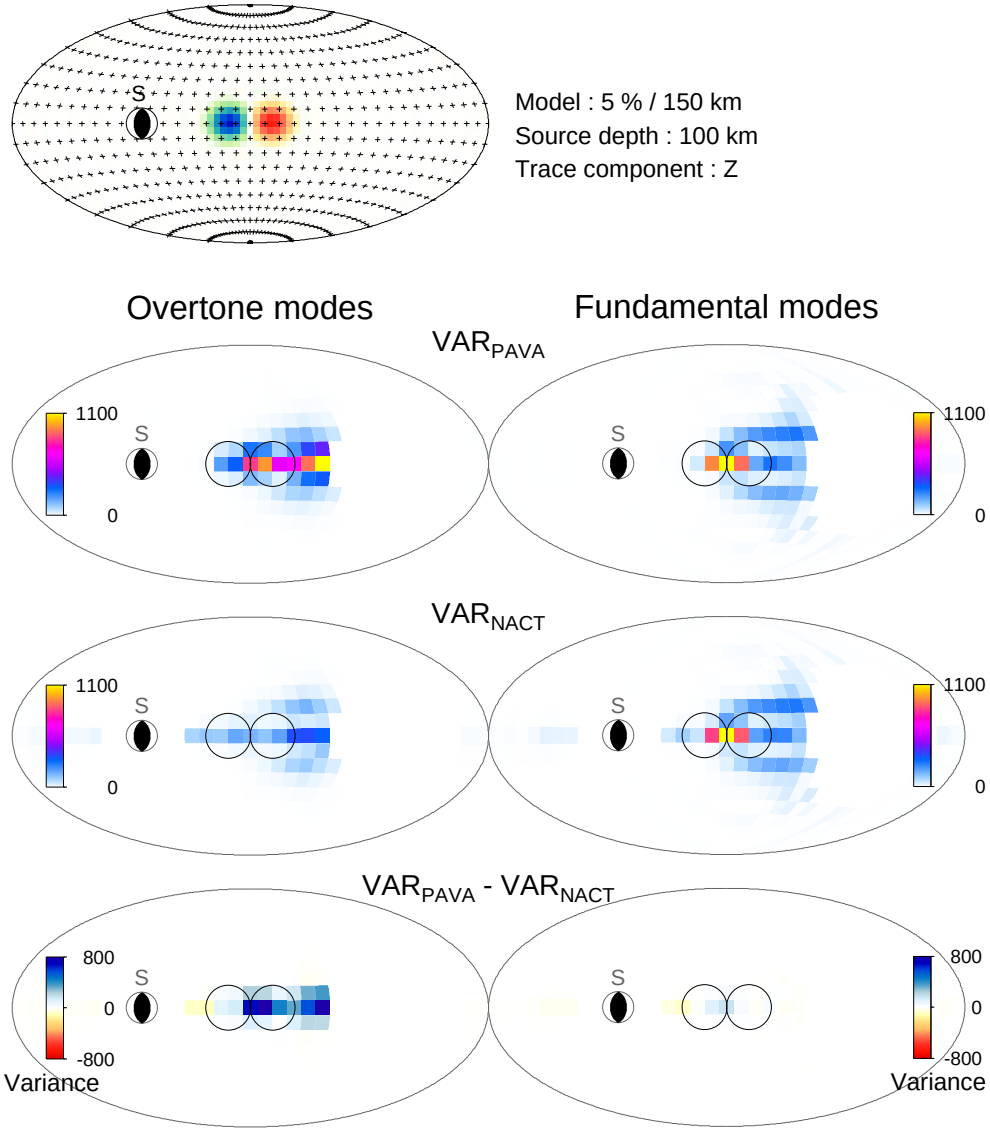


Figure 2.17: Same as Figure 2.16, but for a different source.

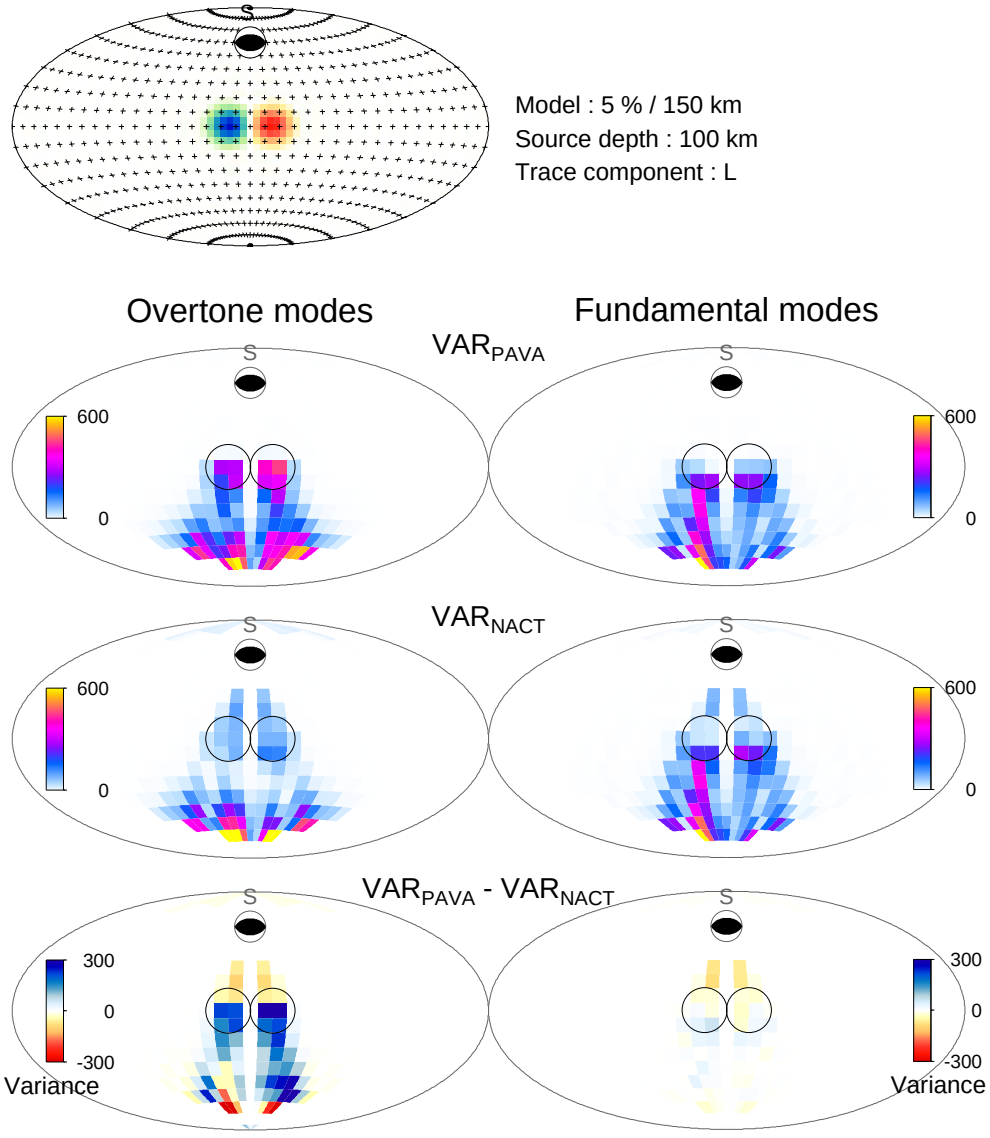


Figure 2.18: Same as Figure 2.16, but for the radial component trace.

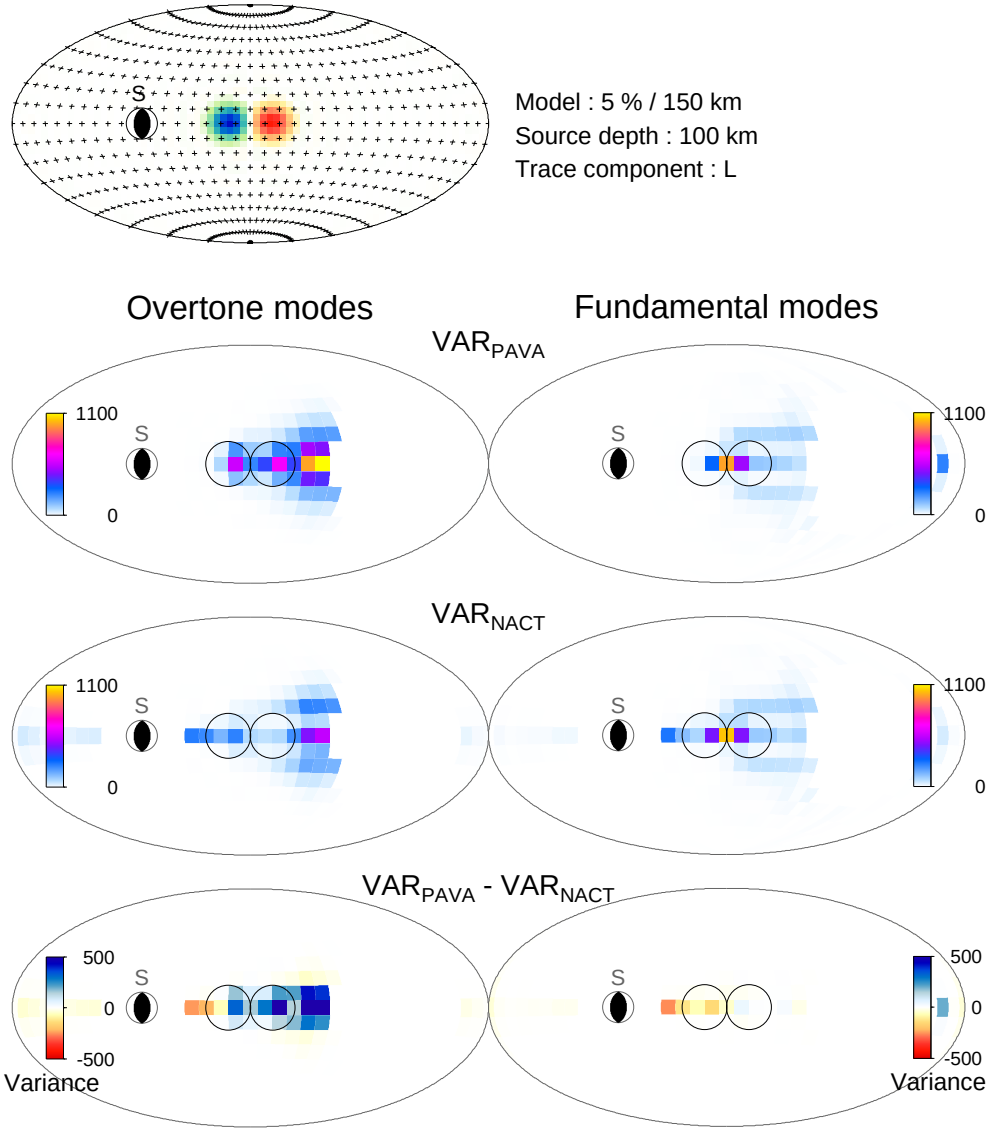


Figure 2.19: Same as Figure 2.17, but for the radial component trace.

# Chapter 3

# Q Tomography of the Upper Mantle

This chapter has been submitted for publication in *Geophysical Journal International* [*Gung & Romanowicz*, 2003] under the title: '$Q$ tomography of the upper mantle using three-component long period waveforms.'

## Abstract

We present a degree 8 three-dimensional $Q$ model (*QRLW8*) of the upper mantle, derived from three-component surface waveform data in the period range 60-400 sec. The inversion procedure involves two steps. In the first step, 3-D whole-mantle velocity models are derived separately for elastic $SH$ (transverse component) and $SV$ (vertical and longitudinal component) velocity models, using both surface and body waveforms and the $NACT$ approach (Non-linear asymptotic coupling theory). In the second step, the surface waveforms, aligned in phase using velocity models, are inverted to obtain a 3-D $Q$ model for the depth range 80-670 km. Various stability

tests are performed and the contamination from focusing effects is examined to assess the quality of *QRLW8*. We find that the 3-D patterns obtained are stable, but the amplitude of the lateral variations in $Q$ is not well constrained. The model obtained agrees with previous results in that there is a strong correlation of $Q$ with tectonics in the top 250 km of the upper mantle, with high attenuation under oceanic regions and low attenuation under continental shields. It is gradually replaced by a simpler pattern at larger depths. At the depths below 400 km, the $Q$ distribution is generally dominated by two strong minima, one under the southern Pacific and one under Africa, yielding a strong degree-2 pattern. Most hotspots are located above regions of low $Q$ at this depth. Ridges are shallow features in both velocity and $Q$ models.

## 3.1 Introduction

Resolving the 3-D anelastic structure of the mantle is important for at least two reasons: (1) $Q$ is considerably more sensitive to temperature variations than elastic velocities [*Jackson et al.*, 1992], which implies that, in principle, $Q$ tomography should be able to provide us important information on the thermal structure in the mantle and therefore its dynamics, complementing that provided by elastic tomography. In particular, it should help us distinguish the distribution of chemical versus thermal heterogeneity in the mantle [*Romanowicz*, 1995]; (2) attenuation causes dispersion in seismic velocities, and this dispersion effect needs to be taken into account when interpreting velocity models [*Romanowicz*, 1990; *Karato*, 1993].

In the last two decades, global elastic tomography has made striking progress. Significant agreements are observed among 3-D whole mantle elastic models derived by research groups using different modeling techniques and a variety of datasets [*Woodhouse & Dziewonski*, 1984; *Su et al.*, 1994; *Li & Romanowicz*, 1996; *Masters et al.*, 1996; *van der Hilst et al.*, 1997; *Grand et al.*, 1997; *Vasco & Johnson*, 1998; *Mégnin & Romanowicz*, 1999b; *Gu et al.*, 2001a]. In contrast, the progress in anelastic to-

mography has been slow, because of the inherent technical difficulties encountered in extracting anelastic signal from amplitude data.

To date, only a few 3-D global attenuation models have been published. Several attempts at retrieving the distribution of even order heterogeneity in upper mantle $Q$ have been made using normal mode data [*Suda et al.*, 1991; *Rould et al.*, 1990] or propagating Rayleigh wave data [*Romanowicz*, 1990; *Durek et al.*, 1993]. The first complete 3-D $Q$ model of the upper mantle, *QR19* [*Romanowicz*, 1995], which includes both even and odd heterogeneities, provided lateral resolution equivalent to degree $\sim 5$ in a spherical harmonics expansion, and remained largely qualitative. In that study, attenuation coefficients were measured in the spectral domain, for low-frequency (100-300 s) Rayleigh waves on multiple orbits, using a method designed to minimize the effects of focusing and scattering due to wave propagation in the complex 3-D elastic earth, as well as the effect of uncertainties in the source moment and radiation pattern. More recently, *Billien et al.* [2000] derived global Rayleigh wave attenuation maps, from simultaneous inversion of phase and amplitude data. *Selby & Woodhouse* [2002] presented a sets of 3-D $Q_\mu$ models of the upper mantle based on amplitude measurement of minor and major arc Rayleigh waves in the period range 70-170 s. Several authors have also developed methods to extract attenuation information from body wave data. *Bhattacharyya et al.* [1996] analyzed differential *SS* - *S* waveforms using a multitaper frequency domain technique to measure the variation of attenuation in the upper mantle. *Reid et al.* [2001] applied a differential waveform-fitting method to multiple *S* phases (*SS* - *S* and *SSS* - *SS*), to constrain the elastic and anelastic structure of the mantle simultaneously. *Warren & Shearer* [2002] analyzed *P* and *PP* spectra to map lateral variations in *P* wave attenuation in the top 220 km of the upper mantle. While the source effects are reduced in differential body wave amplitude measuring techniques, the depth resolution of the resulting models is limited.

Although the similarities between these global $Q$ models are much less clear than those in global elastic models, there are several common features in the shallow mantle

(depth $< 250$ km): low $Q$ beneath active tectonic regions, high $Q$ beneath stable shield regions, and, in general, correlation between slow velocities and high attenuation. The $Q$ variations are correlated with tectonic features in the shallow mantle.

In theory, waveform inversion techniques used in elastic tomography [*Woodhouse & Dziewonski*, 1984; *Li & Romanowicz*, 1996] can be applied to anelastic tomography as well. However, the changes in waveforms due to elastic effects (focusing and scattering) are commensurate with those due to intrinsic attenuation, which makes it a challenge to isolate the attenuation effects on seismograms. To better identify these interfering effects, most $Q$ measurements are usually made in the spectral domain [*Romanowicz*, 1995; *Bhattacharyya et al.*, 1996; *Durek & Ekström*, 1996]. The drawback of spectral approaches is that they require isolated phases on seismograms, which limits the resolution that can be attained in the mantle.

In this study, we show that $Q$ tomography based on waveform inversion is feasible, if reliable elastic models and careful data selection are utilized to minimize the interfering effects. We present the results of a global tomographic inversion for lateral variations in $Q\mu$ in the upper mantle, using a dataset of three-component surface waves in the period range 60-400 s. Unlike our previous $Q$ studies, in which measurements were performed in the spectral domain [*Romanowicz*, 1990; *Romanowicz*, 1995], the present modeling technique is based on the waveform methodology developed by *Li & Romanowicz* [1995] (hereinafter referred to as LR95), with appropriate modification to convert the code from elastic to anelastic inversion, and applied to three-component data.

We first describe the dataset and inversion procedures, explore the mutual influence of elastic and anelastic effects with a test inversion based on synthetic data, and present a degree 16 $V_{SV}$ mantle model, which will be used for phase correction in $Q$ tomography of Rayleigh wave data. In order to account for significant transverse isotropy in the upper mantle [*Montagner & Tanimoto*, 1990; *Ekström & Dziewonski*, 1998; *Gung et al.*, 2003], the phase correction of Love wave data is based on a $V_{SH}$

model, *SAW24B16* [MR00]. Then we present a degree 8 $Q$ model, *QRLW8*, derived after phase correction using Rayleigh and Love waveform data measured on all three components. Finally, we assess the model stability by various experiments. For the geodynamic implications of *QRLW8*, please refer to Chapter 4.

## 3.2 Data

We restrict the modeling of 3-D $Q$ variations to the upper mantle. The strong sensitivity of surface waves to the upper mantle makes them appropriate for this purpose.

The surface wave dataset is composed of two parts. The first part consists of fundamental mantle Love waves of the first and second orbits (*G1* and *G2*), low-pass filtered with a cutoff frequency of 1/80 $Hz$ and a corner frequency of 1/100 $Hz$. They were recorded on global networks for earthquakes occurring between 1977 and 1992. This hand-picked dataset is a subset of the waveform dataset used in the development of the degree 12 shear velocity model of the whole mantle *SAW12D* [LR96] and the subsequent higher degree model *SAW24B16* [MR00].

To further improve the coverage and depth resolution, we complemented this dataset with newly processed waveforms, which, in addition to transverse component data (Love waves), include data from vertical and radial components (Rayleigh waves). Besides the fundamental waves of the first and second orbits, this data set also includes overtone phases. Events of magnitude greater than $Mw$ 5.5 are considered. These new events were recorded at IRIS stations for 249 events for the time period 1995-1999, and at Geoscope stations for 440 events for the time period 1993-1999. Figure 3.1 shows the geographical distribution of events in the dataset. All selected events are properly time-isolated to avoid interference with other events. To prevent possible complications from the long source-time duration, very large events ($M_0 > 10^{20} Nm$) are not used. Seismograms recorded near the epicenters or their antipodes ($\Delta < 15^o$ or $\Delta > 165^o$) are not selected, since the asymptotic theory breaks down near $\Delta = 0^o$

or $\Delta = 180^o$ [*Romanowicz*, 1987a].

Compared to the first data set, the second data set is low-pass filtered with higher cutoff frequency and corner frequency (1/60 $Hz$ and 1/80 $Hz$ respectively), in order to improve the resolution in the shallow mantle.

Figure 3.2 shows the sensitivities of Love and Rayleigh waves to earth structure at periods of 100 s and 200 s. Love waves are highly sensitive to shallow structure, and Rayleigh waves provide constraints in the intermediate depth range of the upper mantle, complementary to the information provided by Love waves. Since the depth of peak sensitivity of fundamental Rayleigh waves increases significantly with increasing period, we expect that better depth resolution in the upper mantle can be obtained using a combination of Rayleigh and Love wave data.

We adopt the individual wavepacket technique first proposed by *Li and Romanowicz* [LR96]. Compared to the more standard full trace approach, this wavepacket technique has the advantage of allowing us to assign weights to wavepackets with different amplitudes, thereby preventing the inversion from being dominated by data with the largest amplitudes [*Mégnin & Romanowicz*, 1999a]. From the point of view of $Q$ inversion, the wavepacket technique also guarantees more reliable amplitude information, since only those portions of data associated with major energy arrivals are selected.

To overcome the drawback of slow data acquisition with manual wavepacket picking, we developed an autopicking algorithm to gather a sufficient dataset in a reasonable amount of time. While the original data set in LR96 was hand-picked, the second dataset was collected using this algorithm. An example of the waveform data selected by autopicking is shown in Figure 3.3. The complete data selection procedure is as follows:

(1) Compare the raw data with synthetics obtained by mode summation for a reference model combining elastic *PREM* [*Dziewonski & Anderson*, 1981] and anelastic *QL6* [*Durek & Ekström*, 1996]. Noisy and glitchy traces are first eliminated. About 25%

of vertical component and 60% of transverse and longitudinal components of data traces available are rejected. Because of the noisy character of horizontal component records, more horizontal component date are rejected (Figure 3.3).

(2) The data trace is broken into individual wavepackets of major energy arrivals. On a packet-by-packet basis, the variance residuals (normalized by data and synthetics, independently), and ratios between the maximum amplitude of observed and synthetics are used as criteria for data elimination. We reject data whose normalized variance is larger than 2, or whose amplitude ratio is larger than 2 or smaller than 0.5. These criteria allow us to remove wavepackets that are noisy or strongly affected by unwanted effects, such as focusing or complex source process. About 50% of the wavepackets are rejected at this stage.

(3) The qualified data in the previous two steps are used in elastic tomography. Because phase alignment between observed and synthetic waves are important before $Q$ inversion (detailed in Section 3.4), stricter data selection criteria based on waveform correlation are applied for the $Q$ inversion. Specifically, we compare the waveform correlation between data and synthetics computed in the 3-D velocity models obtained in the first step, and reject data with correlation less than 0.5. As a result, about 30% of data used in the velocity inversion are excluded from the following $Q$ inversion.

15,777 transverse (Love waves), 4820 radial and 10,770 vertical component (Rayleigh waves) wavepackets are used in the $Q$ inversion. The coverage obtained with these data is shown in Figure 3.4, where it is expressed as the logarithm of the sampling ray length (in degree) in each $10^o$ by $10^o$ cell, corrected for latitude. To prevent the resulting model from being biased by the inherent irregular distribution of data coverage, a coverage dependent weighting scheme is applied. For each wavepacket, we compute a measure of redundancy with respect to all the other wavepackets in the dataset. We then assign to the wavepacket a weight inversely proportional to the square root of the redundancy estimate. Details of this procedure are given in LR96.

## 3.3 Theory

Based on asymptotic expressions of *Romanowicz* [1987a] and *Li & Tanimoto* [1993], *Li & Romanowicz* [1995] developed the non-linear asymptotic coupling theory (*NACT*), in which long period acceleration seismograms can be represented as

$$u(t) = \sum_K A_K \exp(i\widehat{\omega}_K t) + u_1(t). \tag{3.1}$$

The first term on the right hand side of (3.1) is the exact result of conventional path-average approximation (*PAVA*) [*Woodhouse & Dziewonski*, 1984; *Tanimoto*, 1986]; the second term $u_1(t)$ represents the across-branch modal coupling effect ignored by the *PAVA*. As demonstrated in Chapter 2: since across-branch coupling provides 2-D kernels appropriate for body waveforms that sample the deep mantle, *NACT* is significantly more powerful in resolving 3-D structure in the mid and lower mantle. While the *NACT* sensitivity kernels for deep-sampling body waves are very different from those of *PAVA*, they are similar for surface waves. Moreover, the dense data coverage in the upper mantle can also reduce the bias caused by horizontal averaging of the *PAVA* method. The whole mantle velocity models used in this study are derived using *NACT* with both body waves and surface waves. On the other hand, only surface waves are analyzed for the upper mantle $Q$ structure. We will, for now, apply *PAVA* instead of *NACT* during the $Q$ inversion, i.e. the second term on the right hand side of (3.1), $u_1(t)$, will be neglected. This represents considerable computational savings. In the future, as we proceed to include body waves, *NACT* kernels will need to be considered.

In (3.1), the summation is taken over all the multiplets with $A_K \equiv \sum_m R_K^m S_K^m$ and

$$\widehat{\omega}_K = \omega_K + \delta\widetilde{\omega}_K \tag{3.2}$$

where $\omega_K$ is the complex eigenfrequency of multiplet $K$ in the reference symmetrical earth model, and $\delta\widetilde{\omega}_K$ is the *PAVA* apparent frequency shift on the minor arc given by

$$\delta\widetilde{\omega}_K \;=\; \frac{1}{\widehat{SR}} \int_S^R \delta\omega^K_{local} d\phi, \tag{3.3}$$

where the integral is taken along the great circle path between the source $S$ and the receiver $R$, $d\phi$ denotes the differential angular distance element, $\widehat{SR}$ is the total length of the path. $\delta\omega^K_{local}$ is the local frequency introduced by *Jordan* [1978], and is given by

$$\delta\omega^K_{local} \;=\; \frac{1}{2\,\omega_K} \left[ \int_0^{R_\oplus} \delta\mathbf{m}(r,\theta,\phi) \cdot \mathbf{M}_K(r) r^2 \, dr \;-\; \sum_d r_d^2 \, h_d(\theta,\phi) \, H_K^d \right], \tag{3.4}$$

where $R_\oplus$ is the radius of the Earth, $\delta\mathbf{m}$ represents the volumetric perturbations to the elastic reference model, $h_d$ the perturbations in the radius $r_d$ of the $d^{th}$ radial discontinuity in the reference model. The kernels $\mathbf{M}_K(r)$ and $H_K^d$ may be evaluated directly using eqs $(A36) - (A42)$ of *Woodhouse* [1980].

When anelastic dispersion effects are neglected, the complex perturbation in the eigenfrequency can be written in the form (e.g. *Dahlen & Tromp* [1998]):

$$\delta\widetilde{\omega} \;=\; \delta\widetilde{\omega}_0 \;+\; i\omega_0\delta\frac{1}{2Q}, \tag{3.5}$$

where the real part, $\delta\widetilde{\omega}_0$, represents the frequency shift with respect to $\omega_0$, the eigenfrequency in the reference elastic model, and is related to the elastic variation in Earth structure; $\delta\frac{1}{2Q}$ is the anelastic perturbation with respect to the reference attenuation model.

In this study, we do not explicitly correct for focusing effects due to wave propagation in a 3-D elastic model. Although these effects can be strong [*Romanowicz*, 1994a], they

depend on the lateral gradients of the 3-D elastic model, which in turn depend on the short-wavelength features of the elastic model and are not presently well constrained. However, *Romanowicz* [1995] has demonstrated that the focusing/defocusing effects are small in the retrieved low degree ($\sim$ 5-6) $Q$ map. More recently, *Selby & Woodhouse* [2000] and *Selby & Woodhouse* [2002] have also shown that amplitude variations are dominated by intrinsic attenuation at long wavelengths, specifically, for spherical harmonics degrees up to degree $\sim 8$. To stay within the range where these unmodeled effects are small, we limit our $Q$ model to degree 8 and also perform a careful data selection, as was discussed in the previous section.

Comparison of models obtained using different components of data, bootstrapping tests and examination of the contamination from focusing effects, as will be seen, confirm the stability of the main features of our models.

### 3.3.1 Model Parameterization

Our velocity and $Q$ models are both parameterized in spherical harmonics for lateral variations and cubic b-splines [MR00] for depth dependence. The velocity model is expressed as perturbations from the spherically symmetric model *PREM*, and is parameterized radially in 16 cubic b-splines for the whole mantle, with the same knot distribution as used in *SAW24B16*. The $Q$ model is expressed as perturbations from the reference $Q$ model, and is parameterized radially in 7 cubic b-splines defined from the depth of 80 km to the bottom of the upper mantle (Figure 3.5).

$$\delta \mathbf{m_v}(r,\theta,\phi) \;=\; \delta \ln v(r,\theta,\phi) \;=\; \sum_{k=1}^{16} \sum_{s=0}^{v_{smax}} \sum_{t=-s}^{s} {}_k a_s^t \, B_k(r) Y_s^t(\theta,\phi), \tag{3.6}$$

$$\delta \mathbf{m_q}(r,\theta,\phi) \;=\; \delta q_\mu(r,\theta,\phi) \;=\; \sum_{k=1}^{7} \sum_{s=0}^{q_{smax}} \sum_{t=-s}^{s} {}_k b_s^t \, B_k(r) Y_s^t(\theta,\phi), \tag{3.7}$$

where $\delta \mathbf{m_v}$ and $\delta \mathbf{m_q}$ are the volumetric perturbations in $S$ velocity and attenuation,

$v_{smax}$ and $q_{smax}$ are the maximum degrees in the spherical harmonics parameterization for velocity and $Q$ models respectively, $B_k(r)$ are cubic b-splines [MR00], $Y_s^t(\theta, \phi)$ are fully normalized spherical harmonics [*Edmonds*, 1960], $q_\mu = Q_\mu^{-1}$, and ${}_ka_s^t$ and ${}_kb_s^t$ are the model coefficients to be determined in the inversion.

In both models, the knots are distributed with progressively shorter spacing at the shallower depths to reflect the radial resolution of our data. The maximum degree of the spherical harmonics expansion is 16 for the $SV$ velocity model, and 8 for the $Q$ model, for the reasons discussed above.

### 3.3.2 Inversion

The partial derivatives of a seismogram with respect to model coefficients, ${}_ka_s^t$ and ${}_kb_s^t$, can be derived from eqs (1) to (7). The inverse problem is then solved using a stochastic formalism [*Tarantola & Valette*, 1982], and the finite-dimensional model is obtained by the recursive application of a Newton scheme to the Fréchet derivatives of the $L^2$ norm objective function. We refer the reader to LR96 for the details of the inversion.

Elastic and anelastic model coefficients are solved separately. We first solve for the 3-D elastic model, which is then used to align the phase of data and synthetics prior to the $Q$ inversion. The reason for this sequence of inversions will be given in the next section, which discusses the results of test inversion experiments.

Source parameters are kept fixed as given in the CMT catalog [*Dziewonski et al.*, 1981]. We discuss this point in a later section.

## 3.4 Inversion experiments and inversion procedure

For elastic tomography based on waveform data, the phase deviation between observed data and synthetics is the most useful information, in that the variance reduction is mainly achieved by means of phase alignment. Although attenuation heterogeneities could cause phase distortion in the waveform, their main effect is in the amplitudes. This has the following consequence when using waveform data for elastic and anelastic tomography: whereas amplitude variations due to anelastic heterogeneities can be ignored in elastic tomography, the phase shift caused by elastic heterogeneities needs to be considered in anelastic tomography. Indeed, a correct point-by-point matching of amplitudes of synthetic and observed waveforms is impossible when their phases are not well aligned. If the phases are not aligned, the most efficient way to minimize the variance between data and synthetics is to decrease the amplitudes of synthetics, thus biasing the derived $Q$ model. It is therefore essential that phase alignment should be achieved before a $Q$ inversion.

### 3.4.1 Inversion experiments

We implement an inversion experiment to test these assertions, and explore the interaction between elastic and anelastic tomography. The procedure and results are as follows:

(1) Generate the predicted radial component of Rayleigh waves from a test input model. The coverage and frequency band of synthetic data are exactly the same as for the data used in this study. The test input model contains two levels of degree 8 heterogeneities both in velocity and attenuation. The heterogeneities are distributed around depth of 150 km (5% for $\delta \ln V_S$ and 50% for $\delta \ln Q^{-1}$) and 400 km (3% for $\delta \ln V_S$ and 50% for $\delta \ln Q^{-1}$) respectively, as shown in Figure 3.6a. We note that, given these elastic and anelastic variations, the mean variance of synthetic data due to $Q$ heterogeneities is only about 6.4% of the total variance resulting from both the $Q$

and velocity heterogeneities. Therefore, we do not expect a large variance reduction due to $Q$ structure when using real data.

(2) Invert for a velocity model based on the synthetic dataset, without modeling the effects of attenuation heterogeneities. The same inversion technique used for real data is applied. The result (Figure 3.6b) shows that both the lateral variations and amplitudes of the input velocity model are well recovered. This confirms that the amplitude variations due to anelastic perturbations are not an impediment to elastic waveform tomography.

(3) Invert for attenuation model. Two experiments are conducted: one with and one without phase correction for velocity heterogeneities. Figure 3.6c shows that the input $Q$ images at both depths are well recovered, when phase correction is applied prior to the $Q$ inversion (using the retrieved velocity model in the last procedure). When the elastic heterogeneities are ignored, the input $Q$ model, especially its deeper structure, is poorly resolved (Figure 3.6d). These results show that the phase shift correction for the 3-D elastic model is a prerequisite for $Q$ tomography using waveforms.

In the above experiments, the elastic effects in the amplitudes are not modeled. The potential contamination on the resulting $Q$ model from focusing effects will be evaluated in a later section.

### 3.4.2 Inversion procedure

Accordingly, the inversion procedure based on the real data is set as follows:

(1) Invert for velocity models. Since strong anisotropy in the upper mantle has been observed in many studies [*Montagner & Tanimoto*, 1990; *Ekström & Dziewonski*, 1998], we perform separate inversions of $V_{SH}$ (transverse component) and $V_{SV}$ (vertical and longitudinal component) data to better account for the elastic effects in the following $Q$ inversion. For the elastic inversions, we consider a dataset comprising both

surface waves and body waves and we invert for whole mantle structure using *NACT* kernels. We already have a satisfactory $V_{SH}$ elastic model, *SAW24B16*. Starting from *SAW24B16*, truncated to degree 16 (the variations beyond degree 16 are essentially insignificant, as long as we ignore the focusing effects), we invert for a degree 16 $V_{SV}$ model. In addition to Rayleigh wave data, a $V_{SV}$ component body wave data set, composed of about 38,000 wavepackets selected on the vertical and longitudinal components, is also used for this whole mantle parameterized $V_{SV}$ model. Before the inversion, the crustal effects are corrected for by using the global crustal model, *CRUST 5.1* [*Mooney et al.*, 1998].

(2) Invert for a degree 8 $Q$ model using three-component waveforms simultaneously. To prevent the $Q$ model from being biased by unmodeled elastic effects in the phases, waveform correlation is used as a data selection criterion before $Q$ inversion, as described in Section 2. To further emphasize the contribution of data whose phase is well-aligned, an additional weighting factor proportional to the waveform correlation is assigned to each wavepacket during the $Q$ inversion. Each data set (vertical, longitudinal and transverse components) is weighted such that the weighting of Love waves and Rayleigh waves is balanced on the one hand, and, on the other hand, so is the weighting of vertical and radial component of Rayleigh waves. The $V_{SH}$ model is used for the phase corrections on Love wave data, and the $V_{SV}$ model on Rayleigh wave data.

Inversion for $Q$ is limited to the depth range 80-670 km, because resolution is poor at shallower depths. Moreover, since $Q$ in the crust is very large, the sensitivity of long period surface wave data to lateral variation of $Q$ in the crust is relatively small, even though there are significant lateral variations of $Q$ in the crust (e.g. *Mitchell* [1995]).

Regarding crustal corrections, we consider the radially symmetric model *QL6* and replaced its flat *moho* by undulations, according to model *CRUST 5.1*, to account for the distinct $Q$ values across *moho* (e.g. *PREM*, *QL6*).

## 3.5 Results

In what follows, we present our results both for velocity models and $Q$ models, and then discuss the results of various experiments performed to test the stability of the $Q$ models. The discussion of velocity models will be brief, since the $Q$ model is the focus of this chapter.

### 3.5.1 Velocity Models

Figure 3.7 show the lateral variations of $V_{SV}/SAW16BV$ and $V_{SH}/SAW24B16$ models at several depths in the upper mantle. In general, the main features in these two models are similar. The main difference is in the central Pacific at a depth range around 200 km, where opposite variations of $V_{SH}$ (faster than average) and $V_{SV}$ (slower than average) are observed. Besides this well documented anisotropic feature [*Montagner & Tanimoto*, 1990; *Ekström & Dziewonski*, 1998], some other interesting features are also observed in the comparison between $V_{SH}$ model and $V_{SV}$ model. For example, a faster than average signature of continental roots in $V_{SV}$ model fades off at a shallower depths ($\sim$ 200-250 km) compared to that in $V_{SH}$ model ($\sim$ 350-400 km). These features have been confirmed by performing a joint anisotropic inversion using three-component waveform data, in which the effects of $\delta V_{SV}$ on toroidal modes and $\delta V_{SH}$ on spheroidal modes are also incorporated. please refer to Chapter 5 for detailed discussion on the tectonic corresponding implications.

### 3.5.2 3-D $Q$ model

Three different 1-D $Q$ models have been tested as starting models (Figure 3.8). These include *QL6*, *QR19* (degree 0 terms) and *QL6c* (a smoothed version of *QL6*). Although the inverted $Q$ models show similar patterns, those from smooth 1-D $Q$ models are more stable across 220 km discontinuity because the smooth parameterization

is more compatible with the spline parameterization in depth of the 3-D $Q$ model. For simplicity, we will only display the results derived from *QL6c*. Because we do not adjust the seismic moment, which trades off with radial $Q$ structure, we do not present or discuss the degree 0 term of our $Q$ models.

Maps of the 3-D $Q$ model derived using three-component data, *QRLW8*, are presented in Figure 3.9. The lateral variations are expressed in terms of relative variations in $Q^{-1}$ with respect to *QL6c*. The blue and red colors correspond to high $Q$ (low attenuation) and low $Q$ (high attenuation), respectively. The surface positions of hot spots, according to *Richards et al.* [1988] are also shown as black dots in the maps at depths greater than 300 km.

For the depth range above 200 km, we find a good correlation between the distribution of $Q$ and tectonics. The lowest $Q$ anomalies are located under the East Pacific Rise, mid-Atlantic Ridge, Indian ridges, back-arc regions of the western Pacific, and in the Mediterranean. Such low $Q$ features under ridges and back arcs have also been documented in other regional $Q$ studies [*Ding & Grand*, 1993; *Flanagan & Wiens*, 1994]. We also note a low $Q$ zone centered in the southern Pacific extending north to Hawaii. This low $Q$ zone (which does not have an obvious correspondence in elastic velocity models at shallow depths) becomes stronger with depth, and is one of two most prominent low $Q$ anomalies at depths below 200 km.

At depths shallower than 200 km, high $Q$ anomalies are generally found in tectonically stable areas, such as the Canadian Shield, Australia, Siberia, Antarctica, the Russian Platform, Brazil and Africa.

This tectonic-related $Q$ distribution at shallow depths is consistent with other global $Q$ models obtained using various data and techniques [*Warren & Shearer*, 2002; *Reid et al.*, 2001; *Selby & Woodhouse*, 2000; *Selby & Woodhouse*, 2002; *Bhattacharyya et al.*, 1996]. In Figure 3.10, we compare the average $Q$ structure in the depth range 80-200 km with two other recent global $Q$ models: the $Q_\alpha$ model presented by *Warren & Shearer* [2002] (a 2-D model of the top 220 km of the mantle), and the degree 20 $Q_\mu$

model by *Selby & Woodhouse* [2000], which is constructed from Rayleigh waves. Here we show its $Q_\mu$ map at the period of 73 s. Even though they are derived from different approaches, the tectonic-related $Q$ distribution in the shallow mantle is present in all these models.

Between 200 km and 300 km, the tectonic-related $Q$ distribution in *QRLW8* is gradually replaced by a simpler pattern. The strongest low $Q$ anomalies are under central Pacific, south Atlantic and southern Africa. Some strong low $Q$ anomalies at shallow depths disappear, such as the most notable low $Q$ features below the East Pacific Rise, Atlantic Ridge, India Ridge and western Pacific back arcs. The observation of shallow roots of low $Q$ beneath mid-ocean ridges supports the passive character of the ridge system and is in agreement with velocity models, where the low velocity signature of oceanic ridges is also largely limited to the topmost mantle [*Zhang & Tanimoto*, 1993]. Similarly, some shield-related high $Q$ regions also taper off within this depth range, such as southern Africa, Antarctica and part of America.

At depths greater than 400 km, the $Q$ distribution is generally dominated by two strong minima, one under the southern Pacific and one under Africa, yielding a strong degree-2 pattern. We also find that a majority of hotspots are located above regions of low $Q$, which is consistent with *QR19*, in which a tectonic-correlated $Q$ distribution at shallow depths is gradually replaced by a hotspot-correlated pattern at larger depths. The degree-2 pattern of attenuation in the upper mantle transition zone was also found in previous studies [*Rould et al.*, 1990; *Romanowicz et al.*, 1987b; *Suda et al.*, 1991] using complex frequency measurements of fundamental spheroidal modes. In the degree-2 pattern of *QRLW8*, the two low $Q$ minima are, strikingly, positioned above the two 'superplumes' documented in the lowermost mantle from elastic tomography [*Li & Romanowicz*, 1996; *Masters et al.*, 1996; *Mégnin & Romanowicz*, 1999b; *Gu et al.*, 2001a], which, themselves have been shown to be well correlated with the degree 2 geoid as well as with the hotspot distribution [*Richards et al.*, 1988].

This correlation and its geodynamic implications will be discussed in the next chapter.

We will now discuss the stability of the $Q$ model.

### 3.5.3 Discussion of model stability

#### $Q$ models from different data sets

In Figure 3.11, we present the $Q$ models inverted separately from the transverse component ($QL$), radial component ($QRr$) and vertical component ($QRv$). The depth correlation between $QRr$ and $QRv$ is also shown. The $QL$ model is shown only at shallow depth (180 km), as Love waves have limited resolution at larger depths. Although the models differ in some details, similar $Q$ distributions are observed at shallow depth (180 km) in all models, with low attenuation under continents and high attenuation under ridges and back arcs. The low $Q$ region in the central Pacific is stronger and extends further north in the transverse component (Love wave) model. This may be an indication of anisotropy in $Q$, however, we do not feel we are able to resolve this confidently. The $QRr$ and $QRv$ models are also in good correspondence at greater depths, showing low $Q$ regions under Africa and the Pacific. The depth correlation between $QRr$ and $QRv$ is larger than 0.6 at all depths, in spite of their different data coverage. Indeed, fewer radial component traces are available due to the more noisy character of horizontal component data. While it is interesting to note the relatively good agreement between the different models, combining three-component data to obtain model *QRLW8* results in better depth resolution and more robust features.

#### Resolution Analysis

We implement resolution tests to further inspect the robustness of the pattern obtained in the upper mantle transition zone. Unlike the commonly used checkerboard model, we construct a test input model by setting two opposite degree 2 patterns

in the two splines corresponding to the shallow parts of the depth parameterization, which cover the uppermost mantle (80 km to $\sim$ 200 km), and in the 5th and the 6th splines, which cover the transition zone ($\sim$ 300 km to $\sim$ 600 km). The resolution matrix (e.g. *Aki & Richards* [2002]) is directly obtained from the combination of partial derivative matrix and model covariance matrix used in the inversion for real three-component data. The result is shown in Figure 3.12a. Compared to the uppermost mantle, the transition zone is apparently overdamped due to the weaker sensitivity in this depth range combined with unmodeled higher order elastic effects. Nevertheless, the pattern of lateral variations in $Q$ is well recovered and not affected by the opposite pattern in the uppermost mantle. This indicates that the strong degree 2 pattern in the transition zone cannot be an artifact resulting from the leakage of structure in the uppermost mantle. Same experiments are performed at higher degrees. Similarly, the amplitude is well recovered at shallow depths and decreases more at transition zone depths for higher degrees, but the pattern of lateral variations is recovered in both depth ranges. The result of a degree 6 resolution test (Figure 3.12b) shows that the same conclusions hold at shorter wavelengths

**Bootstrap test**

We apply the bootstrap method to estimate model uncertainties. First, all the data are divided into 12 groups according to their month of recording. Next, 10 groups are successively picked out of 12 to generate a data subset for each test. With all the combinations thus obtained, we construct a data population of 66 data subsets with each subset comprises about 83% of the complete dataset. The same inversion procedure and damping scheme as used for model *QRLW8* are applied to each subset. Finally, the standard deviation of the resulting 66 $Q$ models is used to estimate the uncertainty of the model. Ten samples of the resulting 'sub-models' at depths of 200 km and 500 km are shown in Figure 3.13. The tectonic-related features at 200 km and the strong degree 2 pattern at 500 km are clear on all the 'sub-models'. In Figure 3.14 we show the estimated uncertainties at 200 km and 500 km. The maximum

amplitude of uncertainty is less than 10%, and the uncertainties are less than 5% in most regions. Poor-coverage areas tend to have larger uncertainty, such as the north Pacific and the area between Antarctica and Australia. Also note that the uncertainty is very small in the central Pacific, where the prominent low $Q$ zone was found.

### Amplitude of lateral variations in $Q$

The results of the bootstrap tests are only valid inasmuch as the damping chosen for the inversion is valid. As mentioned previously on the occasion of synthetic tests, the variance in the waveforms is dominated by the phase alignment, therefore, it is mainly contributed by 3-D elastic structure. It is thus not surprising that the variance reduction obtained with *QRLW8* is only on the order of 7%. On the other hand, the maximum amplitude of the lateral variations in $Q$ varies with the damping chosen in the inversion. Because the $Q$ signal is faint and we do not correct for focusing explicitly, strong damping is necessary to obtain a stable model. We feel that these amplitudes are therefore not well constrained. We conservatively chose a damping scheme that results in amplitudes of about 55% at 200 km, but these could be larger by a factor of 2. The corresponding lateral variations in temperature are on the order of $200 - 400^oC$, depending on the model chosen for frequency dependence in $Q$ [*Karato*, 1998].

### Assessing the focusing effects

Although previous studies [*Romanowicz*, 1994b; *Selby & Woodhouse*, 2000; *Selby & Woodhouse*, 2002] have shown that the focusing/defocusing contamination is not significant in the retrieved long wavelength $Q$ structure, it is important to examine the focusing/defocusing effects with the data set and 3-D elastic model used in this study.

To investigate this, we generate synthetic data by applying higher order asymptotic

theory [*Romanowicz*, 1987a; *Romanowicz, Gung & Capdeville*, 2003]. In which the normal mode amplitudes, to order $1/l$, can be expressed as

$$A_K \;=\; A_K^0\,(1+\delta F_K), \tag{3.8}$$

where $A_K^0$ is the zeroth order amplitude, as used in path average approximation, $\delta F_K$ is the amplitude perturbation term, which depends on the relative strength of great circle and minor arc averages of the local frequency and its transverse first and second derivatives.

Similar to our earlier inversion experiment, the radial component of Rayleigh waves with realistic data coverage are considered. The phase and amplitude perturbations of synthetics are computed based on the degree 16 $SV$ model, *SAW16BV*. No 3-D $Q$ model is used in the generation of synthetics: we assume no lateral heterogeneity in $Q$.

We then invert for a 3-D attenuation model with the synthetic data, using the same approach as for real data, i.e. correcting for the phase shift and ignoring the elastic amplitude perturbation term. Same damping scheme as in real data is applied during the inversion. The resulting 'ghost $Q$' model and its depth correlation to $Q$ model derived from realistic radial component Rayleigh wave data, *QRr*, are shown in Figure 3.15.

The low amplitude ($< 10\%$) of 'ghost $Q$' model shows that the contamination from uncorrected focusing/defocusing effects is small, in agreement with the previous studies [*Romanowicz*, 1994b; *Selby & Woodhouse*, 2000; *Selby & Woodhouse*, 2002]. In particular, its poor correlation (within the range of $\pm$ 0.2 at all depths) to *QRr* demonstrates that our $Q$ model is not strongly biased by the uncorrected focusing/defocusing effects.

This can be understood when one considers that elastic focusing effects, to first order,

add algebraically along the path (direction of propagation counts), whereas $Q$ effects do not depend on the direction of propagation. When inverting for Q, some of the focusing effects end up in the null matrix. The drawback is that strong damping is necessary, increasing uncertainty on the amplitudes of lateral variation of $Q$.

**Source parameters**

In this study, we assume that source parameters are as given in the CMT catalog. Uncertainties in the source parameters could directly affect the inverted $Q$ images. Since our waveform approach does not exclude the effects of source uncertainties, an implicit assumption is that the uncertainties in sources are randomly distributed, and the steady signals of $Q$ structure on the waveforms are not significantly distorted by the random 'noises' of source uncertainties, given a large amount of data.

To assess the effects of source uncertainties on $Q$ tomography, we have performed an experiment, in which we randomly perturb the source parameters of the events in our dataset, starting from the CMT solutions. Four ranges of perturbation amplitudes are applied, -5% to 5%, -10% to 10%, -20% to 20% and -40% to 40%, respectively. The depth correlation between the resulting $Q$ models and *QRLW8* are shown in Figure 3.16. The resulting $Q$ images are stable and the correlation to *QRLW8* is larger than 0.9 at all depths for $Q$ models with perturbation amplitudes less than 20%. The correlation is larger than 0.7 at all depths even when the perturbation amplitude is as large as 40%. The results of this test show that, with the data coverage used in this study, realistic errors in the source parameters do not have a significant effect on the resulting $Q$ model.

## 3.6 Conclusions

We have presented a 3-D $Q$ model of the upper mantle, which has been derived using waveform data of three-component surface waves. The results of this study may be summarized as follow.

(1) $Q$ tomography waveform-based inversion is feasible, if appropriate phase corrections based on a 3-D elastic models and careful data selection are applied prior to $Q$ inversion.

(2) Our 3-component derived $Q$ model, *QRLW8*, can be divided into two depth ranges. The $Q$ distribution above 250 km is generally tectonic-related, which is similar to what is observed in elastic velocity models, with regions of high/low velocity correlated to regions of high/low $Q$. A notable exception is an elongated zone of low $Q$ in the central Pacific, extending from the south of the equator to Hawaii. Below 250 km, the tectonic-related pattern is gradually replaced by a pattern well correlated with the $V_S$ velocity distribution in the lowermost mantle, with two strong low $Q$ minima centered in the southern Pacific and under Africa. Most surface hot spot positions are above the low $Q$ areas in the upper mantle transition zone. Please refer to Chapter 4 for detailed discussion.

The lateral resolution in our current $Q$ model is limited due to the unmodeled high order elastic effects and the uncertainties in the sources parameters. The next step is to extend this waveform modeling approach to include focusing effects and source readjustment based on improved 3-D velocity models.

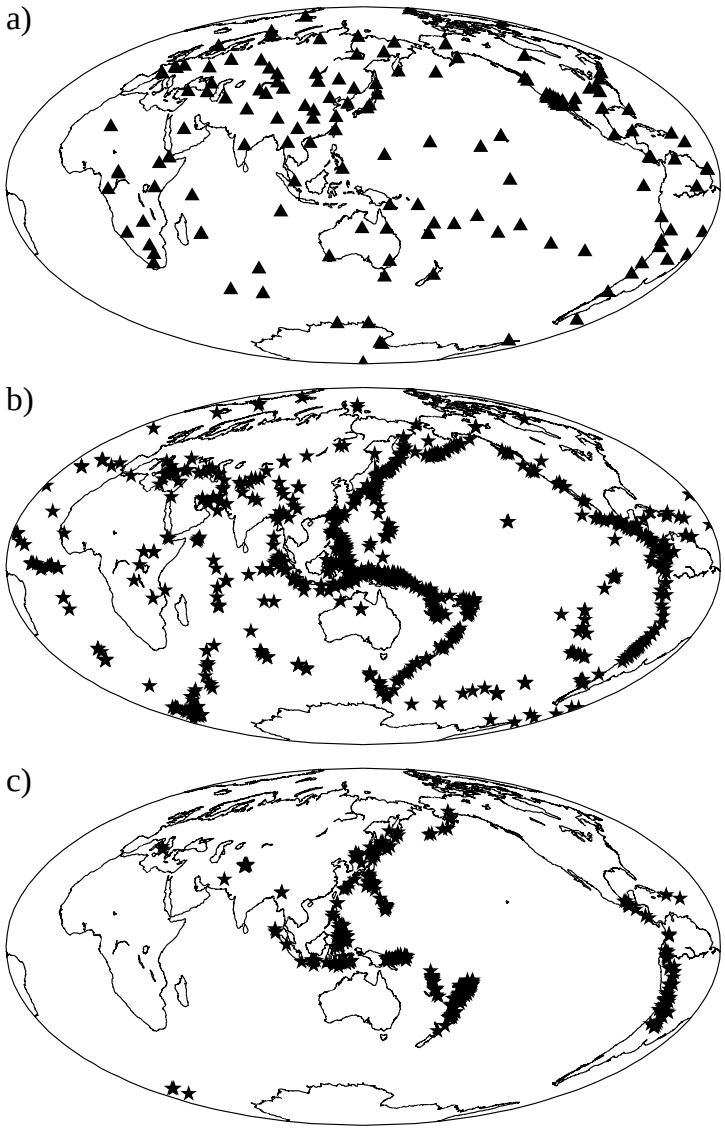


Figure 3.1: Distribution of stations and epicenters for this study. (a) Stations ; (b) Shallow events (depth $< 100$ km); (c) Deep events (depth $> 100$ km)

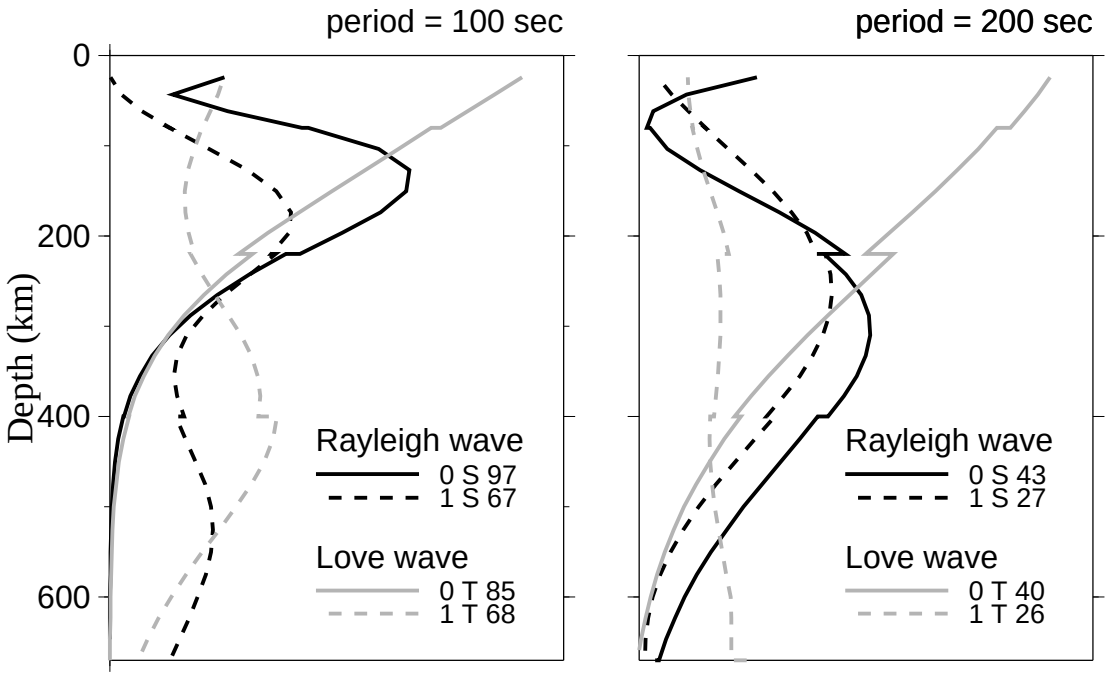


Figure 3.2: Radial sensitivity kernels for $S$ velocity for fundamental mode (solid line) and first overtone (dotted line) Love and Rayleigh wave at periods of 100 s and 200 s.

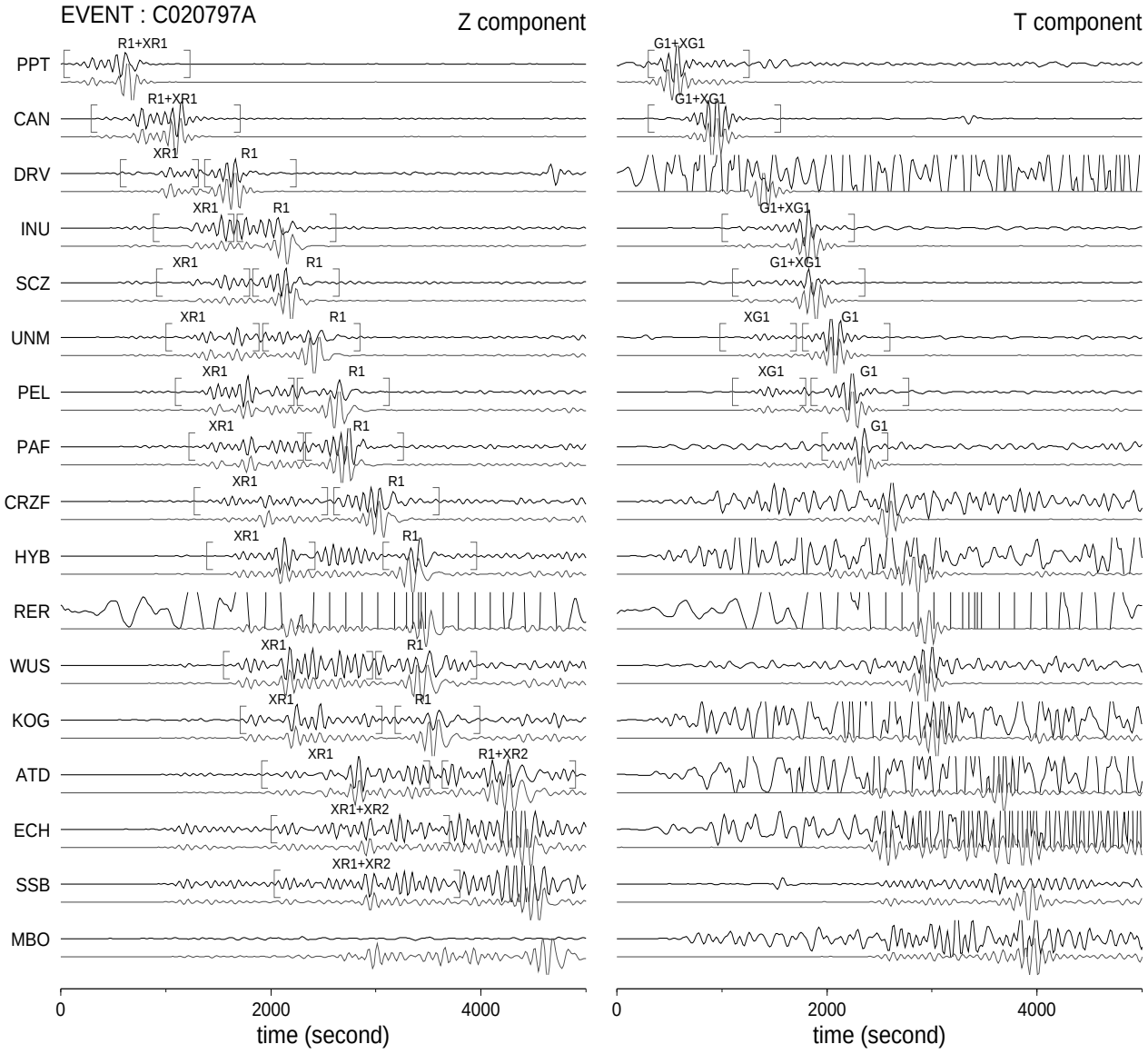


Figure 3.3: Low-pass filtered ($f < 1/60Hz$) vertical and transverse component surface wave seismograms for the Feb. 7, 1997 Tonga Islands earthquake recorded at Geoscope stations. The observed seismograms (black) are plotted superimposed on the reference PREM synthetic seismograms with ellipticity included (gray). Only data within the indicated time windows are used in the inversions. The noisy seismograms without time windows have been rejected by the automatic picking algorithm. Note that the horizontal component traces are much noisier than vertical component traces. As a result, fewer wavepackets in horizontal component are selected.

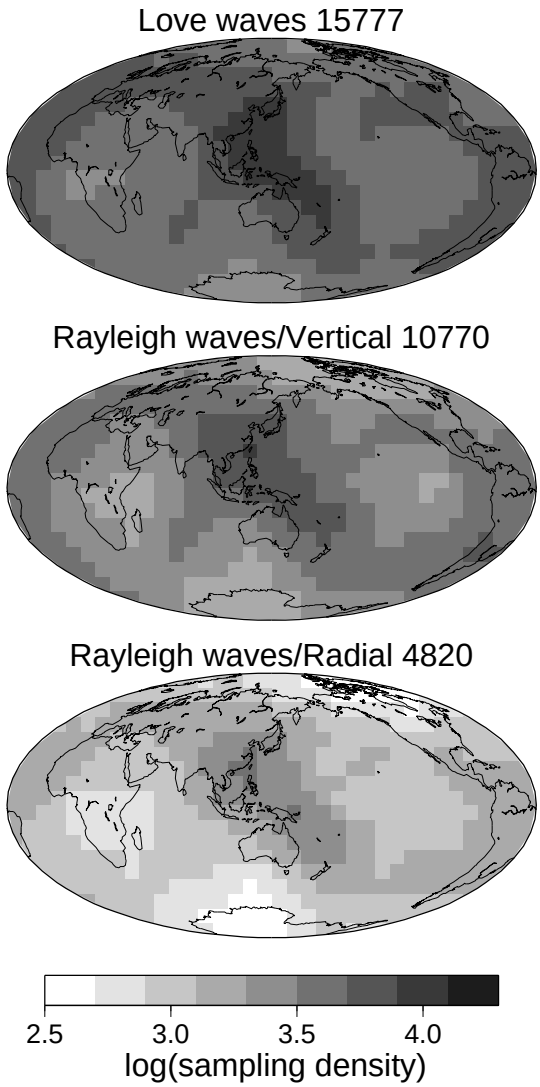


Figure 3.4: Path density coverage achieved in this study, expressed as the logarithm of the ray length (in degrees) in each $10^o$ by $10^o$ cell, corrected for latitude. The total number of wavepackets collected for each component is also shown.

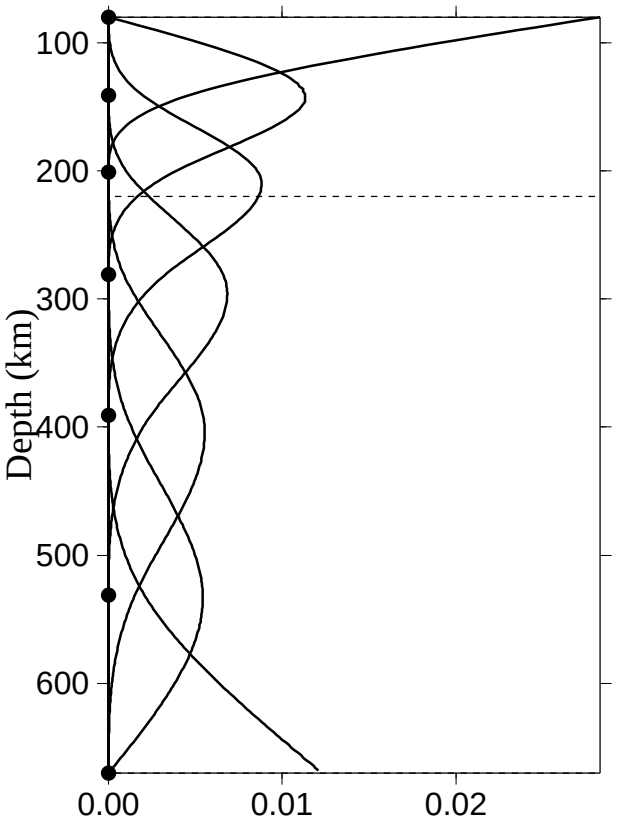


Figure 3.5: The cubic b-splines used as basis functions, for the radial parameterization used in the $Q$ inversion.

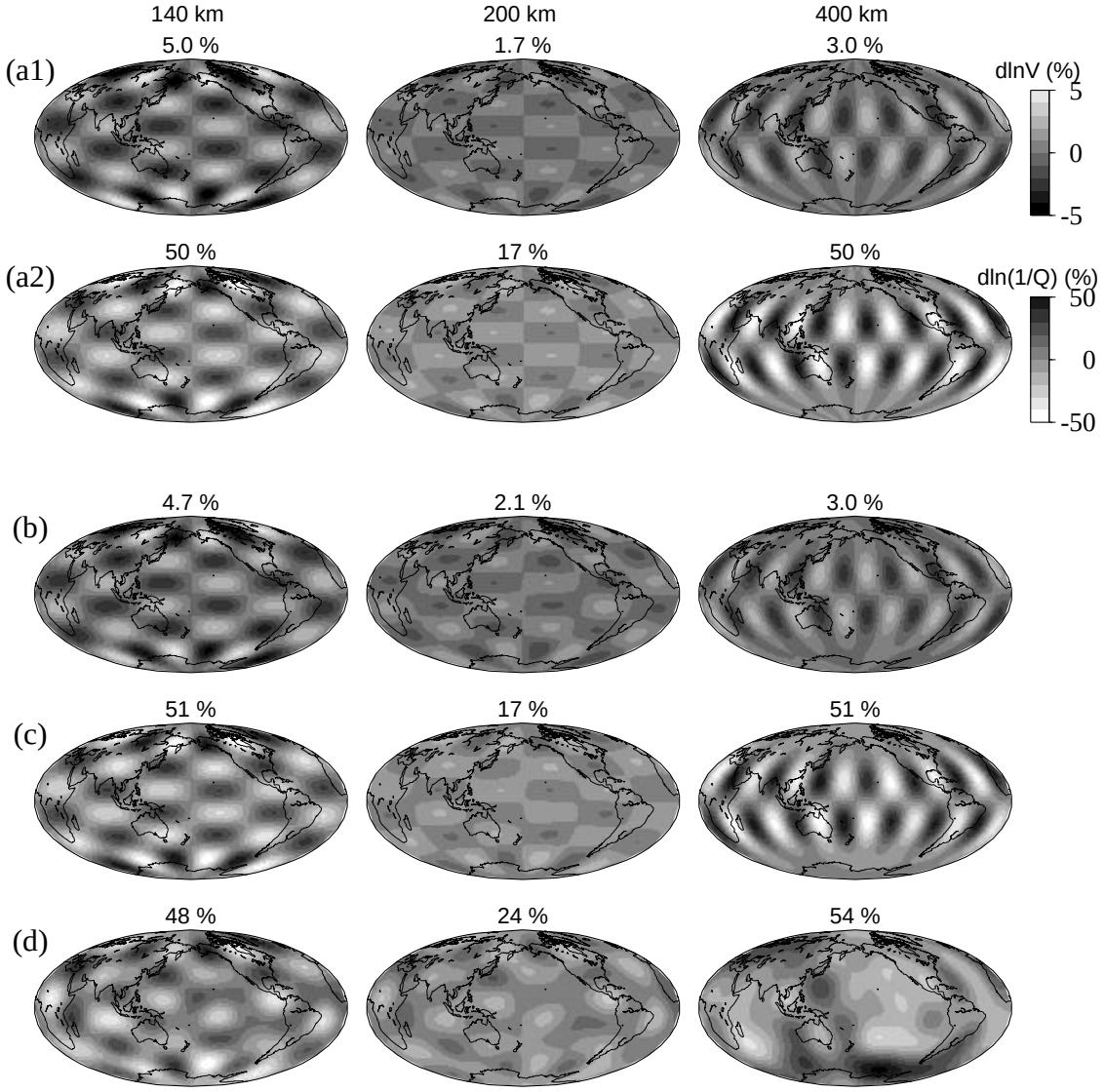


Figure 3.6: Input models and results of synthetic inversions: (a1) Input $V_S$ model; (a2) Input $Q$ model; (b) Inverted velocity model without accounting for the 3-D $Q$ effects; (c) Inverted $Q$ model with phase correction based on the velocity model shown in (b). (d) Inverted $Q$ model without 3-D elastic corrections.

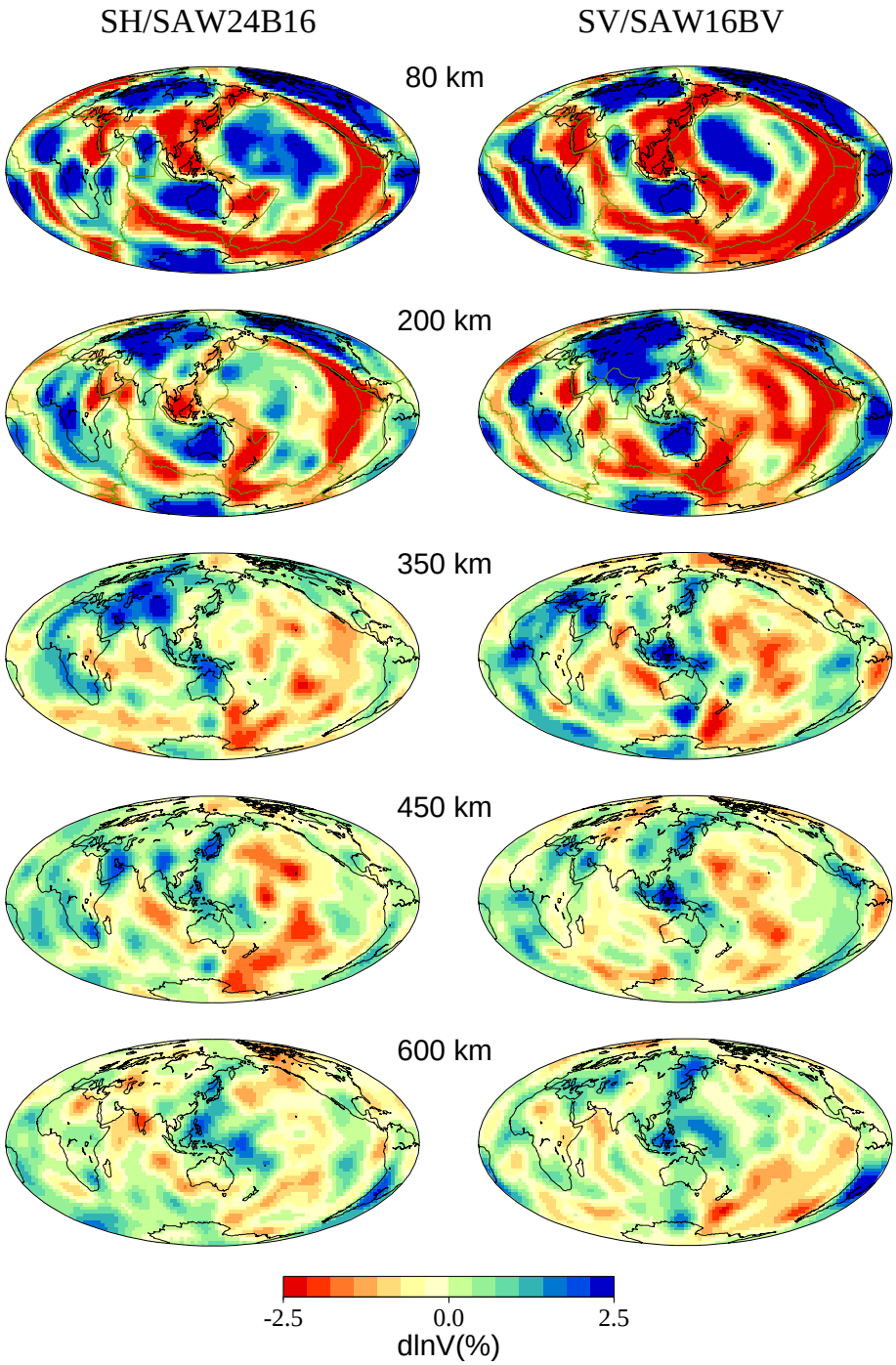


Figure 3.7: Comparison of $V_{SH}$ (*SAW24B16*) and $V_{SV}$ (*SAW16BV*) models. The degree 24 *SAW24B16* model is truncated to degree 16.

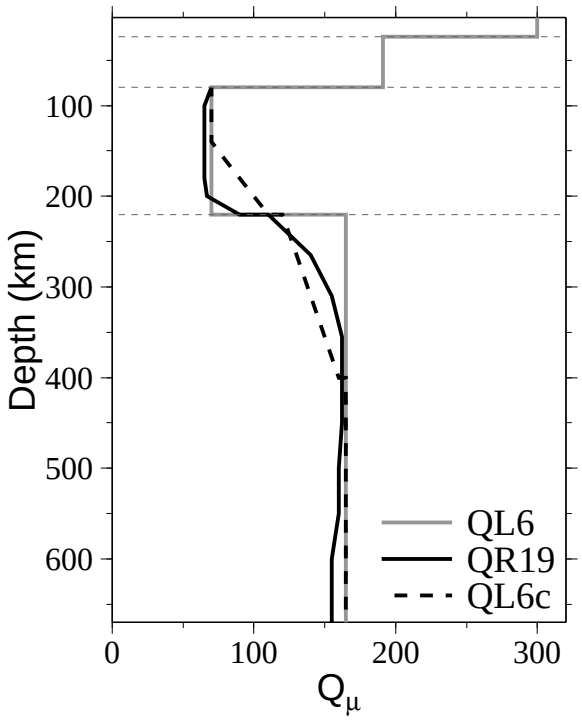


Figure 3.8: Three starting 1-D $Q$ models used in the $Q$ inversion, *QL6* [*Durek & Ekström*, 1996], *QL6c* and degree 0 terms of *QR19* [*Romanowicz*, 1995]. *QL6c* is modified from *QL6* by smoothing across the 220 km discontinuity.

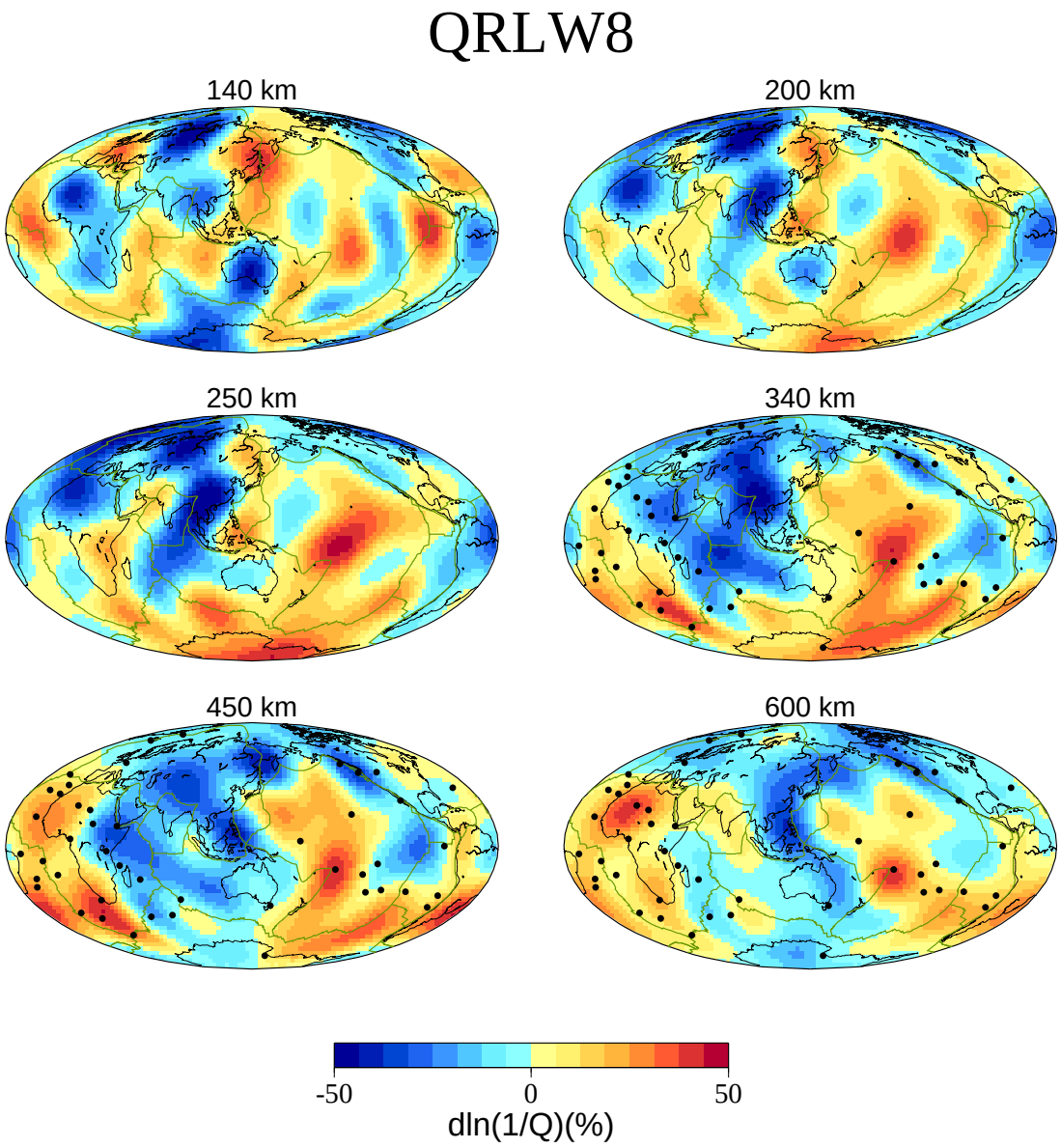


Figure 3.9: Model *QRLW8* derived from three-component data. Black dots are hotspots according to *Richards et al.* [1988].

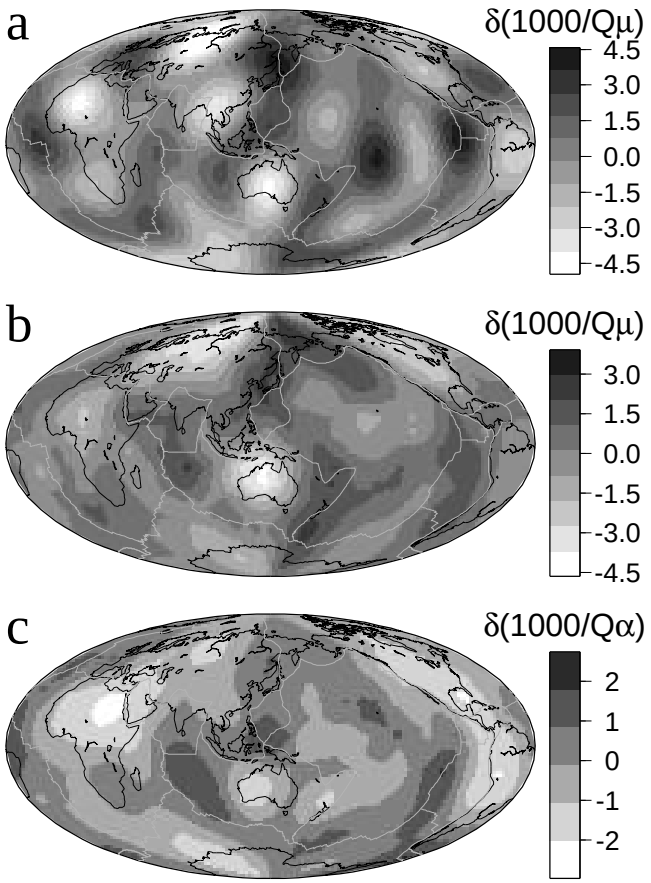


Figure 3.10: Comparison of $Q$ models. (a) Average $Q$ map for the depth range 80-200 km of *QRLW8*, (b) $Q_\mu$ model for 73 s Rayleigh waves by *Selby & Woodhouse* [2000] and (c) $Q_\alpha$ model by *Warren & Shearer* [2000].

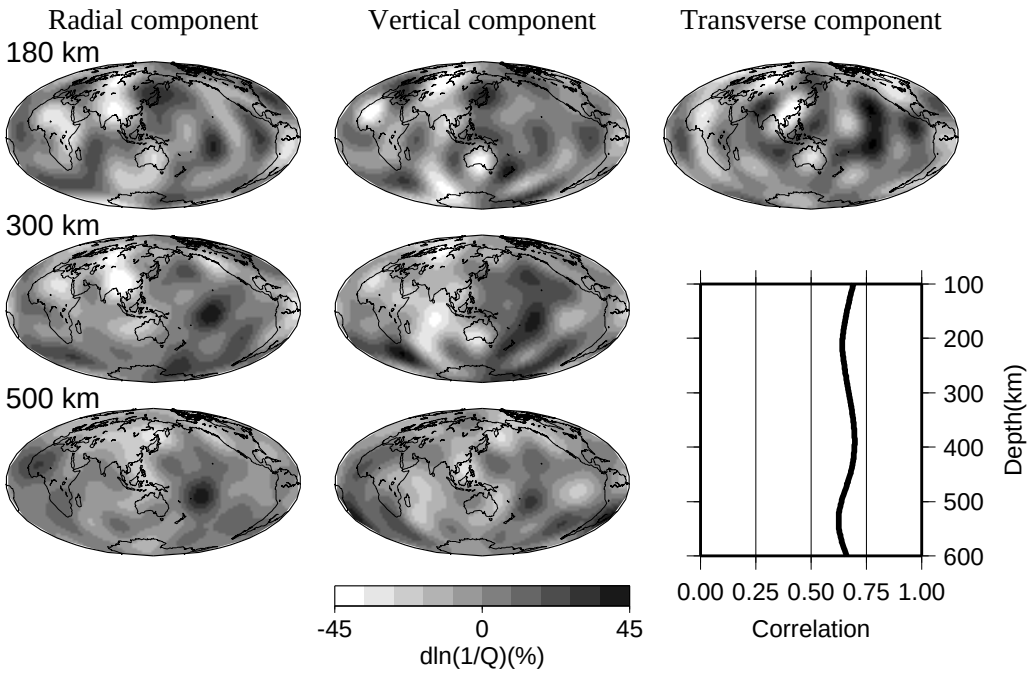


Figure 3.11: Comparison of $Q$ models derived from different component data (left: radial; middle: vertical; right: transverse). The right panel shows the depth correlation of $Q$ models derived from radial and vertical components.

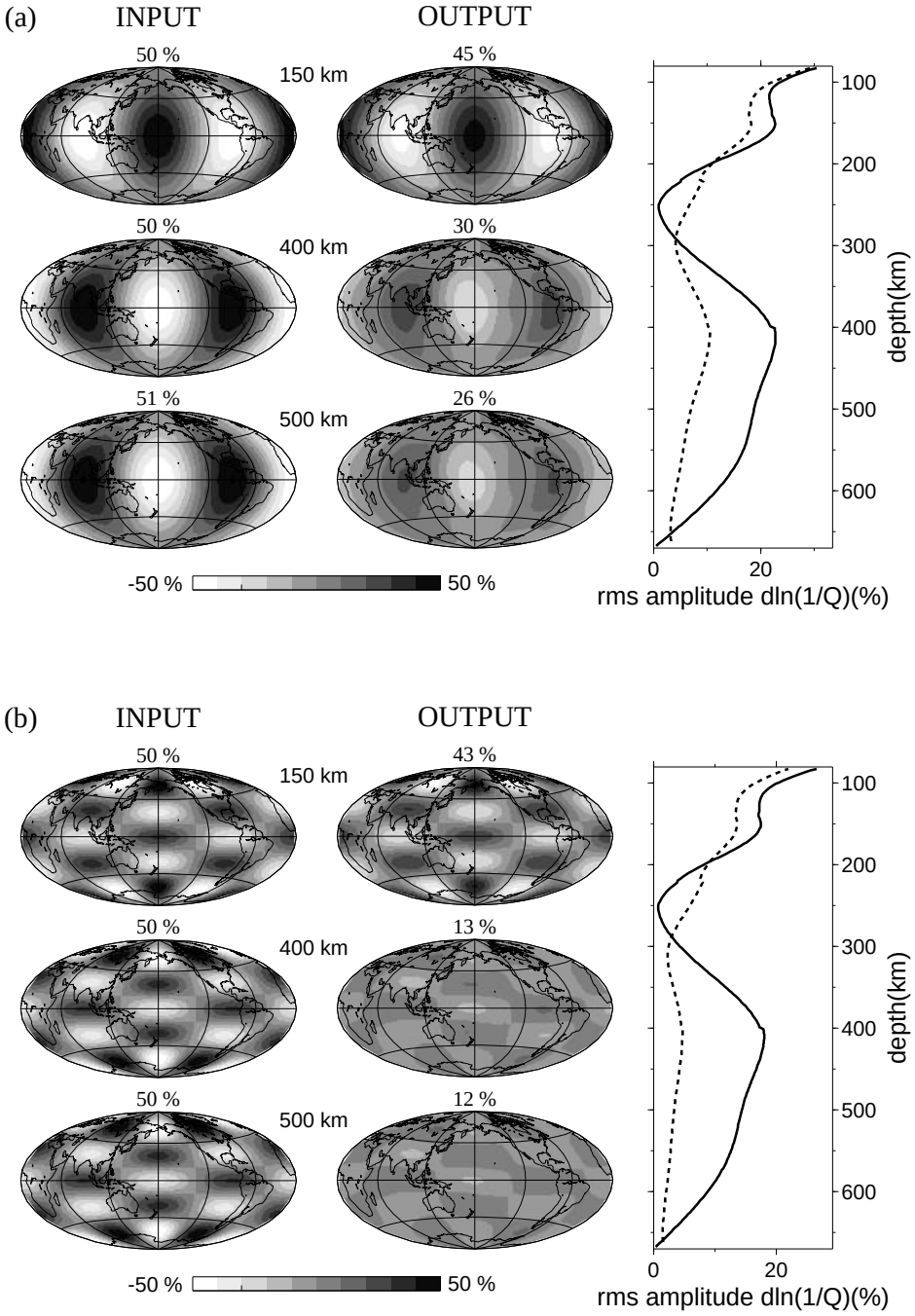


Figure 3.12: Results of resolution tests. (a) Degree 2 input model (left column) and output model (middle column). The rms amplitude profiles are shown in the right panel, with solid line for input model and dotted line for output model. (b) Same as (a), but for a degree 6 input model.

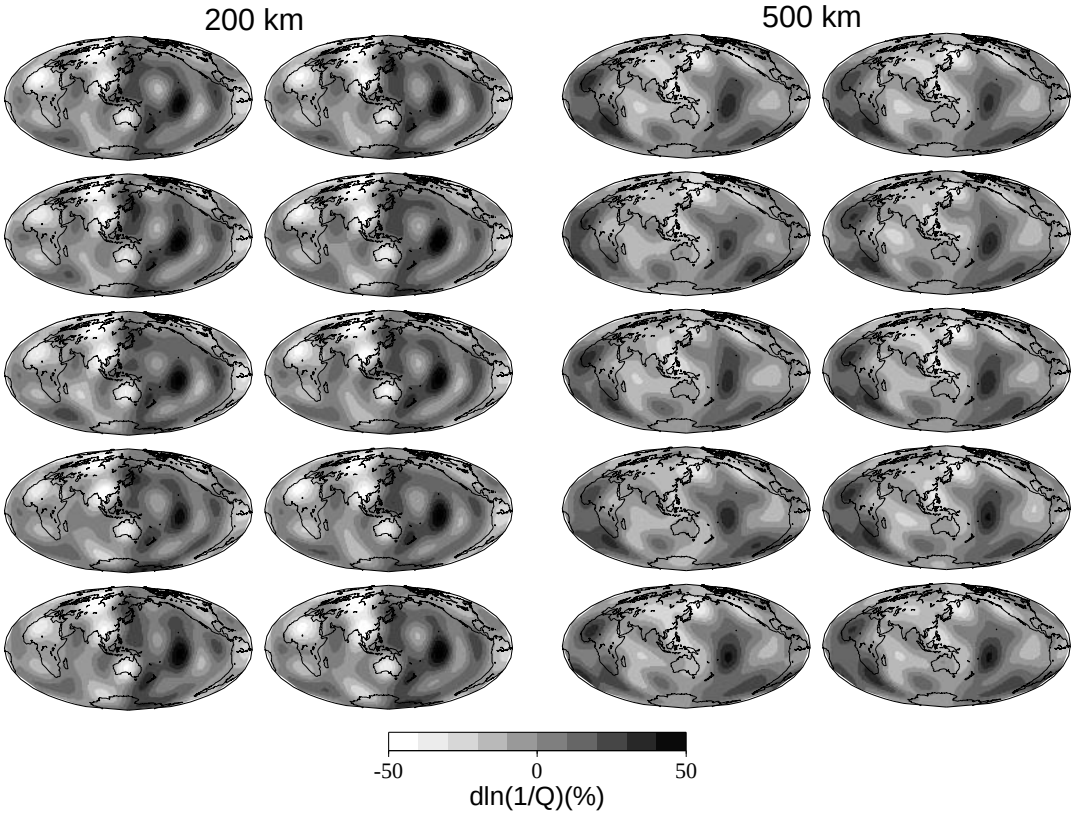


Figure 3.13: Examples of $Q$ models obtained from the bootstrap test. Note the stable tectonic-related $Q$ distribution at 200 km and the plume-correlated pattern at 500 km.

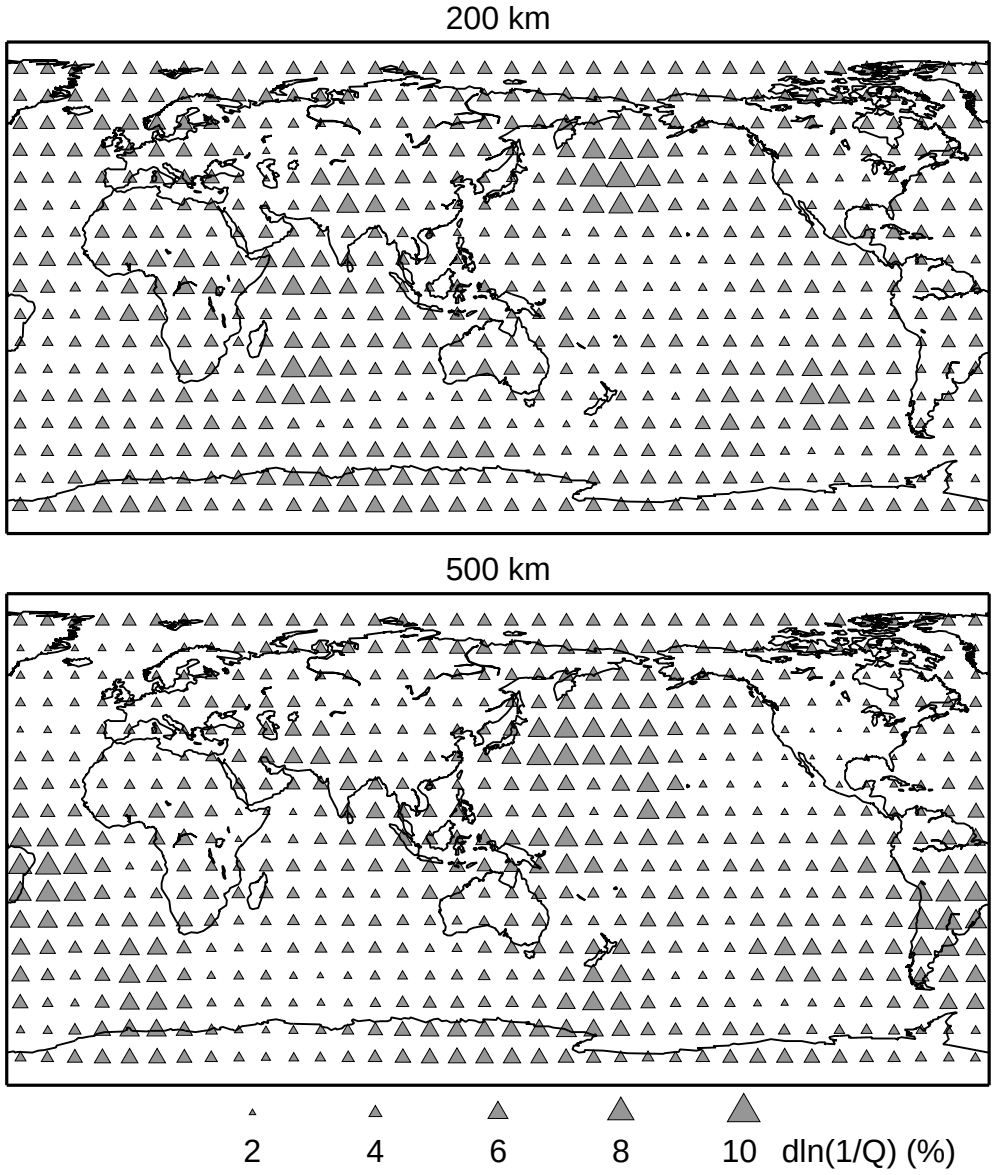


Figure 3.14: The error estimates at depths of 200 km and 500 km from the bootstrap test.

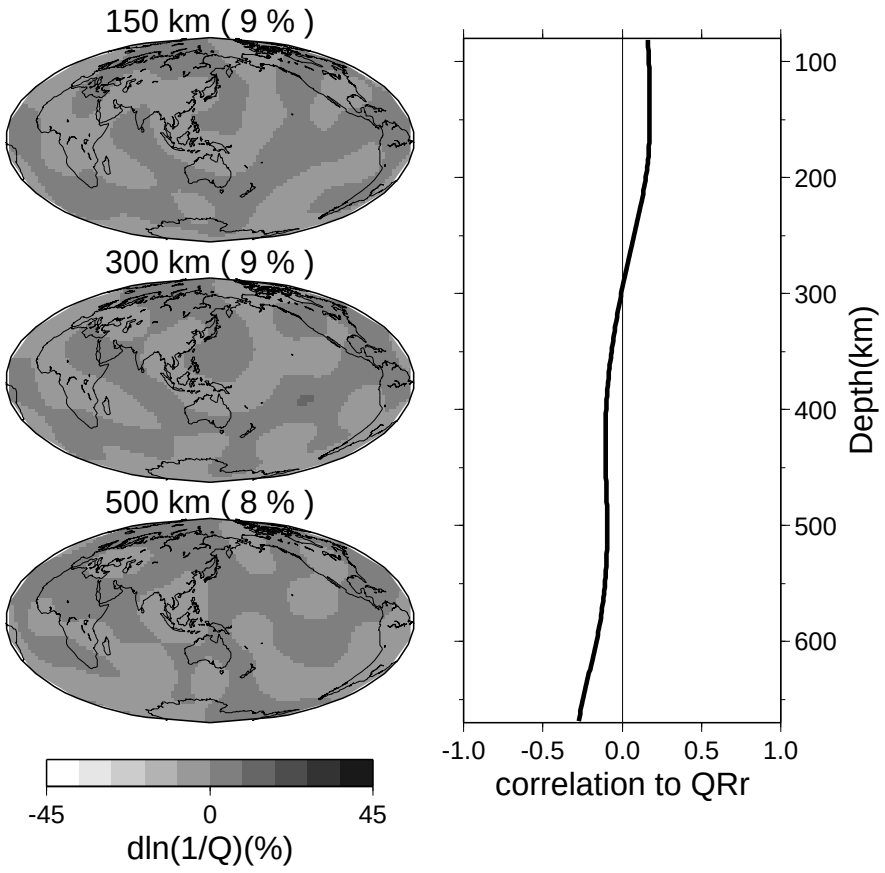


Figure 3.15: Results of the synthetic experiment on focusing/defocusing effects. Left: 'ghost $Q$' model projected from uncorrected focusing/defocusing effects in 3-D elastic model, *SAW16BV*. Right: the depth correlation between 'ghost $Q$' model and *QRr* (please see text for the details).

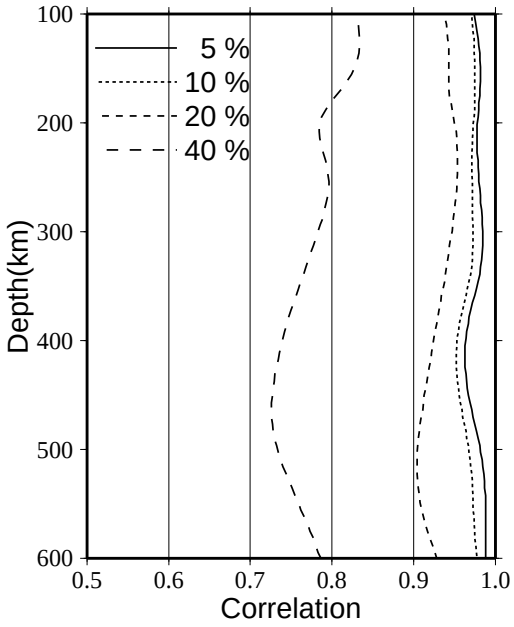


Figure 3.16: Correlation as a function of depth of *QRLW8* and $Q$ models obtained with perturbations to source parameters of different amplitudes. Details are given in the text.

# Chapter 4

# Superplumes from the Core-Mantle Boundary to the Lithosphere: Implications for Heat Flux

This chapter has been published in *Science* [*Romanowicz & Gung*, 2002] under the title: 'Superplumes from the core-mantle boundary to the lithosphere: implications for heat flux.'

## Summary

Three-dimensional modeling of upper-mantle anelastic structure reveals that upwellings associated with the two large 'superplumes', imaged by seismic elastic tomography at the base of the mantle, persist through the upper-mantle transition zone, and are deflected horizontally beneath the lithosphere. This explains the unique transverse isotropy in the central Pacific. We infer that the two superplumes may play a major and stable role in supplying heat and horizontal flow to the low viscosity

asthenospheric channel, lubricating plate motions and feeding hotspots. We suggest that more heat may be carried through the core-mantle boundary than is accounted for by hot-spot fluxes alone.

## 4.1 Introduction

Global seismic tomography aims at improving our understanding of mantle dynamics by providing constraints on three-dimensional (3-D) temperature and composition, using elastic velocities as proxies. Much progress has been made in recent years in resolving increasingly finer details in the 3-D distribution of elastic velocities from the inversion of seismic phase and travel time data [*Masters et al.*, 1996; *Gu et al.*, 2001a; *Mégnin & Romanowicz*, 1999b]. In particular, regions of faster than average velocity, associated with subduction around the Pacific rim, have revealed a variety of behaviors of lithospheric slabs in the transition zone, some stagnant around the 670 km discontinuity, while others penetrate into the lower mantle to depths in excess of 1500 km [*Fukao et al*, 2001]. These results agree with geodynamic models in which the cold and dense downgoing slabs play a driving role in global mantle circulation heated primarily from within [*Bercovici et al.*, 2000]. On the other hand, the detailed morphology and role of upwellings, as manifested by two prominent zones of lower than average velocity in the lowermost mantle, commonly referred to as superplumes, is less clear. Their location, under the south-central Pacific and under Africa, correlates with the global distribution of hotspots, as well as two major geoid highs [*Hager et al.*, 1985]. Recent tomographic S wave velocity models suggest that the superplumes rise high above the core-mantle boundary (CMB) [*Mégnin & Romanowicz*, 1999b; *Ritsema et al.*, 1999], and joint seismic/geodynamic studies imply that they may be active upwellings [*Forte & Mitrovica*, 2001]. However, finer scale resolution is still lacking. In particular, velocity tomography in the transition zone correlates well

with slabs, but not so well with hotspot distribution or the residual geoid, except at degree 6 [*Richards et al.*, 1988]. This could be due to a combination of factors: (1) elastic velocities are sensitive to composition as well as temperature; (2) the effect of temperature on velocities decreases with increasing pressure [*Karato*, 1993]; (3) wavefront healing effects make it difficult to accurately image low velocity bodies [*Nolet & Dahlen*, 2000]; and (4), hotspots could have a shallow origin, independent of the lower mantle superplumes [*Anderson*, 1990].

To obtain additional constraints on hotter than average features, we turn to the amplitudes of seismic waves, which are sensitive to 3-D anelastic structure. Owing to the exponential dependence of attenuation on temperature [Minster & Anderson, 1981], which we shall express in terms of $Q^{-1}$, where $Q$ is the quality factor, we expect anelastic tomography to highlight hotter than average regions better than standard elastic tomographic approaches.

There have been few attempts to map mantle 3-D attenuation structure. Unlike travel time and phase observations, which, in general, can be interpreted in the framework of linear ray theory, amplitudes are affected not only by anelastic structure, but also by the non-linear effects of wave propagation through the 3-D elastic medium, which causes focusing and scattering of energy (for example, high-frequency body waves traveling through slabs arrive early but are defocused). Because the lateral gradients of elastic structure are not sufficiently well constrained to allow the accurate removal of elastic effects, the resulting contamination of amplitude data can be severe. Particular care must therefore be taken in data selection and methodology in order to extract the intrinsic attenuation signal. Previous studies of lateral variations of $Q^{-1}$ in the upper mantle have noted high attenuation regions associated with ridges [*Romanowicz*, 1995; *Reid et al.*, 2001] and back arcs [*Romanowicz*, 1995; *Roth et al.*, 1990], and suggested the existence of a degree 2 pattern in attenuation [*Romanowicz*, 1995; *Suda et al.*, 1991]. However, on the global scale, 3-D mantle $Q^{-1}$ models have remained largely qualitative.

## 4.2 Results and discussions

We have developed a waveform tomographic inversion method, originally aimed at constructing global 3-D elastic models of the whole mantle [*Mégnin & Romanowicz*, 1999b; *Li & Romanowicz*, 1996], which now has been extended to iteratively solve for elastic and anelastic structure in the upper mantle, using three-component waveform data of fundamental and higher mode surface waves (see Section 3.4). While we do not directly account for elastic effects in the amplitudes, which limits the lateral resolution of our $Q^{-1}$ models to $smax = 8$ [*Selby & Woodhouse*, 2000], where $smax$ is the maximum degree in a horizontal spherical harmonics parameterization, strict data selection criteria are designed to reject data most strongly contaminated by focusing [*Gung & Romanowicz*, 2003].

In the top 250 km of the mantle, correlation of high Q regions with shields is seen systematically in North and South America, Eurasia, Australia and Antarctica, whereas mid-ocean ridges in the Pacific, Atlantic and Indian Ocean exhibit generally low Q values, as do western Pacific back-arc regions (Figure 4.1). This is similar to what is observed in elastic velocity models [*Masters et al.*, 1996; *Gu et al.*, 2001a; *Mégnin & Romanowicz*, 1999b], with regions of high/low velocity correlated with regions of high/low Q. A notable exception is an elongated zone of high attenuation in the central Pacific, extending from south of the equator to Hawaii, not seen in *SH* velocity models [*Mégnin & Romanowicz*, 1999b; *Li & Romanowicz*, 1996] at these depths. Below 250 km, this tectonics-related Q distribution is gradually replaced by a simpler pattern, with two strong attenuation maxima centered in the southern Pacific and under Africa, throughout the upper mantle transition-zone. At depths greater than 400 km, a majority of hotspots are located above regions of high attenuation.

In model *QRLW8*, the high attenuation regions in the transition zone coincide in location with the minima in elastic velocity associated with the two superplumes in the lowermost mantle. Correlation between $Q$ in the transition zone and velocity in the last 500 km of the mantle is particularly strong at degree 2 (Figure 4.2), but persists

at shorter wavelengths. Cross-sections in the Pacific (Figure 4.3a) and under Africa (Figure 4.3b) comparing upper mantle $Q^{-1}$ with lower mantle velocity distributions, emphasize the vertical correspondence of the transition zone low $Q$ zones with the lowermost mantle. The latter 'rise' vertically through the lower mantle and have complex shapes, especially under Africa. Because our $Q^{-1}$ model does not extend to the lower mantle, and the low velocity zones are only expressed faintly in the upper half of the lower mantle, where they appear to be narrower and have a complex shape just below the 670 km discontinuity, it is not possible to determine whether the superplumes are simply continuous across this major discontinuity, or whether they induce upwellings in the upper mantle through a thermal coupling processes. However, our results show that the superplumes must carry enough energy across the lower mantle to create coherent upwelling flow in the upper mantle transition zone, in agreement with some recent mantle flow models [*Forte & Mitrovica*, 2001]. In contrast, ridges are shallow high attenuation features, mostly confined to the upper 200 km of the mantle.

The low $Q$ zones in the transition zone connect with shallower ones whose positions are shifted horizontally, suggesting that the upwelling plume-related flow is deflected horizontally below the cold lithosphere, towards the Indian and Atlantic mid-ocean ridges under Africa, and in the Pacific, towards the East Pacific rise and the center of the Pacific plate. In the latter case, the flow is impeded on the west side by the presence of the Fiji-Tonga subduction zone. This deflection occurs at greater depths under the thicker continental lithosphere ($\sim$ 350 km, Figure 4.3b) than under the oceanic one ($\sim$ 200 km, Figure 4.3a).

This change in direction of the upwelling flow is supported by the presence of significant anisotropy (transverse isotropy), as seen by comparing $V_{SH} - V_{SV}$ cross-sections with those of $Q^{-1}$ (Figure 4.3a and Figure 4.3b). The existence of horizontal flow related to the spreading of upwelling flow beneath the lithosphere provides a simple explanation for the existence of strong transverse isotropy in the central Pacific, in particular under Hawaii, with $SH$ velocity greater than $SV$ velocity [*Ekström &*

*Dziewonski*, 1998]. Also, azimuthal anisotropy (not shown), which shows fast directions aligned perpendicular to the ridge in the vicinity of the East Pacific Rise, displays a more complex pattern in the central Pacific [*Montagner & Tanimoto*, 1991]. This is consistent with the spreading of upwelling flow associated with the superplumes into the asthenospheric low viscosity channel [*Gaboret et al.*, 2003], which perturbs the ridge-perpendicular lithospheric drag flow, and creates a complex horizontal flow pattern in the central Pacific. The 'hot' anomaly associated with the Hawaiian hotspot, as seen in the $Q^{-1}$ models (Figure 4.3a), is primarily expressed at shallow depths (less than 300 km), and appears to be 'fed' from the more southerly upwelling by horizontal flow beneath the lithosphere.

These results suggest a potentially important role for superplumes in the dynamics of the mantle: significant action may well take place in the shallow mantle, where hot material injected by the superplumes lowers the viscosity of the asthenosphere [*Forte & Mitrovica*, 2001; *Davies & Richards*, 1992; *Mitrovica & Forte*, 1997], lubricating the motion of the lithospheric plates. In particular, this would allow for efficient slab pull in the Pacific, and contribute to heating of the continental lithosphere under Africa [*Hager et al.*, 1985; *Nyblade & Robinson*, 1994]. Most hotspots are derived from the two main upwellings. Exceptions appear to be hotspots in north America and perhaps Iceland, whose signature in the $Q^{-1}$ models is lost below 400 km, and whose deep or shallow origin has been the subject of vigorous debate [*Ritsema et al.*, 1999; *Wolfe et al.*,, 1997; *Foulger et al.*, 2001]. Since material from the mega-upwellings progressively mixes with the asthenosphere, the relation of the position of different hotspots with respect to the centers of the major upwellings may provide clues on their distinctive geochemical signatures [*Hart et al.*, 1992], particularly in view of the noted correlation of the lower mantle superplumes with the Dupal anomaly [*Castillo*, 1988].

Previous suggestions on the relation of major flood basalts to the two superplumes [*Burke*, 1996] and the stability of absolute hot spot locations [*Morgan*, 1971], combined with the results of the present study, indicate that the two major lower mantle

upwellings may not be mere instabilities in the present mantle convective system. In particular, the estimate of $\sim 10\%$ heat from the core carried by plumes [*Sleep*, 1990] may need to be revised to account not only for hotspot flux, but also for heat carried horizontally in the asthenosphere and eventually contributed to the ridge system.

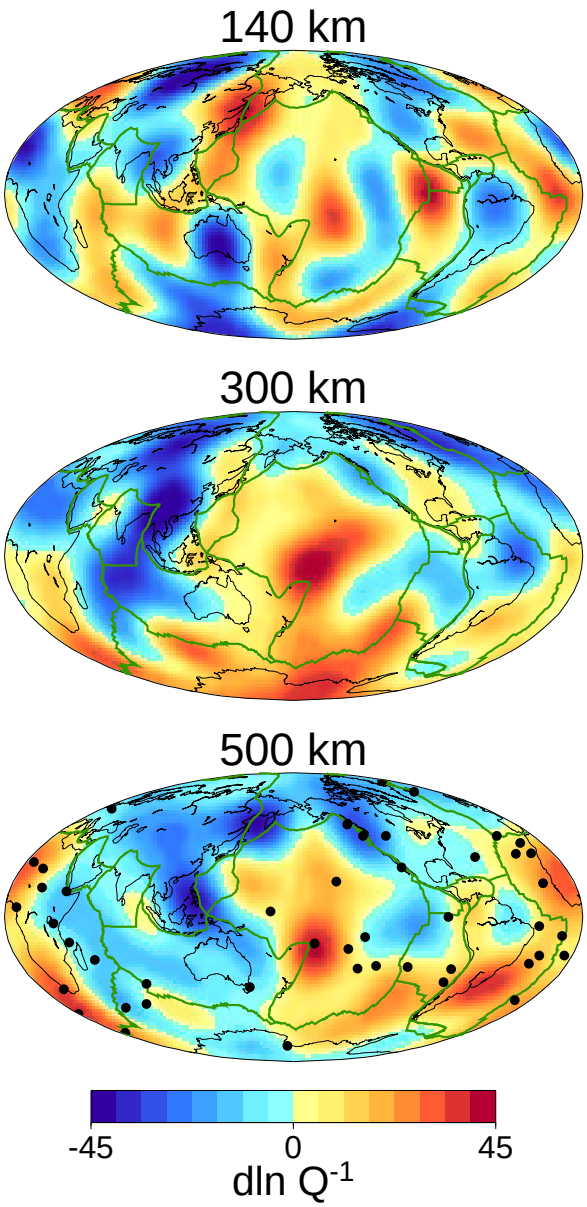


Figure 4.1: Maps of lateral variations in $Q^{-1}$ at representative depths in the upper mantle, obtained by joint inversion of three-component waveform data [model *QRLW8*]. Black dots are hotspots [*Richards et al.*, 1988] and the global plate boundary system is in green, emphasizing the change of $Q^{-1}$ pattern as depth increases. Note that the two high attenuation peaks in the transition zone appear to be connected through South America, following the trail of southern hotspots. Temperature contrasts at the center of the high attenuation regions in the transition zone could be several hundred degrees. However, amplitudes of lateral variations in $Q^{-1}$ are not well constrained.

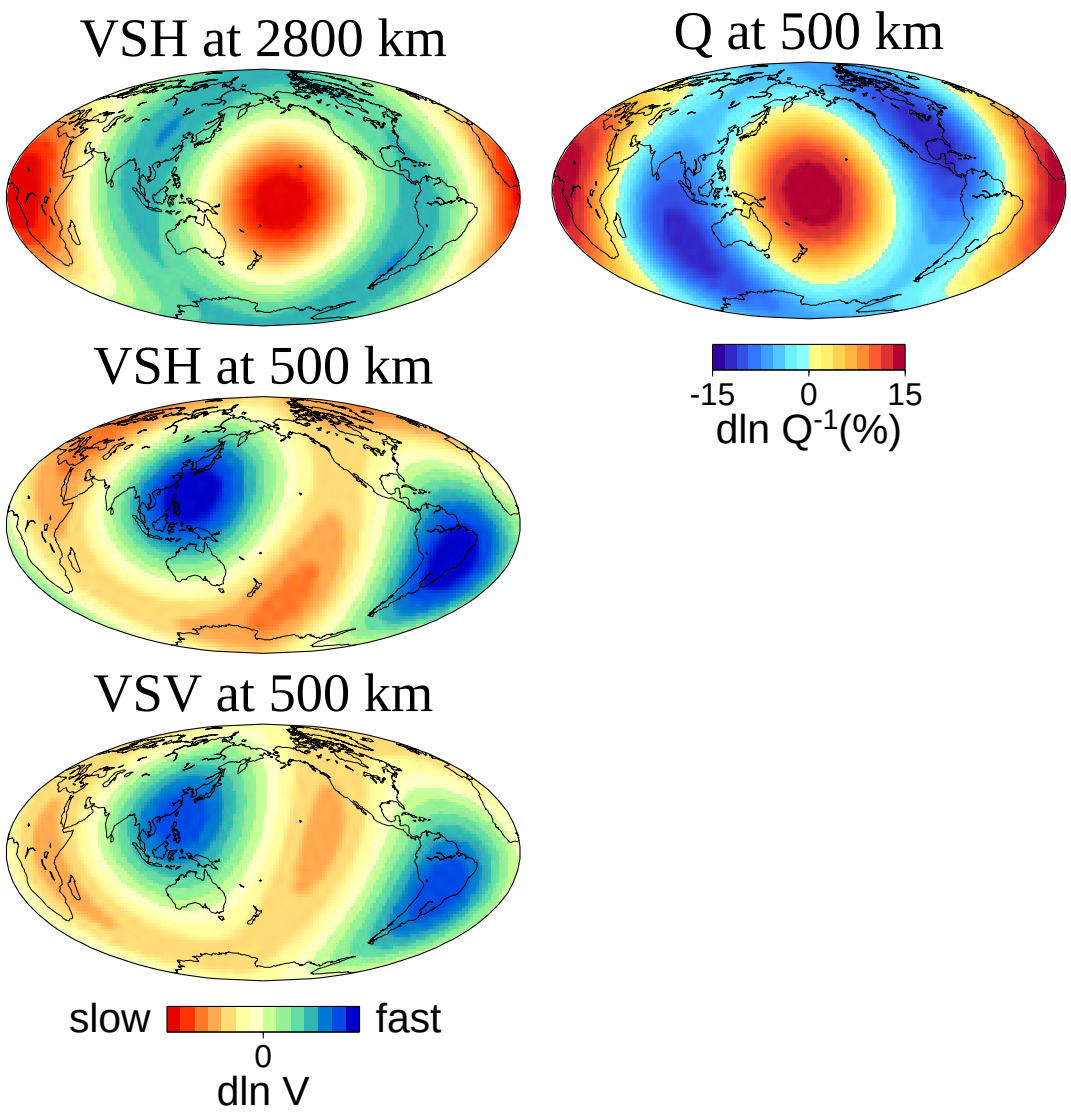


Figure 4.2: Comparison of the degree 2 distribution of $Q^{-1}$ in the upper mantle transition zone (depth of 500 km) for model *QRLW8*, with the corresponding distribution in *SH* and *SV* velocity, as well as with *SH* velocity at 2800 km. The *SH* model is *SAW24B16* [*Mégnin & Romanowicz*, 1999b]. The *SV* model *SAW16BV* [*Gung & Romanowicz*, 2003] was derived in the course of the present study. There is no corresponding *SV* velocity model for the deepest mantle, as the sampling of *SV* at those depths is poorer than for *SH*. Note that the velocity models in the transition zone correlate better with slabs than with superplumes.

Figure 4.3: Bottom panels: Map views of model *QRLW8* centered on (a) the Pacific and (b) Africa. Top panels: Depth cross-sections along profiles indicated in the bottom panels showing, for each profile (top to bottom), $smax = 8$ distribution of anisotropy ($V_{SH} - V_{SV}$) and $Q^{-1}$ in the upper mantle, and $smax = 24$ $V_{SH}$ distribution in the lower mantle. The upper mantle cross-sections start at 80 km depth because our $Q^{-1}$ modeling does not have resolution above that depth. Mid-ocean ridge positions are indicated by arrows. Note that the position of the high attenuation regions in the transition zone above the lowermost mantle low velocity minima. We show $V_{SH} - V_{SV}$ rather than velocities themselves, because the latter are contaminated by anisotropy, which hides the thermal signal. Zones of positive $V_{SH} - V_{SV}$ in the uppermost mantle (blue) correspond to zones where the high $Q^{-1}$ regions are shifted horizontally with respect to their transition zone location. This shift in $Q^{-1}$ is well resolved, as indicated by synthetic tests. The superplumes have complex shapes, especially under Africa, where the superplume appears to have several branches, consistent with observations of experimental fluid dynamics [*Davaille*, 1999]. Ridges are generally shallow features (e.g. at S,N and B), except in the south Atlantic (at M) where the ridge is also connected to the deeper high attenuation zone under south America. Note that $V_{SH} - V_{SV}$ is negative at shallow depths under the African cratons, consistent with other studies [*Babuska et al.*, 1998]. Maps and cross-sections show relative variations with respect to the average velocity or $Q^{-1}$ at each depth, for which the relation to temperature is not well determined, nor is the amplitude of the lateral variations in $Q^{-1}$ well constrained. Therefore it is not possible to compare temperatures beneath ridges and in the transition zone low $Q$ regions directly.

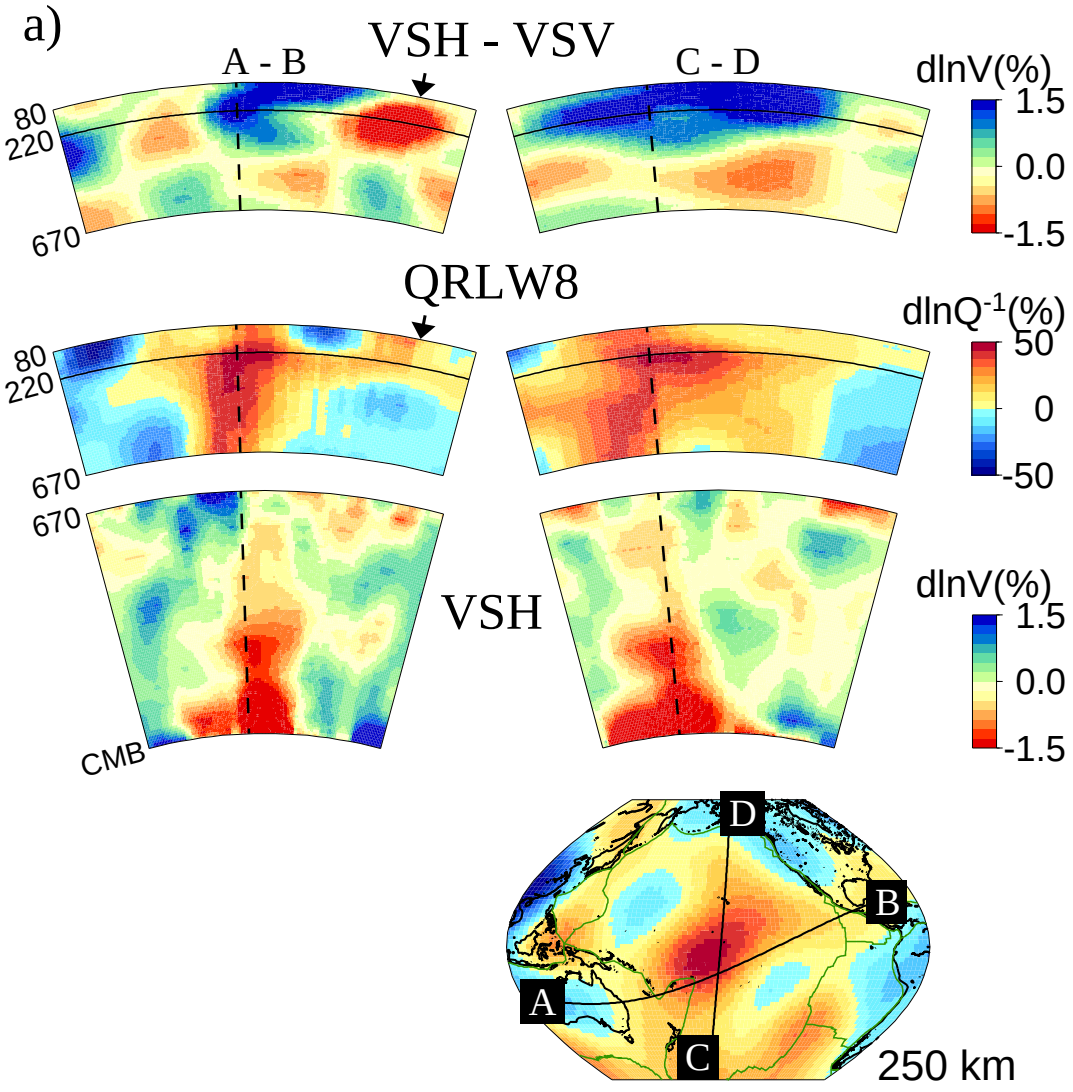
a)
VSH - VSV
A - B
C - D
dlnV(%)
1.5
0.0
-1.5
80
220
670
QRLW8
dlnQ-1(%)
50
0
-50
670
VSH
CMB
D
B
A
C
250 km

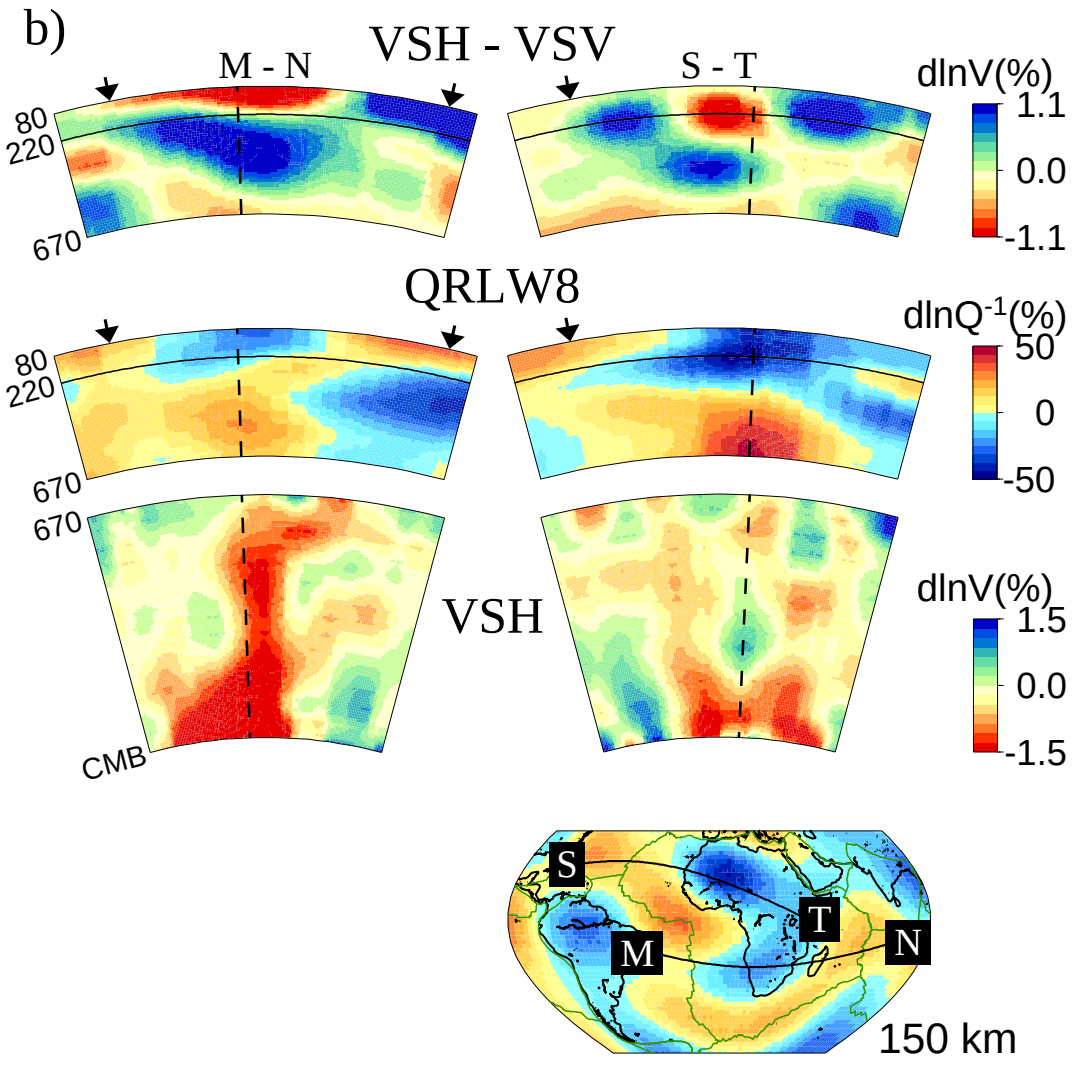
b)
VSH - VSV
M - N
S - T
dlnV(%)
1.1
0.0
-1.1
80
220
670
QRLW8
dlnQ-1(%)
50
0
-50
670
VSH
dlnV(%)
1.5
0.0
-1.5
CMB
S
T
M
N
150 km

# Chapter 5

# Global Anisotropy and Thickness of Continents

This chapter has been published in *Nature* [*Gung et al.*, 2003] under the title: 'Global anisotropy and the thickness of continents.'

## Summary

For decades there has been a vigorous debate about the depth extent of continental roots [*Jordan*, 1975; *Anderson*, 1990]. The analysis of heat flow [*Jaupart et al.*, 1998], mantle xenoliths [*Rudnick et al.*, 1998] and electrical conductivity [*Hirth et al.*, 2000] indicate that the coherent, conductive part of continental roots is not much thicker than 200-250 km. Some global seismic tomographic models agree with this estimate but others indicate a much thicker zone of fast velocities under continental shields [*Masters et al.*, 1996; *Ritsema et al.*, 1999; *Mégnin & Romanowicz*, 1999b; *Ekström & Dziewonski*, 1998], reaching at least 400 km depth. Here we show that the disagreement can be reconciled by taking into account anisotropy. Significant

radial anisotropy with $V_{SH} > V_{SV}$ is present under most cratons in the depth range 250-400 km, similar to that reported earlier [*Ekström & Dziewonski*, 1998; *Montagner & Tanimoto*, 1991] at shallower depths (80-250 km) under ocean basins. We propose that in both cases, this anisotropy is related to shear in the asthenospheric channel, located at different depths under continents and oceans. The seismically defined tectosphere is then at most 200-250 km thick under old continents. The Lehmann discontinuity, observed mostly under continents around 200-240 km, and the Gutenberg discontinuity, observed under oceans at shallower depths ($\sim$ 60-80 km), may both be associated with the bottom of the lithosphere, marking a transition to flow-induced asthenospheric anisotropy.

## 5.1 Introduction

The maximum thickness of the lithosphere, defined as a region of distinctly faster than average seismic velocities (1.5-2%) in global $S$ velocity tomographic models, ranges from 200-400 km, depending on the model [*Masters et al.*, 1996; *Ritsema et al.*, 1999; *Mégnin & Romanowicz*, 1999b; *Ekström & Dziewonski*, 1998]. This is manifested by a drop in correlation between some models from $\sim$0.80 at 100 km to less than 0.45 at 300 km depth (Figure 5.1a), which casts some doubt on the ability of global tomography to resolve upper mantle structure accurately. However, although global $V_S$ models differ from each other significantly in the depth range 200-400 km under the main continental shields, these differences are consistent when they are classified into three categories, depending on the type of data used to derive them: $SV$ (mostly vertical or longitudinal component data, dominated by Rayleigh waves in the upper mantle), $SH$ (mostly transverse component data, dominated by Love waves), and (3) *hybrid* (three-component data). $SH$ and hybrid models are better correlated with each other than with $SV$ models. This difference is accentuated when the correlation

is computed only across continental areas, as shown in Figure 5.1b, models *S20ASH* [*Ekström & Dziewonski*, 1998] (an *SH* model) and *SB4L18* [*Masters et al.*, 1996] (a hybrid model) correlate better with *SAW24B16* [*Mégnin & Romanowicz*, 1999b] (an *SH* model) than with models *S20ASV* [*Ekström & Dziewonski*, 1998] and *S20RTS* [*Ritsema et al.*, 1999], which are both *SV* models. The reduced correlation in the depth range 250-400 km between *SH* and hybrid models and *SV* models is strongly accentuated over continents. Also, *SH* (and hybrid) models exhibit continental roots that exceed those of *SV* models by 100 km or more, as illustrated in Figure 5.2 and Figure 5.3.

On the other hand, global tomographic studies that account for seismic anisotropy, either by inverting three-component data for $V_{SV}$ and $V_{SH}$ using isotropic kernels [*Ekström & Dziewonski*, 1998], or in the framework of more general anisotropic theory [*Montagner & Tanimoto*, 1991] , have documented significant lateral variations in the anisotropic parameter $\xi = (V_{SH}/V_{SV})^2$ on a global scale. Until now, attention has focused mostly on the strong positive values of $\delta \ln \xi = 2(\delta \ln V_{SH} - \delta \ln V_{SV})$ observed in the central part of the Pacific Ocean in the depth range 80-200 km. The presence of this anisotropy has been related to shear flow in the asthenosphere, with a significant horizontal component. Deeper anisotropy was suggested, but not well resolved in these studies, either because the dataset was limited to fundamental mode surface waves [*Montagner & Tanimoto*, 1991], or because of the use of inaccurate depth sensitivity kernels [*Ekström & Dziewonski*, 1998]. In particular, it is important to verify that any differences in $V_{SV}$ and $V_{SH}$ observed below 200 km depth are not an artifact of simplified theoretical assumptions, which ignore the influence of radial anisotropy on depth sensitivity kernels. (See Figure 5.4 for a comparison of isotropic kernels and anisotropic $V_S$ kernels).

## 5.2 Results and discussions

We have developed an inversion procedure for transverse isotropy using three-component surface and body waveform data, in the framework of normal mode asymptotic coupling theory [*Li & Romanowicz*, 1995], which in particular, involves the use of 2D broadband anisotropic sensitivity kernels appropriate for higher modes and body waves (see **Methods**). Figure 5.5 shows the distributions of $V_{SH}$, $V_{SV}$ and $\xi$ in the resulting degree 16 anisotropic model (*SAW16AN*), at depths of 175 km, 300 km and 400 km. At 175 km depth, the global distribution of $\delta \ln \xi$ confirms features found in previous studies, and is dominated by the striking $\delta \ln \xi > 0$ ($V_{SH} > V_{SV}$) anomaly in the central Pacific [*Montagner & Tanimoto*, 1991; *Ekström & Dziewonski*, 1998] and a similar one in the Indian Ocean. However, at depths greater than 250 km, the character of the distribution changes: positive $\delta \ln \xi$ emerges under the Canadian Shield, Siberian Platform, Baltic Shield, southern Africa, Amazonian and Australian cratons, while the positive $\delta \ln \xi$ fades out under the Pacific and Indian oceans. At 300 km depth, the roots of most cratons are characterized by positive $\delta \ln \xi$, which extend down to about 400 km. These features are emphasized in depth cross sections across major continental shields (Figure 5.6 , where we compare $V_{SH}$ and $V_{SV}$ distributions, consistently showing deeper continental roots in $V_{SH}$. The presence of anisotropy at depths greater than 200 km, with $V_{SH} > V_{SV}$, is also consistent with some regional studies [*Tong et al.*, 1994; *Debayle & Kennett*, 2000]. Interestingly, the East Pacific Rise has a signature with $\delta \ln \xi < 0$ down to 300 km, indicative of a significant component of vertical flow. At 400 km depth, we also note the negative values of $\delta \ln \xi$ around the Pacific ring, consistent with quasi-vertical flow in the subduction zone regions in the western Pacific and south America.

There has been a long-lasting controversy regarding the interpretation of shear wave splitting observations under continents, with some authors advocating frozen anisotropy in the lithosphere [*Silver*, 1996], and others, flow induced anisotropy related to present day plate motions [*Vinnik et al.*, 1992]. *SKS* splitting measurements do not have

adequate depth resolution, and inferences that have been made on the basis of a lithospheric thickness of 400 km or more under cratons need to be revisited.

Temperatures in the 250-400 km depth range exceed $1000°C$, and are therefore too high to allow sustained frozen anisotropy in a mechanically coherent lithospheric lid on geologically relevant time scales [*Vinnik et al.*, 1992]. Therefore we infer that the $V_{SH} > V_{SV}$ anisotropy we describe here must be related to present day flow-induced shear, with a significant horizontal component. Such an interpretation is also compatible with results from shear wave splitting, which document the presence of anisotropy below cratons indicating simple-shear deformation parallel to present day plate motion, at least in North America [*Fouch et al.*, 2000; *Bokelmann*, 2002] and Australia [*Debayle & Kennett*, 2000]: some recent studies indicate that there may be two zones of *SKS* anisotropy under continental shields, one shallower, reflecting past geological events, and one deeper, related to present day flow [*Fouch et al.*, 2000; *Levin et al.*, 1999].

We note the similarity of the character of $V_{SH} > V_{SV}$ anisotropy, in the depth range 200-400 km under cratons, and 80-200 km under ocean basins, and we suggest that both are related to shear in the asthenosphere, the difference in depth simply reflecting the varying depth of the asthenospheric channel. Although our inference is indirect, it reconciles tomographic studies with other geophysical observations of lithospheric thickness based on heat flow [*Jaupart et al.*, 1998], xenoliths [*Rudnick et al.*, 1998] and mantle electrical conductivity [*Hirth et al.*, 2000]. It is also in agreement with lateral variations in attenuation on the global scale [*Romanowicz & Gung*, 2002].

Another contentious issue is the nature of the Lehmann discontinuity ($L$), and in particular the puzzling observation that it is not a consistent global feature [*Shearer*, 1990], but is observed primarily in stable continental areas and not under oceans [*Gu et al.*, 2001b; *Revenaugh & Jordan*, 1991]. *Levin et al.* [1981] first proposed that $L$ might be an anisotropic discontinuity, and more recent studies have suggested that $L$ is a rheological boundary marking a transition from anisotropic to isotropic

structure [*Karato*, 1993; *Gaherty & Jordan*, 1995]. Since the $V_{SH} > V_{SV}$ anisotropy under continental cratons is found deeper than 200 km, we propose that $L$ actually marks the top of the asthenospheric layer, a transition from weakly anisotropic lowermost continental lithosphere to anisotropic asthenosphere, in agreement with the inference of [*Levin et al.*, 1981]. Under oceans, the lithosphere is much thinner, and the lithosphere/asthenosphere boundary occurs at much shallower depths. There is no consistently observed discontinuity around 200-250 km depth [*Shearer*, 1990]. On the other hand, a shallower discontinuity, the Gutenberg discontinuity ($G$), is often reported under oceans and appears as a negative impedance reflector in studies of precursors to multiple *ScS* [*Revenaugh & Jordan*, 1991]. The difference in depth of the observed $\delta \ln \xi > 0$ anisotropy between continents and oceans is consistent with an interpretation of $L$ and $G$ as both marking the bottom of the mechanically coherent lithosphere, in areas where it is quasi-horizontal (Figure 5.7).

In this study, we only consider radial anisotropy, which in particular does not account for horizontal or tilted orientation of the fast axis of anisotropy [*Montagner*, 1994]. We can only infer that regions with significantly positive $\delta \ln \xi$ are regions where anisotropy has a significant horizontal component, and expresses the alignment of olivine crystals in predominantly horizontal flow [*Montagner*, 2002]. In regions of transition between cratons and younger continental provinces, or between ocean and continent, the asthenospheric flow would follow the inclined shape of the bottom of the lithosphere and be detected less clearly with our approach.

Thus, the inspection of radial anisotropy in the depth range 200-400 km allows us to infer that continental roots do not extend much beyond 250 km depth, in agreement with other geophysical observations. The part of the mantle under old continents that translates coherently with plate motions need not be thicker than 200-250 km. Tomographic models reveal the varying depth of the top of the anisotropic asthenospheric channel, marked by a detectable seismic discontinuity called $L$ under continents (about 200-250 km depth), and $G$ under oceans (about 60-80 km depth). Finally, seemingly incompatible tomographic models obtained by different researchers can thus also be

reconciled: the relatively poor correlation between different models in the depth range 250-400 km is not due to a lack of resolution of the tomographic approach, but rather to the different sensitivity to anisotropy of different types of data.

# Methods

### Broadband sensitivity kernels

In this study, we invert three-component long period seismograms in the time domain (down to periods of 60 seconds for surface waves, 32 seconds for body waves) in the framework of non-linear asymptotic coupling theory (*NACT*) [*Li & Romanowicz*, 1995], a normal-mode perturbation-based approach which takes into account the concentrated sensitivity of body-waves to structure along the ray path, in contrast to standard approaches which assume 1D kernels, an approximation which is valid only for fundamental mode surface waves. Our technique involves dividing the seismogram into wavepackets that may contain one or more seismic phases, and applying weighting factors to equalize the contribution of large and small amplitude wavepackets in the least squares inversion.

### Transverse isotropy

A transversely isotropic medium with vertical axis of symmetry is described by density $\rho$ and five elastic parameters, usually $A$ $(= \rho V_{PH}^2)$, $C$ $(= \rho V_{PV}^2)$, $L$ $(= \rho V_{SV}^2)$, $N$ $(= \rho V_{SH}^2)$ and $F$. We start by considering, equivalently, the 6 parameters $V_{SH}$, $V_{SV}$, $\eta$ $(= F/(A-2L))$, $V_{Piso}$ (isotropic $Vp$), $\phi$ $(= C/A)$ and $\rho$, with appropriate kernels for weak transverse anisotropy. To reduce the number of parameters in the inversion and keep only those that are best resolved ($V_{SH}$ and $V_{SV}$), we assume the following scaling relations, as inferred from laboratory experiments for depths relevant to our study (i.e., less than 500 km) [*Montagner & Anderson*, 1989] :

$$
\begin{aligned}
\delta \ln V_{Piso} &= 0.5 \ \delta \ln V_{Siso} \\
\delta \ln \eta &= -2.5 \ \delta \ln \xi \\
\delta \ln \phi &= -1.5 \ \delta \ln \xi \\
\delta \ln \rho &= 0.3 \ \delta \ln V_{Siso} \\
\delta \ln V_{Siso} &\approx 2/3 \ \delta \ln V_{SV} + 1/3 \ \delta \ln V_{SH}
\end{aligned}
$$

We have verified that the main features of our results are not affected by the particular values chosen in these relations.

Starting from our most recent tomographic models, *SAW24B16* for $V_{SH}$ and *SAW16BV* [*Gung & Romanowicz*, 2003] for $V_{SV}$, we invert for perturbations in $V_{SH}$ and $V_{SV}$ in a spherical harmonic expansion up to degree 16 laterally. Radiall parameterization is in terms of cubic splines. Since our sampling of the lowermost mantle with $SV$-sensitive body waves is limited, in order to avoid bias from anisotropy in D", we restricted our inversion to the top 1500 km of the mantle, and chose the body waveforms to include in the dataset accordingly.

We have performed synthetic tests to check that our results, and in particular the observation of radial anisotropy under continents at depths greater than 200 km, are not artifacts due to poor resolution in the inversion for either $V_{SH}$ or $V_{SV}$. For example, Figure 5.8 shows the results of an experiment in which synthetic transverse component seismograms were computed for a starting $SV$ model (no roots below 250 km), mimicking the actual distribution of our dataset, and then reinverted for an $SH$ model. No deep continental roots are apparent in the resulting model.

Assuming lattice preferred orientation (LPO) of anisotropic minerals such as olivine, and as illustrated for example by *Montagner* [2002], a large-scale predominantly horizontal flow is characterized by a positive value of $\delta \ln \xi$ and also significant *SKS* wave splitting. The direction of the fast axis inferred from the latter is related to the direction of the flow in the horizontal plane. Coupling between Love and Rayleigh

waves that may arise in the case of anisotropy with a non-vertical axis of symmetry affects mainly the wave amplitudes. Since we are primarily fitting the phase of the seismograms, such coupling should have little influence on our results.

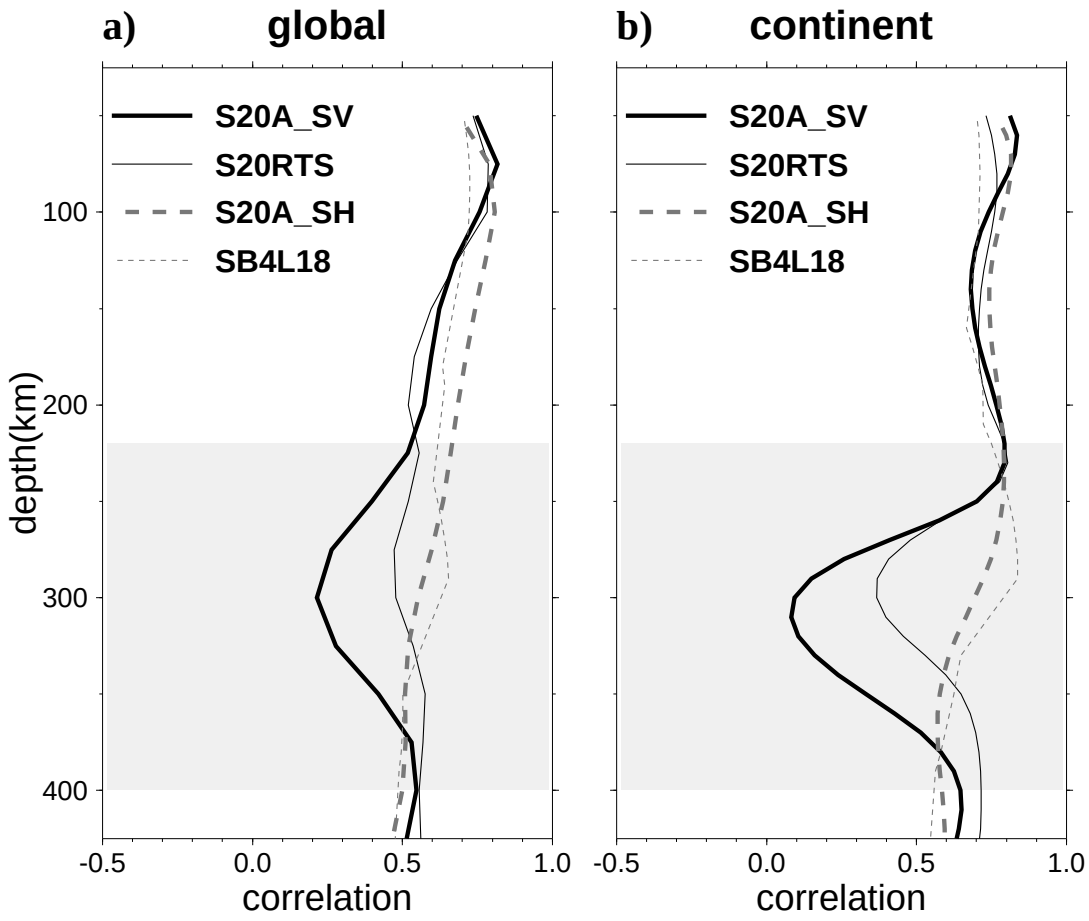


Figure 5.1: Correlation coefficient as a function of depth between model *SAW24B16*, an *SH* model, and other global tomographic *S* velocity models. (a) correlation computed over the whole globe; (b) correlation computed over continental areas only. Here continents include all areas of elevation greater than -0.5 km. Note that models *S20ASH* (an *SH* model) and *SB4L18* (a hybrid model) correlate better with *SAW24B16* than do models *S20ASV* and *S20RTS*, which are both *SV* models. The reduced correlation in the depth range 250-400 km between *SH*/hybrid models and *SV* models is strongly accentuated over continents.

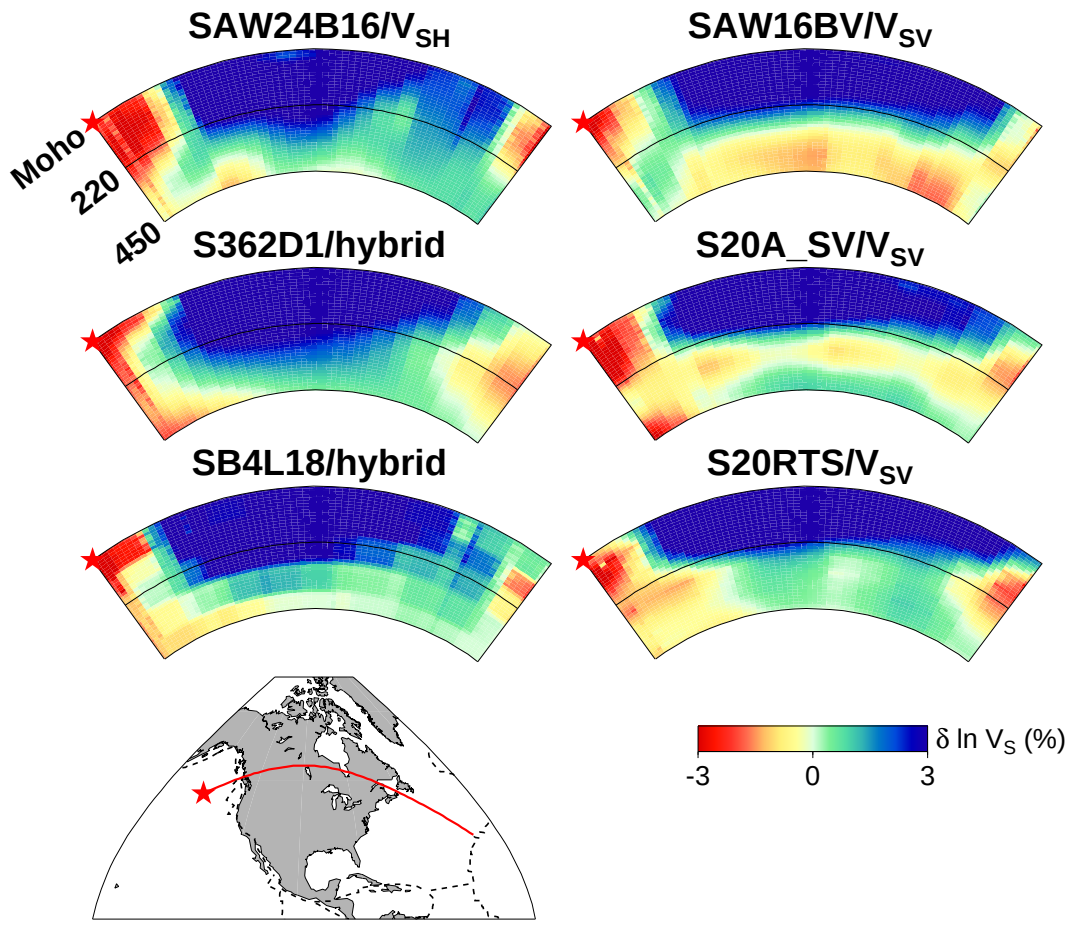


Figure 5.2: Depth cross-sections of the Canadian Shield, for different *SH*/hybrid (left) and *SV* (right) global tomographic models. The models on the left consistently exhibit continental roots that exceed 220 km depth, whereas the models on the right do not.

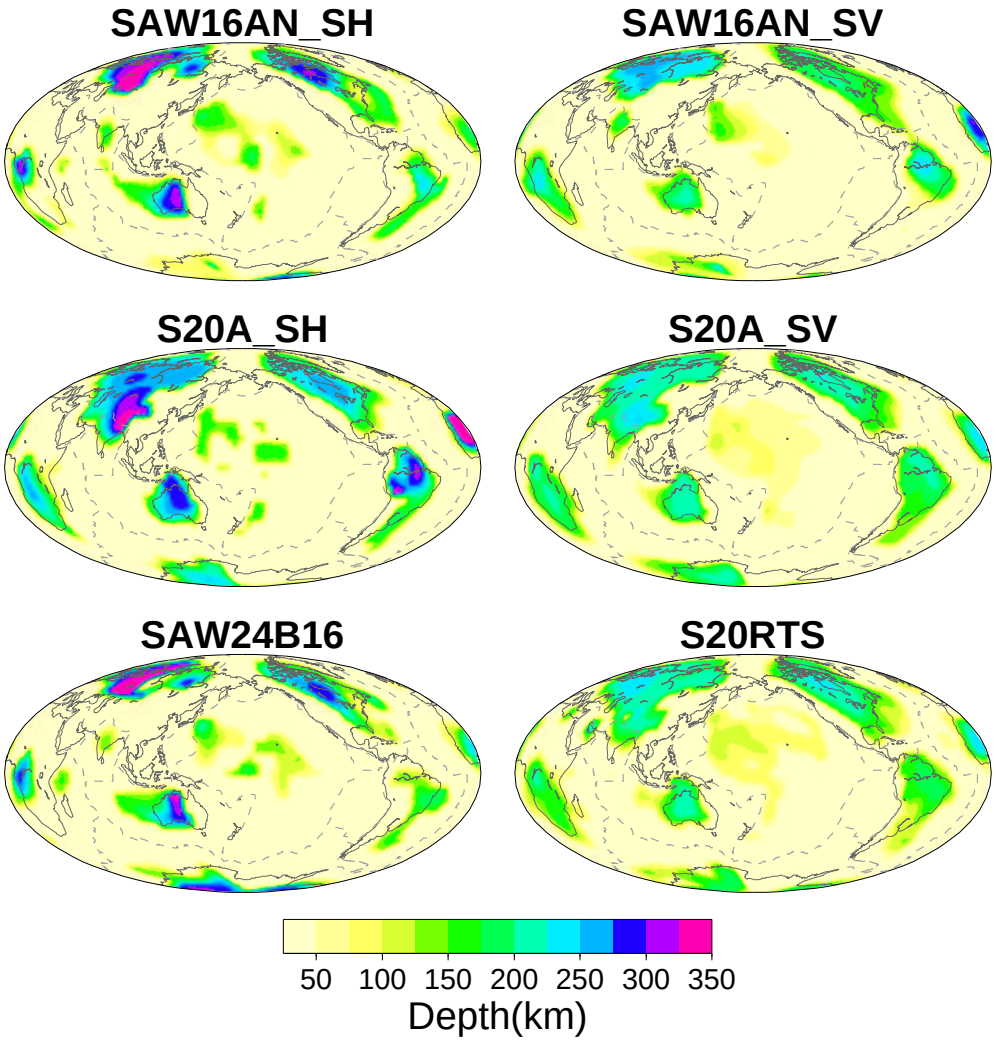


Figure 5.3: Maximum depth for which the velocity anomaly with respect to the reference model *PREM* is greater than 2%, for different $S$ velocity models. Left: *SH* type models; right: *SV* type models. Bottom: *SH* model *SAW24B16* compared to *SV* model *S20RTS*; middle: *SH* and *SV* parts of model *S20A*; top: *SH* and *SV* parts of anisotropic model *SAW16AN* discussed here. While the roots of continents generally extend to depths greater than 300-350 km in *SH* models, they do not exceed 200-250 km in *SV* models.

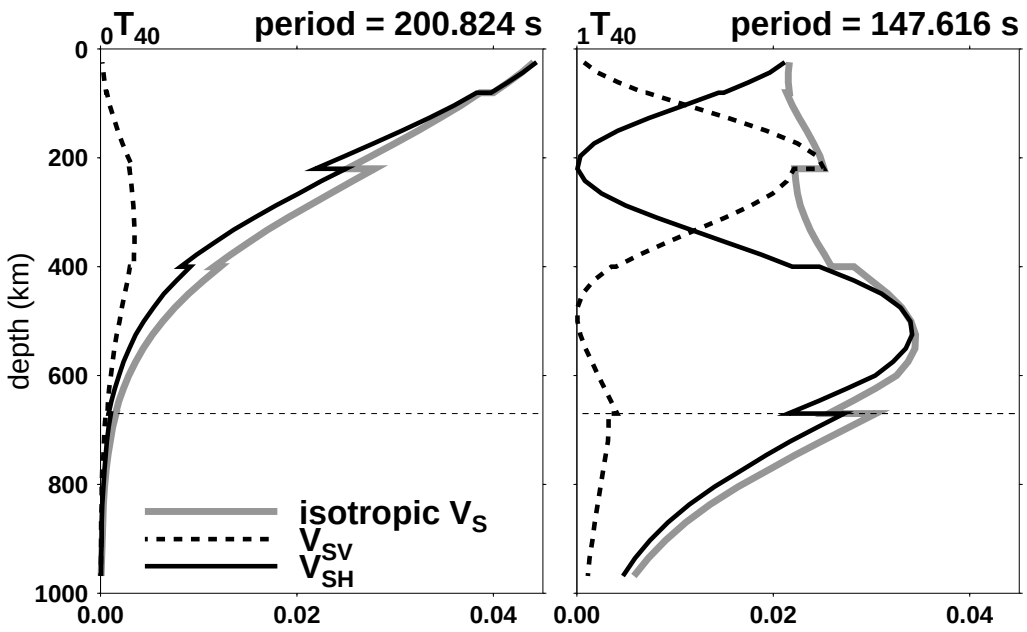


Figure 5.4: Examples of depth sensitivity kernels for toroidal modes ${}_0\mathrm{T}_{40}$ (left) and ${}_1\mathrm{T}_{40}$ (right), comparing the isotropic $V_S$ kernels (grey line) with anisotropic kernels (black continuous and dotted lines). For the fundamental mode, there is not much difference between isotropic and anisotropic $V_{SH}$ kernels, whereas for the overtone, the difference is significant in the top 400 km.

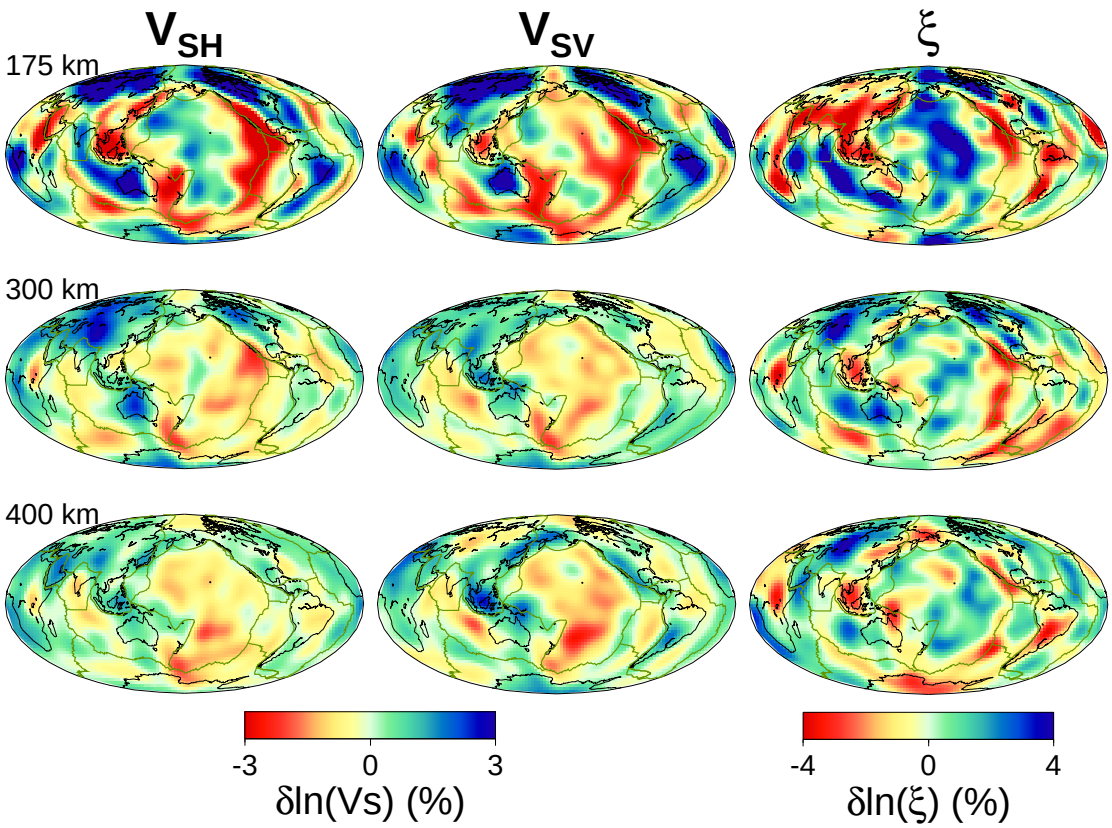


Figure 5.5: Maps of relative lateral variations in $V_{SH}$, $V_{SV}$ and $\xi$ of model *SAW16AN* at three depths in the upper mantle ($\delta \ln \xi = 2(\delta \ln V_{SH} - \delta \ln V_{SV})$). Lateral variations are referred to reference model *PREM*, which is isotropic below 220 km depth, but has significantly positive $\delta \ln \xi$ at 175 km depth.

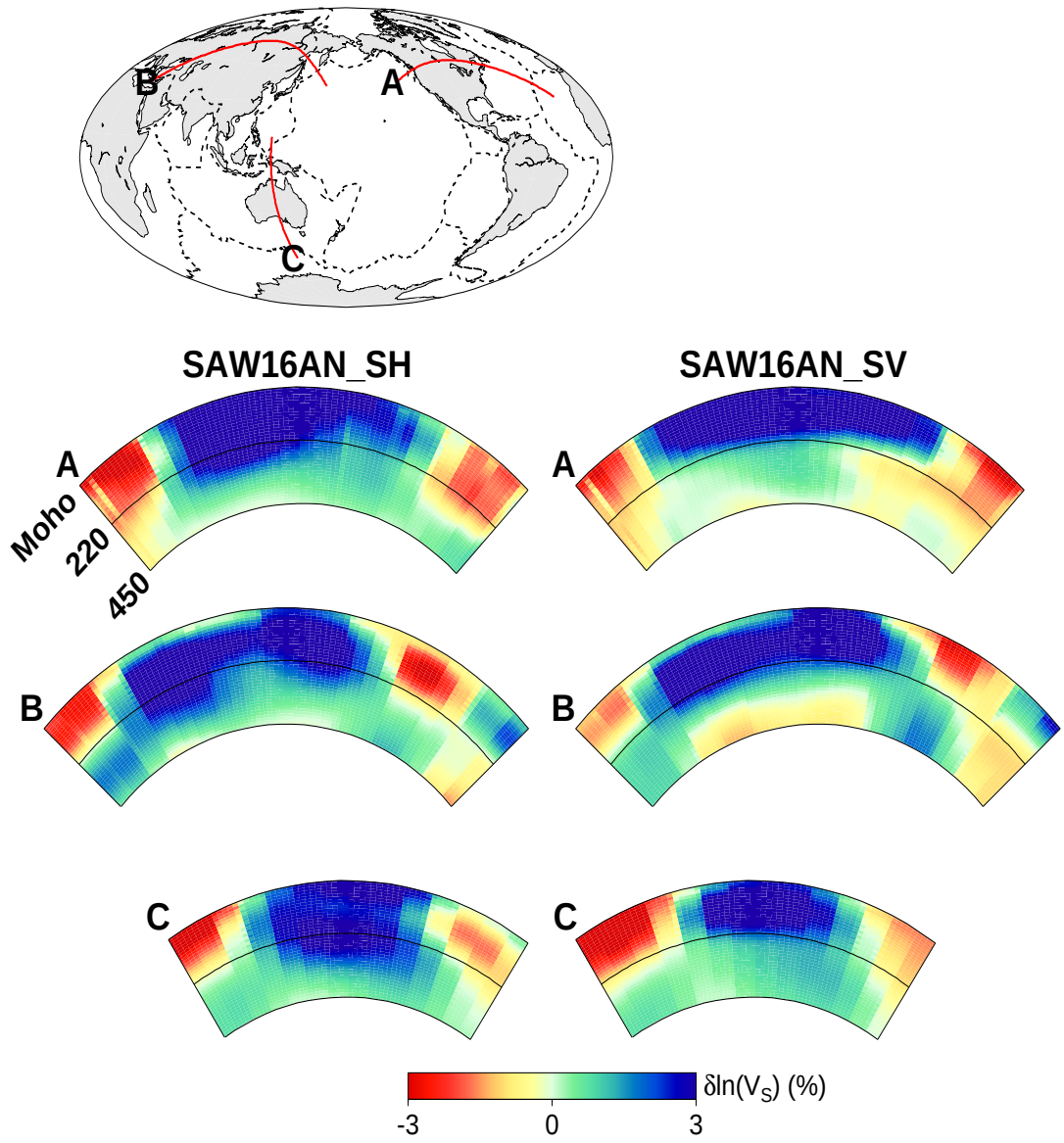


Figure 5.6: Depths cross-sections through three continents (see location at top) showing the *SH* (left) and *SV* (right) components of anisotropic model *SAW16AN*. The *SH* sections consistently indicate fast velocities extending to depths in excess of 220 km, whereas the *SV* sections do not. In section B, the higher velocity associated with the subduction under Kamchatka is clearly visible in *SV* but not as clearly in *SH*. This anisotropy may explain why subduction zones are generally less visible in *S* tomographic models (mostly of the hybrid type, thus more sensitive to *SH*) than in *P* models.

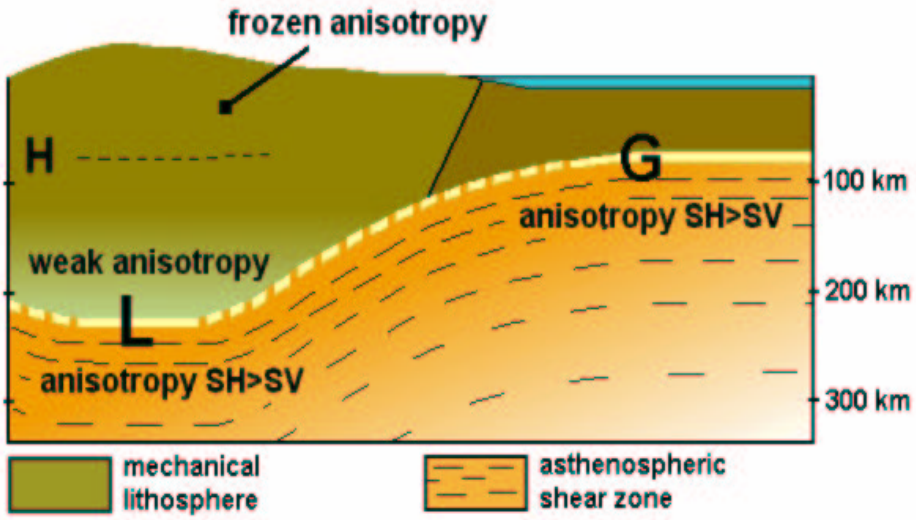


Figure 5.7: Sketch illustrating our interpretation of the observed anisotropy in relation to lithospheric thickness, and its relationship to Lehmann ($L$) and Gutenberg ($G$) discontinuities. The Hales discontinuity ($H$) is also shown. H is generally observed as a positive impedance embedded within the continental lithosphere in the depth range 60-80 km. H and G might not be related.

Figure 5.8: Results of a synthetic test in which an input model (middle panels) of the *SV* type is considered (without deep lithospheric roots). Synthetic seismograms for *SH* component data with the same distribution as our real data are computed. The synthetic data are then inverted for *SH* structure, starting from an *SH* model (*SAW24B16*) that exhibits deep continental roots (left panels). In the resulting fitted model, no deep continental roots, remain consistent with the input model. The right-most panel shows the correlation as a function of depth of the output model, with, respectively, the input model (*SV*) and the starting model (*SH*). The results of this test indicate that the differences in *SH* and *SV* models in the depth range 250-400 km are not an artifact of the inversion process, or of the different depth sensitivities of various *SH* and *SV* sensitive phases present in the data.

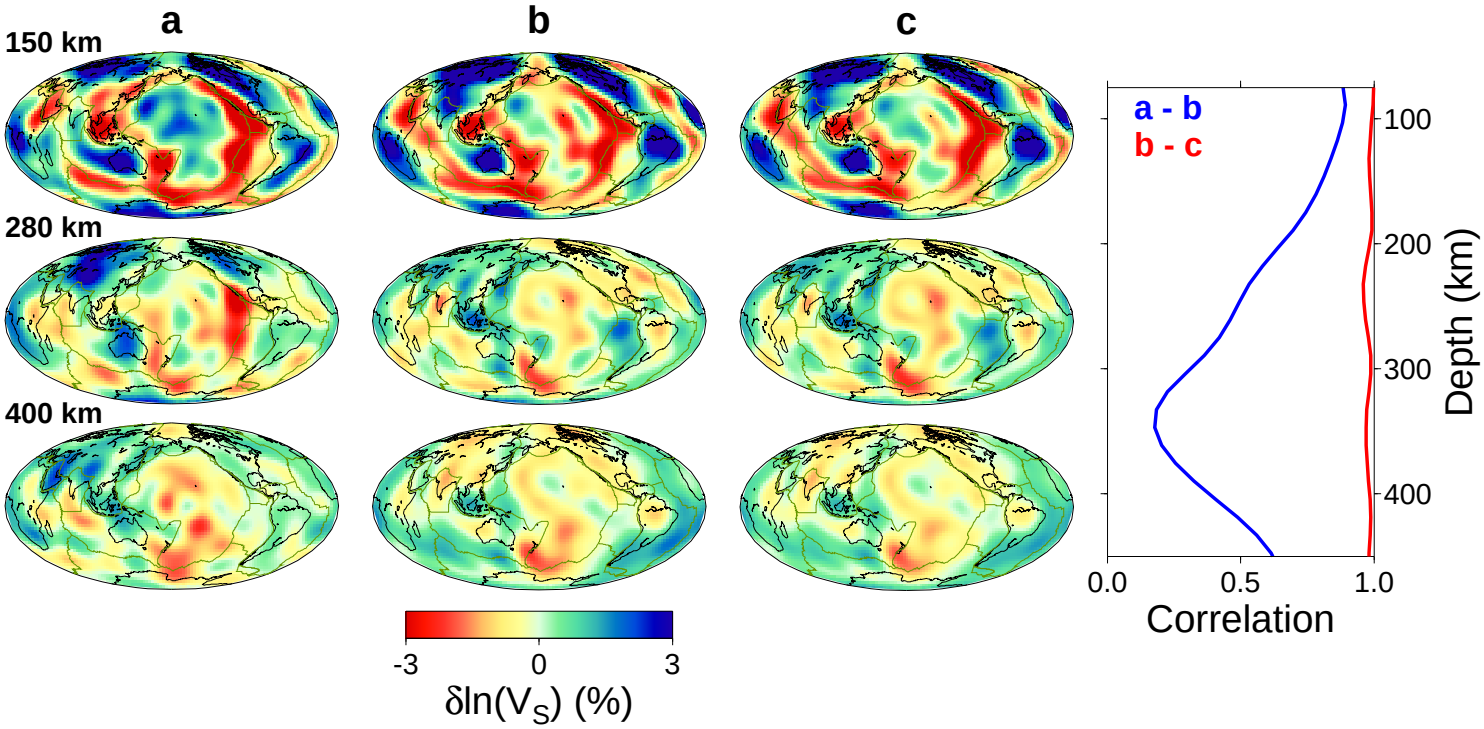
a
b
c
150 km
280 km
400 km
-3
0
3
δln(V_S) (%)
a - b
b - c
100
200
300
400
Depth (km)
0.0
0.5
1.0
Correlation

# Chapter 6

# Conclusions

Using normal mode asymptotic coupling theory and three-component seismic waveform data, we imaged the three-dimensional structure in attenuation and anisotropy for the Earth's upper mantle. Here we summarize the key features and implications of the models.

The degree 8 $Q$ model *QRLW8* shows a generally tectonic-related $Q$ distribution in the uppermost mantle, which is similar to that observed in elastic velocity models, with regions of high/low $Q$ correlated with regions of high/low velocity. Below 250 km, the tectonic-related pattern is gradually replaced by a pattern well correlated with the $V_S$ velocity distribution in the lowermost mantle, with strong low $Q$ minima centered under the southern Pacific and under Africa. Most surface hot spot positions are above the low $Q$ areas in the upper mantle transition zone. The comparison of *QRLW8* and whole mantle velocity models suggests: (1) Upwellings associated with the two large superplumes, imaged by seismic elastic tomography at the base of the mantle, persist through the upper-mantle transition zone, and are deflected horizontally beneath the lithosphere. (2) The two superplumes may play a major and stable role in supplying heat and horizontal flow to the low viscosity asthenospheric channel, lubricating plate motions and feeding hotspots. (3) More heat may be carried through the core-mantle

boundary than is accounted for by hot-spot flux alone.

The degree 16 anisotropy model, *SAW16AN*, confirms the existence of transverse isotropy with $V_{SH} > V_{SV}$ under the central Pacific and Indian oceans in the depth range 100-200 km. At greater depth (250-400 km), pronounced $V_{SH} > V_{SV}$ signals are observed under most continental cratons. The characteristics of *SAW16AN* and other geophysical evidence lead us to propose: (1) This anisotropy is related to shear in the asthenospheric channel, located at different depths under continents and oceans. The seismically defined tectosphere is then at most 200-250 km thick under old continents. (2) The Lehmann discontinuity and the Gutenberg discontinuity may both be associated with the bottom of the lithosphere, marking a transition to flow-induced asthenospheric anisotropy. (3) Seemingly incompatible tomographic models obtained by different researchers can thus be reconciled: the relatively poor correlation between different models in the depth range 250-400 km is mainly due to the sensitivities of different types of data to anisotropy.

Future work will incorporate focusing effects in the computation of synthetic waveforms for the construction of the next generation $Q$ model. In the first step, this will be done using higher order asymptotics, as described in this thesis. As *SEM* computations become more accessible, it will be possible, in the second step, to account for the elastic effects in a more exact fashion.

# Bibliography

Aki, K. and P.G. Richards, *Quantitative Seismology: theory and methods,* W. H. Freeman, New York, 1980.

Anderson, D.L., The deep structure of continents, *J. Geophys. Res.*, **84**, 7555-7560, 1990.

Anderson, D.L., Topside Tectonics, *Science*, **293**, 2016-2018, 2001.

Artemieva, I.M. and W.D. Mooney, Thermal thickness and evolution of Precamvrian lithosphere: a global study, *J. Geophys. Res.*, **106,** 16,387-16,414, 2001.

Babuska, V., J.P. Montagner, J. Plomerova and N. Girardin, Age-dependent large-scale fabric of the mantle lithosphere as derived from surface wave velocity anisotropy, *Pure Appl. Geophys.*, **121**, 257-280, 1998.

Bercovici, D., Y. Ricards and M.A. Richards, *The relation between mantle dynamics and plate tectonics: a primer, the history and dynamics of global plate motions, AGU Geophysical Monograph*, **21**, 5-46, 2000.

Bhattacharyya, J., G. Master and P. Shearer, Global lateral variations of shear wave attenuation in the upper mantle, *J. Geophys. Res.* **101,** 22,273-22,289, 1996.

Billien, M., J.-J. Lévêque and J. Trampert, Global maps of Rayleigh wave attenuation for periods between 40 and 150 seconds, *Geophys. Res. Lett.*, **27,** 3619-3622, 2000.

Bokelmann, G.H.R., Which forces drive North America? *Geology*, **30**, 11, 1027-1030, 2002.

Burke, K., Since 200 Ma nearly all large igneous provinces (LIPs) have been emplaced above deep mantle low velocity volumes (DMLVVS). *EOS, Trans. Am. Geophys. Union*, **82** (F1134), 2001.

Capdeville Y., E. Chaljub, J.P. Vilotte and J.P. Montagner, Coupling the spectral element method with a modal solution for elastic wave propagation in global Earth models, *Geophys. J. Int.*, **152**, 34-66, 2003a.

Capdeville Y., A. To, and B. Romanowicz, Coupling spectral elements and modes in spherical Earth: an extension to the 'sandwich' case, *Geophys. J. Int.*, **154**, 44-57, 2003b.

Castillo, P., The Dupal anomaly as a trace of the upwelling lower mantle, *Nature*, **336**, 667-670, 1988.

Chalijb, E., Y. Capdeville & J-P Vilotte, Solving elastodynamics in a fluid-solid heterogeneous sphere: a parallel spectral element approximation on non-conforming grids, *J. Comput. Phys.*, **187**, 457-491, 2003.

Debayle, E. and B.L.N. Kennett, Anisotropy in the Australian upper mantle from Love and Rayleigh waveform inversion, *Earth Planet. Sci. Lett.*, **184**, 339-351, 2000.

Dahlen, F.A. and J. Tromp, *Theoretical global Seismology,* 1025 pp., Princeton University Press, Princeton, New Jersey, 1998.

Davaille, A., Simultaneous generation of hotspots and superswells by convection in a heterogeneous planetary mantle, *Nature*, **402**, 756-760, 1999.

Davies, G.F. and M.A. Richards, Mantle convection, *J. Geol.*, **100**, 151-206, 1992.

Ding, X.Y. and S.P. Grand, Upper mantle Q structure beneath the east pacific rise, *J. Geophys. Res.*, **98,** 1973-1985, 1993.

Durek, J.J., M.H. Ritzwoller and J.H. Woodhouse, Constraining upper mantle anelasticity using surface amplitudes, *Geophys. J. Int.*, **114,** 249-272, 1993.

Durek, J.J. and G. Ekström, A radial model of anelasticity consistent with long period surface wave attenuation, *Bull. Seism. Soc. Am.*, **86**, 144-158, 1996.

Dziewonski, A.M. and D.L. Anderson, Preliminary reference Earth model, *Phys. Earth planet. Inter.*, **25**, 297-356, 1981.

Dziewonski, A.M., G. Chou and J. H. Woodhouse, Determination of earthquake source parameters from waveform modeling, *J. Geophys. Res.*, **86,** 2825-2852, 1981.

Edmonds, A.R., *Angular momentum in quantum mechanics*, Princeton University Press, Princeton, New Jersey, 1960.

Ekström, G. and A.M. Dziewonski, The unique anisotropy of the Pacific upper mantle, *Nature*, **394,** 168-171, 1998.

Flanagan, M.P. and D.A. Wiens, Radial upper mantle attenuation structure of inactive back arc basins from differential shear wave measurements, *J. Geophys. Res.*, **99,** 15,469-15,495, 1994.

Forte, A.M. and J.X. Mitrovica, Deep-mantle high-viscosity flow and thermochemical structure inferred from seismic and geodynamic data, *Nature*, **410**, 1049-1056, 2001.

Fouch, M.J., K.M. Fischer, E.M. Parmentier, M.E. Wysession and T.J. Clarke, Shear wave splitting, continental keels, and patterns of mantle flow, *J. Geophys. Res.*, **105**, 6255-6275, 2000.

Foulger, G.R., M.J. Pritchard, B.R. Julian, J.E. Evans, R.M. Allen, G. Nolet, W.J. Morgan, B. Bergsson, P. Erlendsson, S. Jakobsdottir, S. Ragnarsson, R. Stefansson and K. Vogfjord, Seismic tomography shows that upwelling beneath Iceland is confined to the upper mantle, *Geophys. J. Int.*, **146**, 504-530, 2001.

Fukao, Y., S. Widiyantoro and M. Obayashi, Stagnant slabs in the upper and lower mantle transition region, *Rev. Geophys.*, **39**, 291-323, 2001.

Gaboret, C., A.M. Forte and J.P. Montagner, The unique dynamics of the pacific hemisphere mantle and its signature on seismic anisotropy, *Earth Planet. Sci. Lett.*, **208**, 219-233, 2003.

Gaherty, J.B. and Jordan, T.H., Lehmann discontinuity as the base of an anisotropic layer beneath continents, *Science*, **268**, 1468-1471, 1995.

Gilbert, F., Excitation of the normal modes of the Earth by earthquake sources, *Geophys. J. R. Astr. Soc.*, **22**, 223-226, 1971.

Grand, S.P., R.D. van der Hilst and S. Widiyantoro, Global seismic tomography: a Snapshot of convection in the Earth, *GSA Today*, **7**, No 4, 1-7, 1997.

Gu, Y., A.M. Dziewonski, W.J. Su and G. Ekström, Models of the mantle shear velocity and discontinuities in the pattern of lateral heterogeneities, *J. Geophys. Res.*, **106,** 11,169-11,200, 2001a.

Gu, Y., A.M. Dziewonski and G. Ekström, Preferential detection of the Lehmann discontinuity beneath continents, *Geophys. Res. Lett.*, **28**, 4655-4658, 2001b.

Gung, Y., M. Panning and B. Romanowicz, Global anisotropy and the thickness of continents, *Nature*, **422**, 707-711 2003.

Gung, Y. and B. Romanowicz, Q tomography of the upper mantle using three component long period waveforms, *submitted to Geophys. J. Int.* 2003.

Hager, B.H., R.W. Clayton, M.A. Richards, R.P. Comer and A.M. Dziewonski, Lower mantle heterogeneity, dynamic topography and the geoid, *Nature*, **313**, 541-545, 1985.

Hart, S.R., E. Hauri, L. Oschmann and J. Whitehead, Mantle plumes and entrainment: isotopic evidence, *Science*, **256**, 517-520, 1992.

van der Hilst, R.D., S. Widiyantoro and E.R. Engdahl, Evidence of deep mantle circulation from global tomography, *Nature*, **386**, 578-584, 1997.

Hirth, G., Evans, R.L. and Chave A.D. Comparison of continental and oceanic mantle electrical conductivity: is the Archean lithosphere dry? *Geochem. Geophys. Geosyst.*, **1**, 2000GC000048, 2000.

Jackson, I., M.S. Paterson and J.D. FitzGerald, Seismic wave dispersion and attenuation in Aheim dunite: an experimental study, *Geophys. J. Int.*, **108,** 517-534, 1992.

Jordan. T.H., The continental lithosphere, *Rev. Geoph. Space Phys.*, **13**, 1-12, 1975.

Jordan, T.H., A procedure for estimating lateral variations from low-frequency eigenspectra data, *Geophys. J. R. Astr. Soc.*, **52**, 441-455, 1978.

Jaupart, C., J.C. Mareschal and L. Guillou-Frottier, Heat flow and thickness of the lithosphere in the Canadian Shield, *J. Geophys. Res.*, **103**, 15,269-15,286, 1998.

Karato, S-I., On the Lehmann discontinuity, *Geophys. Res. Lett.*, **19**, 2255-2258, 1992.

Karato, S-I., Importance of anelasticity in the interpretation of seismic tomography, *Geophys. Res. Lett.*, **20,** 1623-1626, 1993.

Karato, S-I., A dislocation model of seismic wave attenuation and micro-creep in the earth: Harold Jeffreys and the rheology of the solid earth, *Pure Appl. Geophys.*, **153,** 239-256, 1998.

Komatitsch, D. and J.P. Vilotte, The spectral element method: an effective tool to simulate the seismic response of 2D and 3D geological structures, *Bull. Seism. Soc. Am.*, **88**, 368-392, 1998.

Leven, J.H., I. Jackson and A.E. Ringwood, Upper mantle seismic anisotropy and lithospheric decoupling, *Nature*, **289**, 234-238, 1981.

Levin, V., W. Menke and J. Park, Shear wave splitting in the Appalachians and the Urals: a case for multilayered anisotropy, *J. Geophys. Res.*, **104**, 17,975-17,993, 1999.

Levin, V. and J. Park, Shear zones in the Proterozoic lithosphere of the Arabian Shield and the nature of the Hales discontinuity, *Tectonophysics*, **323**, 131-148, 2000.

Li, X.D. and T. Tanimoto, Waveforms of long-period body waves in a slightly aspherical Earth model, *Geophys. J. R. Astr. Soc.*, **112**, 92-102, 1993.

Li, X.D. and B. Romanowicz, Comparison of global waveform inversions with and without considering cross-branch modal coupling, *Geophys. J. Int.*, **121**, 695-709, 1995.

Li, X.D. and B. Romanowicz, Global mantle shear-velocity model developed using nonlinear asymptotic coupling theory, *J. Geophys. Res.*, **101**, 22,245-22,272, 1996.

Masters, G., S. Johnson, G. Laske and H. Bolton, A shear-velocity model of the mantle, *Phil. Trans. R. Soc. London*, **354** 1,385-1,410, 1996.

Mégnin, C. and B. Romanowicz, The effects of theoretical formalism and data selection scheme on mantle models derived from waveform tomography, *Geophys. J. Int.*, **138,** 366-380, 1999.

Mégnin, C. and B. Romanowicz, The 3D shear velocity structure of the mantle from the inversion of body, surface and higher mode waveforms, *Geophys. J. Int.*, **143**, 709-728, 2000.

Mégnin, C., *The shear velocity structure of the mantle from the inversion of time-domain waveform data*, Ph.D. thesis, University of California at Berkeley, Berkeley, CA, 1999.

Minster, J.B. and D.L. Anderson, A dislocation-controlled theology for the mantle, *Phil. Trans. R. Soc. London*, **299**, 319-356, 1981.

Mitchell, B.J., Anelastic structure and evolution of the continents from seismic surface wave attenuation, *Rev. Geophys.*, **33**, 441-462, 1995.

Mitrovica, J.X. and A.M. Forte, Radial profile of mantle viscosity; results from the joint inversion of convection and postglacial rebound observables. *J. Geophys. Res.*, **102**, 2751-2769, 1997.

Montagner, J.P. and D.L. Anderson, Petrological constraints on seismic anisotropy, *Phys. Earth planet. Inter.*, **54**, 82-105, 1989.

Montagner, J.P. and T. Tanimoto, global anisotropy in the upper mantle inferred from regionalization of phase velocities, *J. Geophys. Res.*, **95,** 4797-4819, 1990.

Montagner, J.P. and T. Tanimoto, Global upper mantle tomography of seismic velocities and anisotropies, *J. Geophys. Res.*, **96,** 20,337-20,351, 1991.

Montagner, J.P., What can seismology tell us about mantle convection? *Rev. Geophys.*, **32**, 2, 135-137, 1994.

Montagner, J.P., Upper mantle low anisotropy channels below the Pacific Plate, *Earth Planet. Sci. Lett.*, **202**, 263-274, 2002.

Mooney W.D., G. Laske and G. Masters, Crust 5.1: a global crustal model at 5 deg ×5 deg, *J. Geophys. Res.*, **103,** 727-747, 1998.

Morgan, W.J., Convection plumes in the lower mantle. *Nature*, **230**, 42-43, 1971.

Nolet, G. and F.A. Dahlen, Wavefront healing and the evolution of seismic delay times, *J. Geophys. Res.*, **105**, 19,043-19,054, 2000.

Nyblade, A.A. and S.W. Robinson, The African superswell, *Geophys. Res. Lett.*, **21**, 765-768, 1994.

Park, J., Asymptotic coupled mode expressions for multiplet amplitude anomalies and frequency shifts on an aspherical Earth, *Geophys. J. R. Astr. Soc.*, **90**, 129-169, 1987.

Phinney, R.A. and R. Burridge, Representation of the elastic-gravitational excitation of a spherical earth model by generalized spherical harmonics, *Geophys. J. R. Astr. Soc.*, **34**, 451-487, 1973.

Rayleigh, Lord, *The Theory of Sound*. New York: Dover Publication, 1945.

Revenaugh, J. and T.H. Jordan, Mantle layering from ScS reverberations, 3. The upper mantle, *J. Geophys. Res.*, **96**, 19,781-19,810, 1991.

Reid, F.J.L. and J.H. Woodhouse and H.H. van Heist, Upper mantle attenuation and velocity structure from measurements of differential S phases, *Geophys. J. Int.*, **145,** 615-630, 2001.

Richards, M.A., B.H. Hager and N.H. Sleep, Dynamically supported geoid highs over hotspots: observation and theory, *J. Geophys. Res.*, **93**, 7690-7708, 1988.

Ritsema, J., S. Ni, D.V. Helmberger and H.P. Crotwell, Evidence for strong shear velocity reductions and velocity gradients in the lower mantle beneath Africa, *Geophys. Res. Lett.*, **25**, 4,245-4,248, 1998.

Ritsema, J., H. van Heijst and J.H. Woodhouse, Complex shear wave velocity structure imaged beneath Africa and Iceland, *Science*, **286**, 1925-1928, 1999.

Robin, L., *Fonctions sphériques de Legendre et fonctions sphéroidales,* Gauthiers Villars, Paris, 1958.

Romanowicz, B. and G. Roult, First order asymptotics for the eigenfrequencies of the Earth and application to the retreival of large-scale lateral variations of structure, *Geophys. J. R. Astr. Soc.*, **87**, 209-239, 1986.

Romanowicz, B., Multiplet-multiplet coupling due to lateral heterogeneity: asymptotic effects on the amplitude and frequency of Earth's normal modes, *Geophys. J. R. Astr. Soc.*, **90**, 75-100, 1987a.

Romanowicz, B., G. Roult and T. Kohl, The upper mantle degree two pattern: constraints from GEOSCOPE fundamental spheroidal mode eigenfrequency and attenuation measurements, *Geophys. Res. Lett.*, **14**, 1219-1222, 1987b.

Romanowicz, B., The upper mantle degree two: constraints and inferences on attenuation tomography from global mantle wave measurements, *J. Geophys. Res.*, **95**, 11,051-11,071, 1990.

Romanowicz, B., Anelastic tomography: a new perspective on upper mantle thermal structure *Earth Planet. Sci. Lett.*, **128**, 113-121, 1994a.

Romanowicz, B., On the measurement of Anelastic attenuation using amplitudes of low frequency surface waves, *Phys. Earth planet. Inter.*, **84,** 179-191, 1994b.

Romanowicz, B., A global tomographic model of shear attenuation in the upper mantle, *J. Geophys. Res.*, **100,** 12,375-12,394, 1995.

Romanowicz, B. and Y. Gung, Superplumes from the core-mantle boundary to the lithosphere: implications for heat flux, *Science*, **296**, 513-516, 2002.

Romanowicz, B., Y. Gung and Y. Capdeville, Long period seismograms in a 3D earth: tests of normal mode asymptotic approximations against computations using the Spectral Element Method, *in preparation*, 2003.

Roth, E., D.A. Wiens, L.M. Dorman, J. Hildebrand and S.C. Webb, Seismic attenuation tomography of the Tonga back-arc region using phase pair methods, *J. Geophys. Res.*, **104**, 4795-4809, 1999.

Roult, G., B. Romanowicz and J.P. Montagner, 3-D upper mantle shear velocity and attenuation from fundamental mode free oscillation data *Geophys. J. Int.*, **101,** 61-80, 1990.

Rudnick, R., W. McDonough and R. O'Connell, Thermal structure, thickness and composition of continental lithosphere, *Chem. Geol.*, **145**, 395-411, 1998.

Selby, N.D. and J.H. Woodhouse, Controls on Rayleigh wave amplitudes: attenuation and focusing, *Geophys. J. Int.*, **142,** 933-940, 2000.

Selby, N.D. and J.H. Woodhouse, The Q structure of the upper mantle: constraints from Rayleigh wave amplitudes, *J. Geophys. Res.*, **107**, 933-940, 2097, doi:10.1029/2001JB000257, 2002.

Shearer, P., Seismic imaging of upper mantle structure with new evidence for a 520km discontinuity, *Nature*, **344**, 121-126, 1990.

Silver, P.G., Seismic anisotropy beneath the continents: probing the depths of geology. *Ann. Rev. Earth Planet. Sci.*, **24**, 385-432, 1996.

Sleep, N.H., Hotspots and mantle plumes: some phenomenology, *J. Geophys. Res.*, **95**, 6,715-6,736, 1990.

Stark, P.B. and D.I. Nikolayev, Toward tubular tomography, *J. Geophys. Res.*, **98**, 8,095-8,106, 1993.

Su, W.J., R.L. Woodward and A.M. Dziewonski, Degree 12 model of shear velocity in the mantle, *J. Geophys. Res.*, **99**, 6,945-6,980, 1994.

Su, W.J. and A.M. Dziewonski, Predominance of long-wavelength heterogeneity in the mantle, *Nature*, **352**, 121-126, 1991.

Suda, N., N. Shibata and Y. Fukao, Degree-2 pattern of attenuation structure in the upper mantle from apparent complex frequency measurements of fundamental spheroidal modes, *Geophys. Res. Lett.*, **18**, 1119-1122, 1991.

Tanimoto, T., A simple derivation of the formula to calculate synthetic long-period seismograms in a heterogeneous earth by normal mode summation, *Geophys. J. R. Astr. Soc.*, **77**, 275-278, 1984.

Tanimoto, T., Free oscillation in a slightly anisotropic Earth, *Geophys. J. R. Astr. Soc.*, **87,** 493-517, 1986.

Tarantola, A. and B. Valette, Generalized non-linear inverse problems solved using the least-squares criterion, *Rev. Geophys.*, **20**, 219-232, 1982.

Tong, C., O. Gudmundsson and B.L.N. Kennett, Shear wave splitting in refracted waves returned from the upper mantle transition zone beneath northern Australia, *J. Geophys. Res.*, **99**, 15,783-15,797, 1994.

Vasco, D.W. and L.R. Johnson, Whole earth structure estimated from seismic arrival times, *J. Geophys. Res.*, **103**, 2,633-2,671, 1998.

Vinnik, L.P., L.I. Makeyeva, A. Milev and Y. Usenko, Global patterns of azimuthal anisotropy and deformations in the continental mantle, *Geophys. J. Int.*, **111**, 433-447, 1992.

Warren, L.M., and P.M. Shearer, Investigating the frequency dependence of mantle Q by stacking P and PP spectra, *J. Geophys. Res.*, **105**, 25,391-25,402, 2000.

Warren, L.M., and P.M. Shearer, Mapping lateral variation in upper mantle attenuation by stacking P and PP spectra, *J. Geophys. Res.*, **107**, 2342, doi:10.1029/2001JB001195, 2002.

Wolfe, C.J., I.Th. Bjarnason, J.C. VanDecar and S.C. Solomon, Seismic structure of the Iceland mantle plume. *Nature*, **385**, 245-247, 1997.

Woodhouse, J.H., The coupling and attenuation of nearly resonnant multiplets in the earth's free oscillation spectrum, *Geophys. J. R. Astr. Soc.*, **61**, 261,283, 1980.

Woodhouse, J.H., The joint inversion of seismic waveforms for lateral variations in Earth structure and earthquake source parameters, *Proc. 'Enrico Fermi' Int. Sch. Phys. LXXXV*, (eds. Kanamori, H. and Boschi, E.), 366-397, 1983.

Woodhouse, J.H. and A.M. Dziewonski, Mapping the upper mantle: Three dimensional modeling of Earth's structure by inversion of seismic waveforms, *J. Geophys. Res.*, **89**, 5,953-5,986, 1984.

Woodhouse, J.H. and Y.K. Wong, Amplitude, phase and path anomalies of mantle waves, *Geophys. J. R. Astr. Soc.*, **87**, 753-773, 1986.

Woodhouse, J.H. and T.P. Girnius, Surface waves and free oscillations in a regionalized earth model, *Geophys. J. R. Astr. Soc.*, **68**, 653-673, 1982.

Zhang, Y.S. and T. Tanimoto, High-resolution global upper mantle structure and plate tectonics, *J. Geophys. Res.*, **98,** 9793-9823, 1993.

# Appendix A

## A.1

We apply the stationary phase approximation method to derive the asymptotic integration in (2.63).

Let

$$I(\lambda) = \int_0^{2\pi} g(\lambda, \mu) \cos\left[\kappa F(\mu)\right] d\mu. \tag{A.1}$$

Following *Romanowicz & Roult* [1986] and *Romanowicz* [1987a], the stationary points are $\mu = 0$ and $\mu = \pi$, i.e. on the great circle. The contribution of the points $\mu = 0$, to order $1/l$, is

$$I_0(\lambda) = \sqrt{\frac{2\pi}{\kappa |F_0^{"}|}} \left[ \cos(\kappa F_0 + \frac{\pi}{4}) g_0 - \frac{1}{\kappa} \sin(\kappa F_0 + \frac{\pi}{4}) (h g_0 + \frac{g_2}{2F_0^{"}}) \right], \tag{A.2}$$

where

$$\begin{aligned} \kappa F_0 &= \kappa\beta_0 - \frac{\pi}{4} + \frac{N\pi}{2} + (\frac{N^2}{2\kappa} - \frac{1}{8\kappa}) \cot\beta_0, \\ g_0 &= g(\lambda, 0), \end{aligned}$$

$$
\begin{aligned}
F_0^{"} &= \frac{\partial^2 \beta}{\partial \mu}(\mu = 0) = \frac{\sin\lambda \sin\Delta}{\sin\beta_0}, \\
g_2 &= \frac{\partial^2 g}{\partial \mu}(\mu = 0), \\
h_0 &= -\frac{1}{8}\frac{F""}{(F")^2} = \frac{1}{8}\left[\frac{1}{\beta"_0} + 3\cot\beta_0\right].
\end{aligned} \tag{A.3}
$$

After some algebra, $g_2$ becomes:

$$
g_2 = \frac{1}{\sqrt{\sin\beta_0}}\left[\frac{\partial^2 \delta\omega^2_{KK'}}{\partial\mu^2} - \frac{\delta\omega^2_{KK'}}{2}\beta_0" \cot\beta_0 - \left(M - N\frac{\partial\mu'}{\partial\mu}|_0\right)^2 \delta\omega^2_{KK'} + 2i\left(M - N\frac{\partial\mu'}{\partial\mu}|_0\right)\frac{\partial\delta\omega^2_{KK'}}{\partial\mu}\right]. \tag{A.4}
$$

All quantities in (A.4) are calculated at $\mu = 0$. Using the following relations in the configuration of Figure 2.3

$$
\begin{aligned}
\mu'|_0 &= \pi, \\
\beta_0 &= \lambda - \Delta, \\
\beta"_0 &= F"_0 = \frac{\sin\lambda\sin\Delta}{\sin\beta_0}, \\
\cot\beta_0 &= \cot\lambda + \frac{1}{\beta"_0}, \\
\frac{\partial\mu'}{\partial\mu}|_0 &= \frac{\sin\lambda}{\sin\beta_0},
\end{aligned} \tag{A.5}
$$

it can be shown, by the same procedures, that the contribution $I_\pi$ from the stationary points $\mu = \pi$ is

$$
\begin{aligned}
& \int_0^\pi \sqrt{\sin\lambda}\ \cos\left[\kappa' F(\kappa', M, \lambda)\right](I_0 + I_\pi)d\lambda \\
= & \int_0^{2\pi} \sqrt{\sin\lambda}\ \cos\left[\kappa' F(\kappa', M, \lambda)\right] I_0 d\lambda.
\end{aligned} \tag{A.6}
$$

Substituting $I_0$ into (2.63), ignoring terms of order higher than $1/l$ and rapidly varying terms in $\cos(k\lambda)$, and assuming $\delta\omega_{KK'} = \delta\omega_{KK'} = \delta\omega_{KK}$ [*Romanowicz*, 1987a], we obtain $A_{KK'}$, and similarly, $A_{K'K}$:

$$\begin{aligned} A_{KK'} &= \frac{\omega_K}{\pi^2}\sqrt{\frac{2\pi}{\kappa}}\sum_{NM} i^{N+M} R_K^N S_{K'}^M \times \\ &\quad \int_0^{2\pi} d\lambda \left[\delta\omega_{KK}\cos(\Psi_1(\lambda)) + \frac{1}{2k}Q(\lambda,\delta\omega_{KK})\sin(\Psi_1(\lambda))\right], \qquad \text{(A.7)} \\ A_{K'K} &= \frac{\omega_K}{\pi^2}\sqrt{\frac{2\pi}{\kappa}}\sum_{NM} i^{N+M} R_K^N S_{K'}^M \times \\ &\quad \int_0^{2\pi} d\lambda \left[\delta\omega_{KK}\cos(\Psi_2(\lambda)) + \frac{1}{2k}Q(\lambda,\delta\omega_{KK})\sin(\Psi_2(\lambda))\right], \qquad \text{(A.8)} \end{aligned}$$

where

$$\begin{aligned} \Psi_1(\lambda) &= \kappa\Delta + j\lambda - \frac{\pi}{4} + (M+N)\frac{\pi}{2}, \qquad \text{(A.9)} \\ \Psi_2(\lambda) &= \kappa\Delta - j(\lambda-\Delta) - \frac{\pi}{4} + (M+N)\frac{\pi}{2}, \qquad \text{(A.10)} \\ Q(\lambda,\delta\omega_{KK}) &= \delta\omega_{KK}\left[(-\frac{M^2+N^2}{2} + \frac{1}{8})\cot\Delta + \frac{MN}{\sin\Delta}\right] + \\ &\quad i(ME_1 - NE_2) + D. \qquad \text{(A.11)} \end{aligned}$$

Here $j = K - K'$, and the 'off-great-circle' terms $E_1$, $E_2$, and $D$ are defined by

$$\begin{aligned} E_1 &= \frac{1}{\beta"_0}\frac{\partial\delta\omega_{KK}^2}{\partial\mu}, \\ E_2 &= \frac{1}{\beta"_0}\frac{\sin\lambda}{\sin\beta_0}\frac{\partial\delta\omega_{KK}^2}{\partial\mu}, \qquad \text{(A.12)} \\ D &= \frac{1}{2\beta"_0}\frac{\partial^2\delta\omega_{KK}}{\partial\mu^2}. \end{aligned}$$

Also note that, when one consider multiplets along the same dispersion branch,

$$\omega_K^2 - \omega_{K'}^2 = \omega_K^2 - \omega_{K+j}^2 \approx -2j\omega_K \frac{U}{a}, \tag{A.13}$$

where $a$ is the earth's radius and $U = a(\partial\omega_K/\partial K)$ is the group velocity of the multiplet $K$ in the reference Earth model.

Following the derivation of ( *Romanowicz* [1987a], equations 28-44), grouping the phase terms $\Psi_1$ and $\Psi_2$ as a function of $j$, we obtain $\sum_{K\neq K'}(A_{KK'} + A_{K'K})$ in terms of minor (with *tilde* accent) and great circle (with *hat* accent) averages of $D$, $E_1$,$E_2$ and local frequency $\delta\omega_{KK}$, whereas $\sum_{K=K'} A_{KK'}$, the self-coupling terms, are expressed in terms of great circle averages only. The contribution to the seismogram from multiplet $K$, to order $1/l$, is

$$\begin{aligned} u_K(t) &= \Re e \sum_{NM} i^{M+N} R_K^N S_K^M \sqrt{\frac{2\pi}{k}} \frac{1}{\pi\sqrt{\sin\Delta}} \exp(i\omega_K t) \times \\ &\quad \Big[\cos(f_\kappa(M,N) + \frac{\alpha_{NM}}{k}) \\ &\quad + it\left(\delta\hat{\omega}_{KK}\cos(f_\kappa(M,N)) + \frac{A_K}{k}\sin(f_\kappa(M,N))\right) \\ &\quad + \frac{a\Delta}{U}\left((\delta\tilde{\omega}_{KK} - \delta\hat{\omega}_{KK})\sin(f_\kappa(M,N)) + \frac{X_K}{k}\cos(f_\kappa(M,N))\right)\Big], \end{aligned} \tag{A.14}$$

where

$$f_\kappa(M,N) = \kappa\Delta - \frac{\pi}{4} + (M+N)\frac{\pi}{2}, \tag{A.15}$$

$$\alpha_{NM} = (\frac{M^2+N^2}{2} - \frac{1}{8})\cot\Delta - \frac{MN}{\sin\Delta}, \tag{A.16}$$

$$\begin{aligned} A_K &= A_{Kr}^{NM} + iA_{Ki}^{NM} \\ &= \frac{\hat{D}_K}{2} + \delta\hat{\omega}_{KK}\left(\frac{\cot\Delta}{8} + \frac{MN}{\sin\Delta} - \frac{\cot\Delta}{2}(M^2+N^2)\right) + \\ &\quad i\left(M\hat{E}_1 - N\hat{E}_2\right), \end{aligned} \tag{A.17}$$

$$
\begin{aligned}
X_K &= X_{Kr}^{NM} + iX_{Ki}^{NM} \\
&= \frac{\hat{D}_K - \tilde{D}_K}{2} + (\delta\hat{\omega}_{KK} - \delta\tilde{\omega}_{KK})\left(\frac{\cot\Delta}{8} + \frac{MN}{\sin\Delta} - \frac{\cot\Delta}{2}(M^2+N^2)\right) + \\
&\quad i\left(M(\hat{E}_1 - \tilde{E}_1) - N(\hat{E}_2 - \tilde{E}_2)\right). \qquad \text{(A.18)}
\end{aligned}
$$

$A_{Kr}^{NM}$, $A_{Ki}^{NM}$, $X_{Kr}^{NM}$ and $X_{Ki}^{NM}$ are given in Appendix B.

We can then separate terms that depend on $\Delta$ and $t$ from terms that depend only on the source characteristics, and, with the help as given in Appendix B, we obtain expressions (2.66)- (2.70).

# A.2

Denoting the complex amplitude of multiplet $K$ by $A_K$, we may rewrite (A.14), to the zeroth order in $1/l$ along a single mode branch

$$
\begin{aligned}
u_K(t) &= \Re e\ A_K \exp(i\omega_K t) \\
&\approx \Re e\ A_K^0(1+\delta\Delta)\exp(i(\omega_K + \delta\hat{\omega}_K)t), \qquad \text{(A.19)}
\end{aligned}
$$

where $\delta\Delta = \frac{a\Delta}{\kappa U}(\hat{\omega}_K - \tilde{\omega}_K)$ is the 'epicentral distance shift' introduced by *Woodhouse & Dziewonski* [1984] to account for the odd part of lateral heterogeneity. As mentioned in Section 2.3, the *PAVA* (2.32) is then equivalent to zeroth order approximation when one considers only the contribution from along-branch coupling.

# Appendix B

The expressions used in equations (2.67)-(2.70) are defined as follows:

$$
\begin{aligned}
T_0 &= \sum_{NM} R_K^N S_K^M i^{M+N} \cos((M+N)\frac{\pi}{2}), \\
T_1 &= \sum_{NM} R_K^N S_K^M i^{M+N} \sin((M+N)\frac{\pi}{2}), \\
F_1 &= \sum_{NM} R_K^N S_K^M i^{M+N} X_{Kr}^{NM} \cos((M+N)\frac{\pi}{2}), \\
F_2 &= \sum_{NM} R_K^N S_K^M i^{M+N} X_{Kr}^{NM} \sin((M+N)\frac{\pi}{2}), \\
F_3 &= \sum_{NM} R_K^N S_K^M i^{M+N} A_{Kr}^{NM} \cos((M+N)\frac{\pi}{2}), \\
F_4 &= \sum_{NM} R_K^N S_K^M i^{M+N} A_{Kr}^{NM} \sin((M+N)\frac{\pi}{2}), \\
F_5 &= \sum_{NM} R_K^N S_K^M i^{M+N} \alpha_{Kr}^{NM} \cos((M+N)\frac{\pi}{2}), \\
F_6 &= \sum_{NM} R_K^N S_K^M i^{M+N} \alpha_{Kr}^{NM} \sin((M+N)\frac{\pi}{2}), \\
i\tilde{F}_7 &= \sum_{NM} R_K^N S_K^M i^{M+N} X_{Ki}^{NM} \cos((M+N)\frac{\pi}{2}), \\
i\tilde{F}_8 &= \sum_{NM} R_K^N S_K^M i^{M+N} X_{Ki}^{NM} \sin((M+N)\frac{\pi}{2}), \\
i\tilde{F}_9 &= \sum_{NM} R_K^N S_K^M i^{M+N} A_{Ki}^{NM} \cos((M+N)\frac{\pi}{2}),
\end{aligned}
\tag{B.1}
$$

$$i\tilde{F}_{10} = \sum_{NM} R_K^N S_K^M i^{M+N} A_{Ki}^{NM} \sin((M+N)\frac{\pi}{2}),$$

where

$$\begin{aligned}
A_{Kr}^{NM} &= \frac{\hat{D}_k}{2} - \delta\hat{\omega}_K \alpha_{NM}(\Delta), \\
A_{Ki}^{NM} &= M\hat{E}_1 - N\hat{E}_2, \\
X_{Kr}^{NM} &= \frac{\hat{D}_k - \tilde{D}_k}{2} - \alpha_{NM}(\Delta)(\delta\hat{\omega}_K - \delta\tilde{\omega}_K), \\
X_{Ki}^{NM} &= M(\hat{E}_1 - \tilde{E}_1) - N(\hat{E}_2 - \tilde{E}_2), \\
\alpha_K^{NM} &= (\frac{M^2+N^2}{2} - \frac{1}{8})\cot\Delta - \frac{MN}{\sin\Delta},
\end{aligned} \tag{B.2}$$

and, following *Romanowicz* [1987a]:

$$\begin{aligned}
D_k(\theta,\phi) &= \frac{\sin(\phi-\Delta)}{\sin\Delta}\left(\frac{\partial^2\delta\omega_K}{\partial\theta^2}\sin\phi - \frac{\partial\delta\omega_K}{\partial\phi}cos\phi\right), \\
E_{1k}(\theta,\phi) &= \frac{\sin(\Delta-\phi)}{\sin\Delta}\frac{\partial\delta\omega_K}{\partial\theta}, \\
E_{2k}(\theta,\phi) &= -\frac{\sin\phi}{\sin\Delta}\frac{\partial\delta\omega_K}{\partial\theta}.
\end{aligned} \tag{B.3}$$

The symbols *tilde* and *hat* represent the minor arc and great circle averages respectively, see (2.72) for example.

The receiver terms $R_K^N$ and the source terms $S_K^M$ are defined by *Woodhouse & Girnius* [1982] (table 1):

$$\begin{aligned}
R_K^0 &= k_0 U v_r, \\
R_K^{\pm 1} &= k_1(V \pm iW)(\mp v_\theta - iv_\phi),
\end{aligned}$$

$$
\begin{aligned}
S_K^0 &= -k_0[\partial r U M_{rr} + 1/2 f(M_{\theta\theta} + M_{\phi\phi})], \\
S_K^{\pm 1} &= k_1(X \mp iZ)(\pm M_{r\theta} - iM_{r\phi}), \\
S_K^{\pm 2} &= -k_2 r_s^{-1}(V \mp iW)[(M_{\theta\theta} - M_{\phi\phi}) \mp 2iM_{\theta\phi}],
\end{aligned}
\tag{B.4}
$$

with

$$
\begin{aligned}
k_n &= \frac{1}{2^n}\left[\frac{2l+1}{4\pi}\cdot\frac{(l+n)!}{(l-n)!}\right]^{1/2}, \\
f &= \frac{2U - l(l+1)V}{r}, \\
X &= \partial_r V + \frac{U-V}{r}, \\
Z &= \partial_r W - \frac{W}{r}.
\end{aligned}
\tag{B.5}
$$

Here $v_r, v_\theta, v_\phi$ are the components of the instrument vector, $M_{rr}$, $M_{r\theta}$ etc., are the components of moment tensor, and $U$, $V$ and $W$ are the scalar eigenfunctions of the $K$th mode. The eigenfunctions are evaluated at Earth's surface ($r = a$) for receiver terms and at the source radius ($r = r_s$) for source terms.

We also define:

$$
\begin{aligned}
T_2 &= \sum_{NM} R_K^N S_K^M i^{M+N} iM \cos((M+N)\frac{\pi}{2}), \\
T_3 &= \sum_{NM} R_K^N S_K^M i^{M+N} iM \sin((M+N)\frac{\pi}{2}), \\
T_4 &= \sum_{NM} R_K^N S_K^M i^{M+N} iN \cos((M+N)\frac{\pi}{2}), \\
T_5 &= \sum_{NM} R_K^N S_K^M i^{M+N} iN \sin((M+N)\frac{\pi}{2}), \\
T_6 &= \sum_{NM} R_K^N S_K^M i^{M+N} (M^2+N^2) \cos((M+N)\frac{\pi}{2}), \\
T_7 &= \sum_{NM} R_K^N S_K^M i^{M+N} (M^2+N^2) \sin((M+N)\frac{\pi}{2}), \\
T_8 &= \sum_{NM} R_K^N S_K^M i^{M+N} MN \cos((M+N)\frac{\pi}{2}),
\end{aligned}
\tag{B.6}
$$

$$T_9 = \sum_{NM} R_K^N S_K^M i^{M+N} MN \sin((M+N)\frac{\pi}{2}),$$

and

$$\begin{aligned}
a_{01} &= \frac{\hat{D}_k - \tilde{D}_k}{2} + \frac{\cot\Delta}{8}(\delta\hat{\omega}_K - \delta\tilde{\omega}_K),\\
a_{11} &= \frac{\delta\hat{\omega}_K - \delta\tilde{\omega}_K}{\sin\Delta},\\
a_{21} &= (\delta\hat{\omega}_K - \delta\tilde{\omega}_K)\cot\Delta,\\
a_{02} &= \frac{\hat{D}_k}{2} + \frac{\cot\Delta}{8}\delta\hat{\omega}_K,\\
a_{12} &= \frac{\delta\hat{\omega}_K}{\sin\Delta},\\
a_{22} &= \delta\hat{\omega}_K\cot\Delta,\\
a_{03} &= -\frac{\cot\Delta}{8},\\
a_{13} &= -\frac{1}{\sin\Delta},\\
a_{23} &= -\cot\Delta,\\
a_{31} &= \hat{E}_1 - \tilde{E}_1,\\
a_{32} &= \hat{E}_1,\\
a_{41} &= \hat{E}_2 - \tilde{E}_2,\\
a_{42} &= \hat{E}_2.
\end{aligned} \tag{B.7}$$

With (B.6) and (B.7) , we may rewrite $F$ terms in (B.1) by

$$\begin{aligned}
F_1 &= a_{01}T_0 + a_{11}T_8 - \frac{a_{21}}{2}T_6,\\
F_2 &= a_{01}T_1 + a_{11}T_9 - \frac{a_{21}}{2}T_7,\\
F_3 &= a_{02}T_0 + a_{12}T_8 - \frac{a_{22}}{2}T_6,\\
F_4 &= a_{02}T_1 + a_{12}T_9 - \frac{a_{22}}{2}T_7,
\end{aligned} \tag{B.8}$$

$$
\begin{aligned}
F_5 &= a_{03}T_0 + a_{13}T_8 - \frac{a_{23}}{2}T_6, \\
F_6 &= a_{03}T_1 + a_{13}T_9 - \frac{a_{23}}{2}T_7, \\
F_7 &= -\tilde{F}_7 = a_{31}T_2 - a_{41}T_4, \\
F_8 &= -\tilde{F}_8 = a_{31}T_3 - a_{41}T_5, \\
F_9 &= -\tilde{F}_9 = a_{32}T_2 - a_{42}T_4, \\
F_{10} &= \tilde{F}_{10} = a_{32}T_3 - a_{42}T_5.
\end{aligned}
$$

With the help of (B.4 ), we define

$$
\begin{aligned}
\tilde{R}_0 &= R_0 = k_0 U v_r, \\
\tilde{R}_1 &= i(R_{-1} + R_1) = 2k_1(V v_\phi + W v_\theta), \\
\tilde{S}_0 &= -k_0 \left[\partial_r U M_{rr} + \frac{1}{2} f(M_{\theta\theta} + M_{\phi\phi})\right], \\
\tilde{S}_1 &= -i(S_1 + S_{-1}) = -2k_1(Z M_{r\theta} + X M_{r\phi}), \\
\tilde{S}_2 &= S_2 + S_{-2} = -2\frac{k_2}{r_s}\left[V(M_{\theta\theta} - M_{\phi\phi}) - 2W M_{\theta\phi}\right], \\
\tilde{R}_{-1} &= R_1 - R_{-1} = 2k_1(W v_\phi - V v_\theta), \\
\tilde{S}_{-1} &= S_1 - S_{-1} = -2k_1(Z M_{r\phi} - X M_{r\theta}), \\
\tilde{S}_{-2} &= i(S_2 - S_{-2}) = -2\frac{k_2}{r_s}\left[2V M_{\theta\phi} + W(M_{\theta\theta} - M_{\phi\phi})\right],
\end{aligned}
\tag{B.9}
$$

where $R_0 = R_K^0$, $R_1 = R_K^1$ etc. $T$ terms in (B.8 ) can then be expressed as

$$
\begin{aligned}
T_0 = &\ \tilde{R}_1\tilde{S}_1 + \tilde{R}_0(\tilde{S}_0 + \tilde{S}_2), \\
T_1 = &\ \tilde{R}_1(\tilde{S}_0 + \tilde{S}_2) - \tilde{R}_0\tilde{S}_1, \\
T_2 = &\ \tilde{R}_1\tilde{S}_{-1} + 2\tilde{R}_0\tilde{S}_{-2}, \\
T_3 = &\ 2\tilde{S}_{-2}\tilde{R}_1 - \tilde{R}_0\tilde{S}_{-1}, \\
T_4 = &\ \tilde{R}_{-1}S_1,
\end{aligned}
\tag{B.10}
$$

$$
\begin{aligned}
T_5 = & \quad -\left[\tilde{R}_{-1}(\tilde{S}_0 + \tilde{S}_2)\right], \\
T_6 = & \quad 2\left[\tilde{R}_1\tilde{S}_1 + 2\tilde{S}_2\tilde{R}_0\right], \\
T_7 = & \quad \tilde{R}_1\tilde{S}_0 + 5\tilde{R}_1\tilde{S}_2 - R_0\tilde{S}_1, \\
T_8 = & \quad \tilde{R}_{-1}S_{-1}, \\
T_9 = & \quad 2\tilde{R}_{-1}\tilde{S}_{-2}.
\end{aligned}
$$